Design, Synthesis, and Evaluation of Tacrine-Based Derivatives: Potential Agents to Treat Alzheimer's Disease

by

Wesseem Osman

A thesis

presented to the University of Waterloo

in fulfillment of the

thesis requirement for the degree of

Master of Science

in

Pharmacy

Waterloo, Ontario, Canada, 2013

AUTHOR'S DECLARATION

I hereby declare that I am the sole author of this thesis. This is a true copy of the thesis, including any required final revisions, as accepted by my examiners.

I understand that my thesis may be made electronically available to the public.

ABSTRACT

With the incidence of Alzheimer's disease (AD) growing worldwide and in Canada along with the growing economic and social burdens, the need for more effective therapies becomes of great importance. Since the discovery of AD, a number of proposed theories have arisen to explain the pathophysiology including the i) cholinergic theory, ii) oxidative stress pathways, and iii) metal ion imbalance. The major class of drug therapies to treat AD are cholinesterase inhibitors; however, the "one drug, one target" approach has not proven fruitful and generally becomes ineffective in later stages of disease progression. In this project, we synthesized a library of 1,2,3,4-tetrahydroacridine derivatives (**10a-d**, **11a-e**, **12a-e**, and **13a-f**) as potential agents to target the cholinergic and oxidative stress pathways of AD. Chapter I provides background information on the role of AChE and BuChE enzymes in AD. Furthermore, this chapter describes the neurotoxicity of reactive oxygen species (ROS) and metals in AD. Chapter II provides a summary of project hypothesis and rationale. Chapter III describes the synthetic details regarding the synthesis of target small molecules. It further describes the principles involved in carrying out biological evaluation such as AChE and BuChE inhibition, antioxidant properties via DPPH stable radical scavenging, iron chelation capacity using ferrozine and in vitro cell viability data in neuroblastoma cells. Chapter IV describes the SAR details on ChE inhibition, antioxidant activities, iron chelation and cell viability profiles and molecular modeling details. A brief conclusion and future directions are included in Chapter V and the final section, Chapter VI provides experimental details for synthetic chemistry including analytical data of synthesized compounds and protocols for biological evaluations. This study identified novel tetrahydroacridine derivatives with nanomolar inhibition of both human AChE and human BuChE enzymes that were more potent relative to the reference agent tacrine. Compound **10d**

[*N*-(3,4-dimethoxybenzyl)-1,2,3,4-tetrahydroacridin-9-amine] was identified as a potent inhibitor of BuChE (IC_{50} = 24.0 nM) and compound **13c** [6-chloro-*N*-(pyridine-2-ylmethyl)-1,2,3,4-tetrahydroacridin-9-amine] was identified as a potent inhibitor of AChE (IC_{50} = 95.0 nM) with good inhibition of BuChE (IC_{50} = 1.61 μM) whereas compound **11e** [6-chloro-*N*-(3,4-dimethoxybenzyl)-1,2,3,4-tetrahydroacridin-9-amine] was identified with an optimum combination of dual AChE and BuChE inhibition (AChE IC_{50} = 0.9 μM; BuChE IC_{50}= 1.4 μM). In conclusion, our studies provide new insight into the design and development of novel tetrahydroacridine derivatives to target multiple pathological routes of AD.

ACKNOWLEDGEMENTS

I would like to extend my thanks to the University of Waterloo's School of Pharmacy for supporting the presented work. In addition, I would like to thank Rx and D Canada, the Ontario Graduate Scholarship (OGS), the Queen Elisabeth II graduate Scholarship in Science and Technology (honourary), and the Graduate Studies Office for their funding of the project and conference expenses.

I would also like to acknowledge Tarek Mohamed for his expertise during the project as a mentor. Thanks to Maryam Vasefi and Dr. Michael Beazely for providing MTT cell viability assay data. Finally, I would like to acknowledge Victor Munsing Sit, and Katherine Tran for their dedication, hard work and valuable assistance with the project during their time as volunteers with our research group.

DEDICATION

I would like to dedicate the efforts presented here to my parents, Mustapha and Fida Osman, my brother, Medo, my tortoise, Mango, and close friends and colleagues who supported me throughout my graduate career. I would also like to dedicate my work to Dr. Praveen Nekkar for not only giving me this great opportunity, but for his support and mentorship throughout my masters project. Finally, I would also like to extend my appreciation to my committee members, Dr. Michael Beazely and Dr. David Rose for their advice and support over the last 6 terms.

TABLE OF CONTENTS

LIST OF FIGURES

LIST OF TABLES

LIST OF SCHEMES

LIST OF ABBREVIATIONS

AAPH – 2,2'-Azobis-(2-methylpropionamidine) dihydrochloride

Aβ – Amyloid beta

ACh – Acetylcholine

AChE –Acetylcholinesterase

AD - Alzheimer's disease

Ala - Alanine

APP – Amyloid precursor protein

Asp – Aspartate

BuChE – Butyrylcholinesterase

$CDCl_3$ – Deuterated chloroform

ChAT – Cholineacetyltransferase

ChE – Cholinesterase

CNS – Central nervous system

DCM – Dichloromethane

DIPEA – Diisopropylethylamine

DTNB – Dithiobis-(2-nitrobenzoic acid)

EtOAc – Ethylacetate

EtOH – Ethanol

Glu – Glutamate

*h*AChE – Human acetylcholinesterase

*h*BuChE – Human butyrylcholinesterase

His – Histidine

HPLC – High performance liquid chromatography

IC_{50} – Inhibition concentration 50

Leu – Leucine

MeOH – Methanol

$MgSO_4$ – Magnesium sulfate

mL – Millilitre

mM – Millimolar

mmol – Millimole

mp – Melting point

MS – Mass spectroscometry

MTT – 3-(4,5-Dimethylthiazol-2-yl)-2,5-diphenyltetrazolium bromide

MV – Molecular volume

MW – Molecular weight

NaI – Sodium iodide

NaOH – Sodium hydroxide

NH_4OH – Ammonium hydroxide

NMR – Nuclear magnetic resonance

nM – Nanomolar

nm – Nanometer

PAS – Peripheral anionic site

Pd/C – Palladium/carbon

Phe – Phenylalanine

$POCl_3$ – Phosphorus oxychloride

pv – Pressure vial

RBF – Round bottom flask

r.t. – Room temperature

SAR – Structure activity relationship

Ser – Serine

$SnCl_2$ – Tin (II) chloride

THA – 9-Chloro-1,2,3,4-tetrahydroacridine

Trp – Tryptophan

Tyr – Tyrosine

μM – Micromolar

Val – Valine

CHAPTER I

Introduction

1.1 The History of Alzheimer's Disease

In 1907, Alois Alzheimer diagnosed a patient for the first time with a type of dementia which would later be identified as Alzheimer's disease (AD).[1] Symptoms including memory loss and cognitive dysfunction were typified as hallmarks of AD and were found to affect the aging population.[1,2] Anatomical hallmarks include the presence of senile plaques and neurofibrillary tangles. The reason for the decrease in memory and cognitive ability for those living with AD is due to the neurodegenerative nature of the disease. The resulting affect of AD is a decrease in brain mass, affecting cholinergic neuron-dense areas of the central nervous system (CNS) such as the nucleus basalis of Meynert and the hippocampus, areas of the brain which have roles in memory and cognition.[3,4] Ultimately, after disease progression, patients will develop issues with speech, recollection of past events, and difficulties with concentration.[1,5]

Since its discovery, AD has had an increasing socio-economic burden and as of 2011 approximately 36 million individuals worldwide are living with AD.[6] By 2030, this number is expected to increase to almost 66 million. In the United States alone, caregivers, such as family members and friends, contribute nearly 17 billion hours of unpaid work valued at almost $200 billion, and costs of $200 billion for healthcare providers, long-term care and hospices already strain the American healthcare system in addition to the 500 000 Canadians with AD.[7] It has been a major challenge to determine the initial cause of AD as it is a multifaceted disorder. A number of hypotheses have been posited to resolve the etiology of AD with research being done to determine the major driving forces for the disease.

1.2 The Cholinergic Hypothesis

Alzheimer's disease primarily results in the neurodegeneration of cholinergic neurons in the CNS resulting in decreased neuronal cell signalling, an important process in basic human physiology. During AD, there is a decrease in the levels of choline acetyltransferase (ChAT), the enzyme responsible for catalysis of acetylcholine (ACh, Fig. 1) formation, resulting in a decrease in ACh levels in the CNS.[8] As one of the crucial neurotransmitters, ACh is used by cholinergic neurons to communicate with other neurons via propagation of a neural impulse. ACh is released as a chemical neurotransmitter by a pre-synaptic neuron into a region called the synaptic cleft. The ACh will traverse this region and bind to cholinergic receptors on the post-synaptic neuron, thus propagating the neuronal signal. Cholinesterases will further deplete the level of ACh thus exacerbating the condition and further promoting AD pathology.

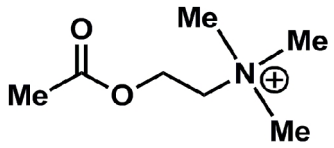

Acetylcholine

Figure 1: Chemical structure of the neurotransmitter acetylcholine (ACh)

1.2.1 The Cholinesterases

Acetylcholinesterase (AChE) (EC 3.1.1.7) and butyrylcholinesterase (BuChE) (EC 3.1.1.8) are both responsible for enzymatically hydrolyzing ACh into its inactive metabolites, acetate and choline (Fig. 2).[9]

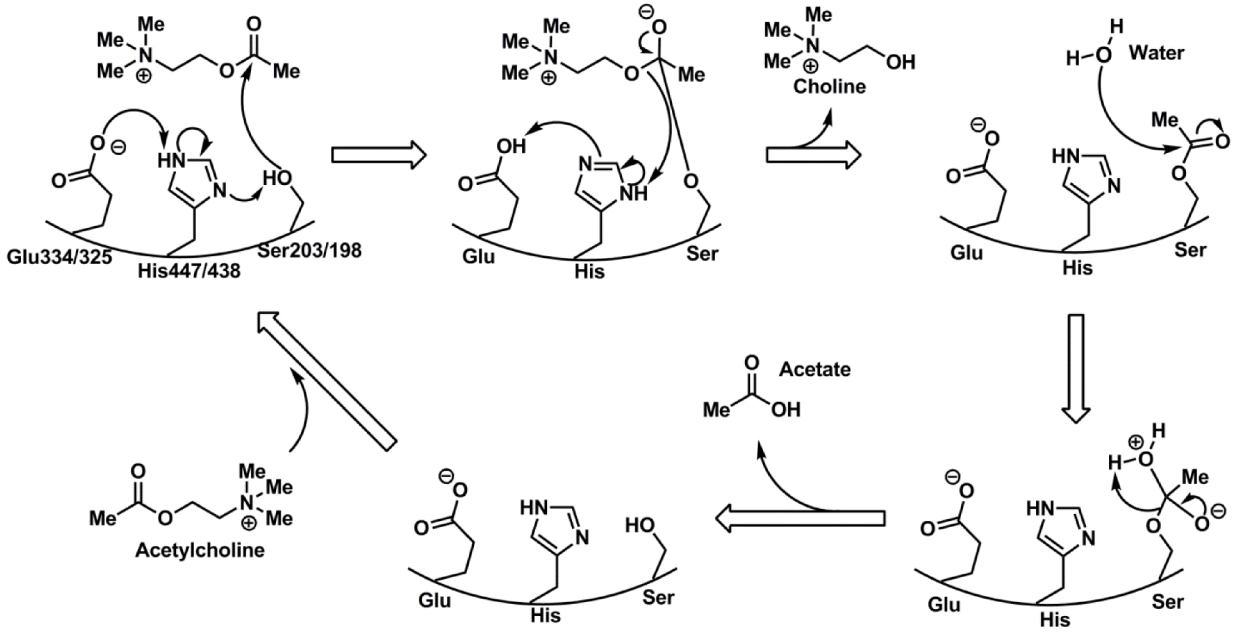

Figure 2: Enzymatic mechanism of acetylcholine hydrolysis by AChE (Glu334, His447, Ser 203) and BuChE (Glu325, His 438, Ser198)

Under normal physiological conditions AChE is the major enzyme that is known to recycle or remove excess ACh in the CNS. In early stages of AD, AChE is the primary ACh degrading enzyme; however, during disease progression there is a shift in the ratio between AChE and BuChE where BuChE becomes the primary ACh hydrolyzing enzyme.[10] Figure 2 gives the schematics of ACh hydrolysis by ChEs. Different regions of AChE exist in which its primary substrate, ACh, can interact. The AChE active site gorge is located 20 Å away from the entrance and is comprised of a catalytic triad consisting of residues serine (Ser) 203, glutamate (Glu) 334 and histidine (His) 447.[11,12] AChE depends on key hydrophobic residues to stabilize ACh once it has entered the active site allowing for its hydrolysis. These residues include phenylalanine (Phe) 338, and the cationic-π site residue, tryptophan (Trp) 86.[11,13] There also exists an acyl pocket comprised of Phe295 and Phe297, which stabilize the acetyl moiety of ACh. One particular region is the peripheral anionic site (PAS), with key residues including Trp 286, tyrosine (Tyr) 341, and aspartate (Asp) 72, which aid in directing ACh to the active site

entrance.[11,12] The PAS has been implicated in promoting the generation of beta amyloid (Aβ) plaques resulting in further neuronal damage.[14-16] It has also been found that PAS-specific binding by certain drug compounds can inhibit the formation of these plaques.[17] Like AChE, BuChE also has an active site with a catalytic triad comprised of Ser198, Glu325 and His438 as well as Trp82 and Phe329 as hydrophobic stabilizers of ACh.[11,18] However, BuChE does not have a PAS, and its acyl pocket is lined by aliphatic residues leucine (Leu) 286 and valine (Val) 288, which are smaller than the Phe residues in AChEs acyl pocket.[18] The smaller residues, along BuChEs active site contribute to its approximately 200 $Å^3$ greater active site compared to AChE, allowing BuChE to bind to a greater pool of substrates larger than ACh.[18,19] While the role of AChE has been well-documented, the exact function of BuChE in humans has yet to be discerned.

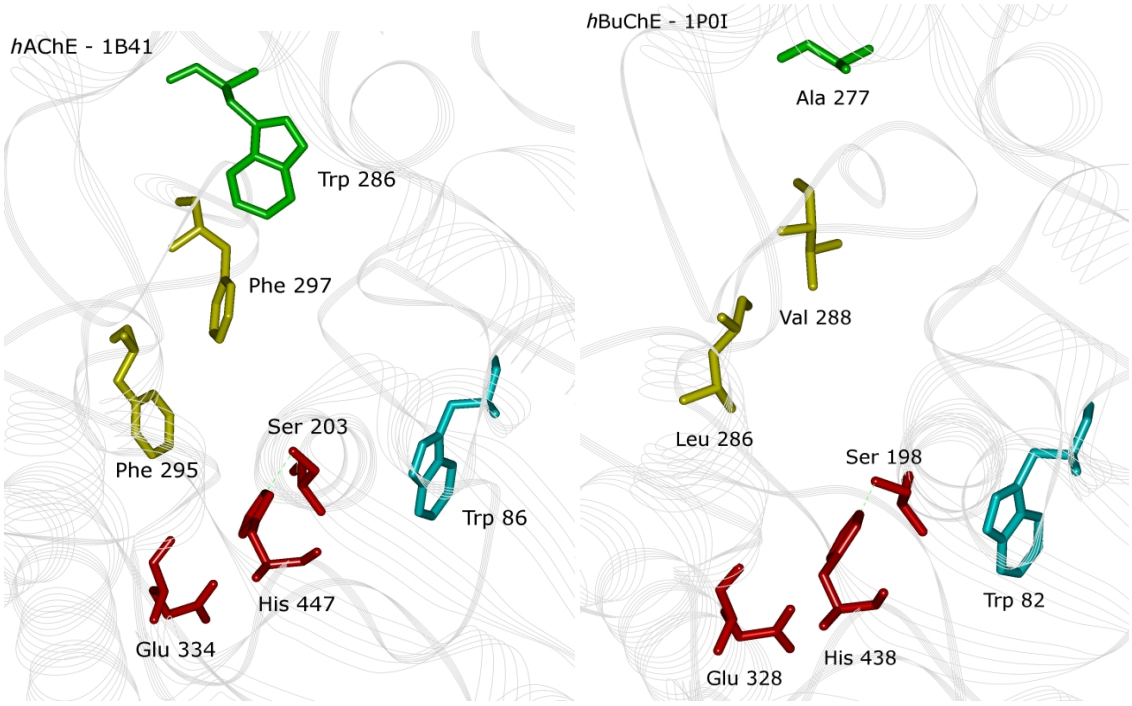

Figure 3: Active sites of *h*AChE (PDB:1B41) and *h*BuChE (PDB:1P0I), *red*: catalytic site, *blue*: cationic-π site, *yellow*: acyl pocket, *green*: gorge entry/PAS

Cholinesterase inhibitors (ChEI) represent the major class of drug treatments used in AD therapy. Some known ChEIs include donepezil (Aricept®), rivastigmine (Exelon®), galantamine (Reminyl®), and tacrine (Cognex®) (Fig. 4). Each treatment varies in the selectivity for AChE versus BuChE, and its effectiveness at various stages in AD progression, with some being more effective in early AD and others in intermediate stages.

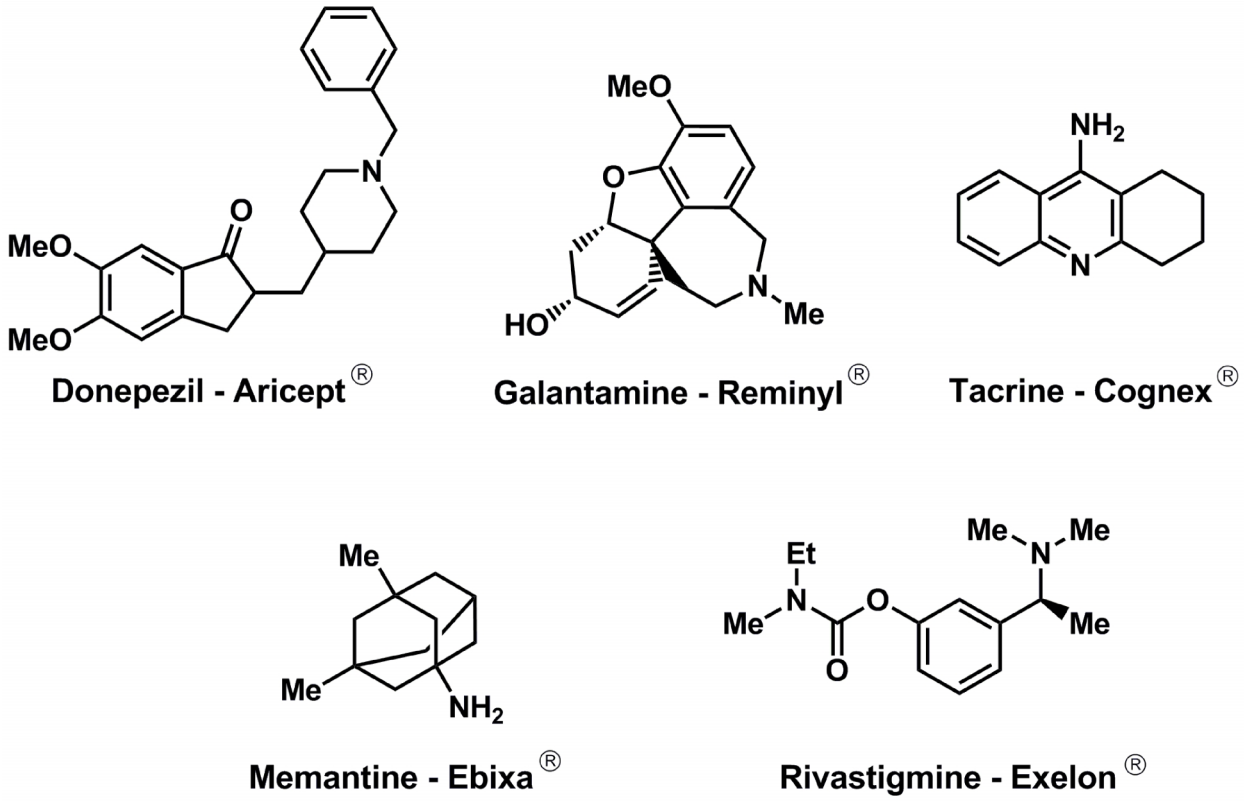

Figure 4: Chemical structures of past and current therapies used in AD treatment

1.2.2 Summary

The cholinergic hypothesis aims to make the connection between the decrease in cognitive and memory functions in AD patients with the reductions in ACh levels. The decreased levels of ChAT resulting in slower production of ACh coupled with the hydrolyzing activity of AChE and BuChE account for the decrease in ACh in cholinergic-dense regions of the CNS,

which are responsible for reduction in cognition and memory. Development of ChEIs have shown improvement with respect to the aforementioned symptoms; however, the exact cause and driving factors in AD are yet to be determined, and suggests that the cholinergic hypothesis is merely one facet in explaining this complex disease.

1.3 The Effect of Metals in AD

The multifaceted nature of AD is a major challenge in determining primary factors that result in the initiation of AD. It has been shown that certain metal ions have had a significant role in the progression of the disease by promoting neuronal cell damage via oxidative stress pathways.[20,21] Increased levels of iron (III) (Fe^{3+}), copper (II) (Cu^{2+}) and zinc (II) (Zn^{2+}) have been shown to promote the generation of reactive oxygen species (ROS) either through direct or indirect redox activity. [22] There is a marked increase in oxidative damage found in the CNS of AD patients due to the generation and increasing levels of ROS.[23-25] The connection between metal ion concentration and ROS generation makes these specific metals key pathogenic factors in AD progression as oxidative stress has a significant role in neuronal damage and cell death.[22,26,27] As with normal age progression, there is a natural increase in the concentrations of these metals; however, patients with AD have been found to have significantly higher concentrations in the CNS compared to age-matched controls.[28-34] Firstly, Fe^{3+} can promote increased translation of amyloid precursor protein (APP) by preventing iron response proteins from inhibiting an iron response element. The increase in APP results in an increase in Aβ peptides being formed, including $A\beta_{1-40}$ and $A\beta_{1-42}$. These peptides can go on to form oligomers that aggregate into fibrils, fibers, filaments, and consequently will form into senile plaques, one of the hallmarks of AD. Due to Aβ's high affinity for the aforementioned metal ions, they will continue to interact with senile plaques to generate ROS. It has been demonstrated that increased

Zn^{2+} as well as Cu^{2+} and Fe^{3+} promote increased Aβ aggregation characteristic of AD.[35-38] It is also suggested there are binding sites located on Aβ selective for both Cu^{2+} and Zn^{2+} that promote Aβ-aggregation.[28,39] Chelation of these ions inhibit the formation of senile plaques by solubilising the Aβ peptides.[40] All three metals are generally found in higher concentrations within Aβ deposits. Through redox reactions, peroxide is generated from the interaction of redox-active Fe^{3+} or Cu^{2+} and $A\beta_{1\text{-}40/1\text{-}42}$, in which peroxide undergoes further redox reactions via Fenton chemistry and Haber-Weiss reactions to generate free radicals (Fig. **5**).

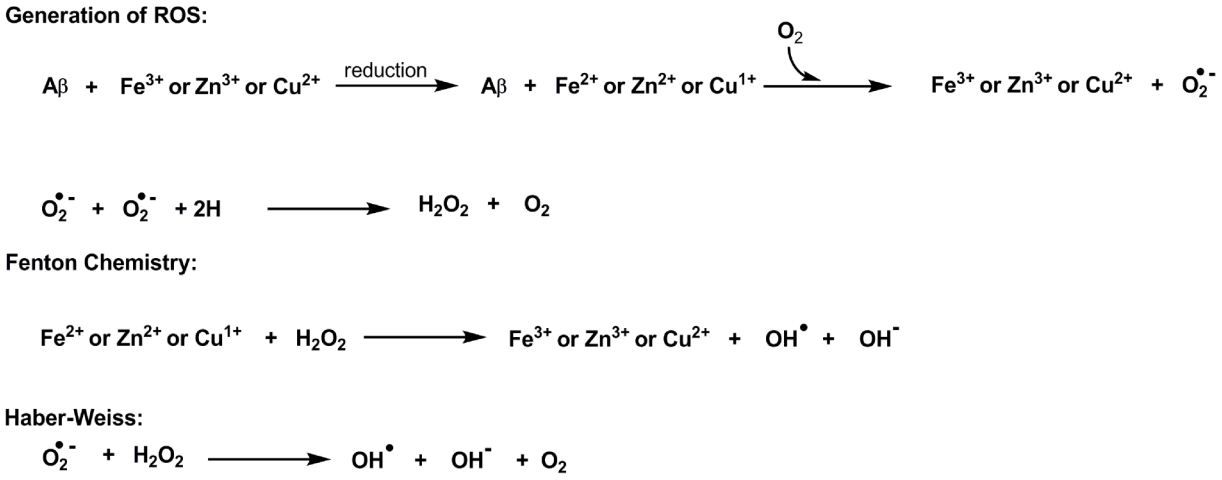

Figure 5: Reaction scheme of ROS generation through metal reduction via Fenton chemistry and Haber-Weiss reactions

1.4 The Effect of ROS in AD

As mentioned, the increase in metal ion concentration results in increased ROS generation, which go on to induce the inflammatory response and cellular damage in the CNS.[41-43] Major ROS include that of peroxide (H_2O_2), superoxide ($O_2^{\bullet -}$), and hydroxy radical ($OH^{\bullet}$). Specifically, these ROS target lipids, protein structures, and induce DNA damage, all integral in cell function and structure.[44] Unfortunately in AD, the ROS clearance mechanisms in key

regions of the CNS are reduced, including a reduction in levels of superoxide dismutase (SOD) and glutathione peroxidises.[45] The interaction between Aβ and Cu^{2+} resulting in the reduction of Cu^{2+} into Cu^{1+} and generation of neurotoxic peroxide, is markedly reduced in the presence of a copper chelator.[39] Several effective antioxidants function by stabilizing existing free radicals generally through different resonance structures, thus making them far less reactive than other ROS (Fig. 6). This exchanges the highly reactive and inflammatory hydroxy free radical ($OH^{\bullet}$) with a less reactive molecule that can be cleared from the body without producing significant cellular damage or inflammation. ROS generated *in vitro* due to Aβ have been shown to be removed by enzymatic and chemical ROS scavengers.[46-47] Effective antioxidants, which have demonstrated neuroprotective effects in *in vivo* AD animal models include resveratrol and curcumin (Fig. **7**).[45,48-51] However, these antioxidants demonstrate instability in aqueous environments and/or poor bioavailability and may suggest why they have not been effective in treating patients with AD.[52-56] Potent metal chelators include compounds possessing nitrogen-substituted functional groups that can chelate with metal ions forming a stable 5- or 6-membered ring systems (Fig. **7**).

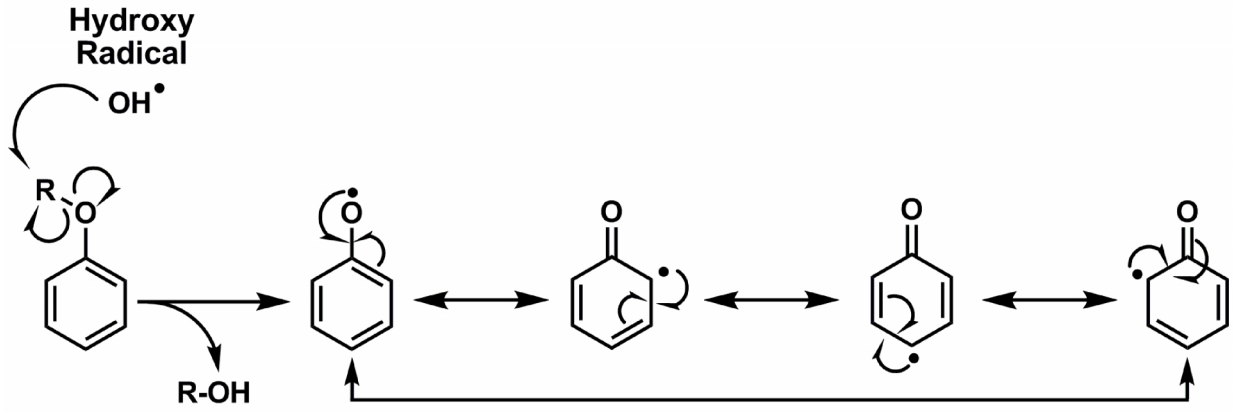

Figure 6: Mechanism of free-radical scavenging by antioxidants through resonance stabilization

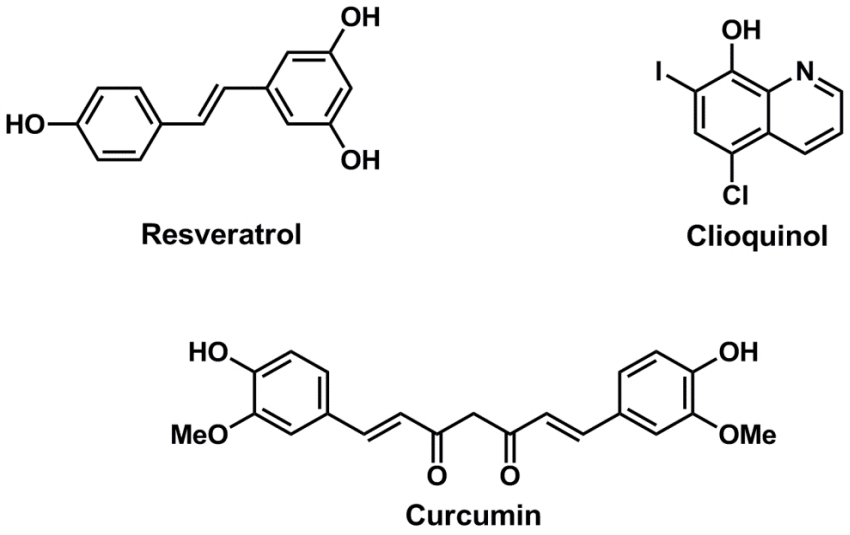

Figure 7: Structures of common antioxidants, resveratrol and curcumin, and metal chelator, clioquinol

1.4.1 Summary

The direct interaction between Cu^{2+} or Zn^{2+}, and $A\beta_{1\text{-}40/1\text{-}42}$ peptides promotes its aggregation into larger senile plaques. Additionally, Fe^{3+} promotes further expression of the APP which ultimately results in increased Aβ peptide formation. The following interactions between the senile plaques and redox-active Cu^{2+} and Fe^{3+} results in the generation of ROS, through Haber-Weiss reactions and Fenton chemistry, that go on to induce oxidative damage in the CNS. The introduction of metal chelators can inhibit the formation of these plaques and ROS. Furthermore, introduction of anti-oxidants are effective means of scavenging free radicals and other ROS, to reduce oxidative damage associated with AD.

1.5 Tacrine and Alzheimer's disease treatments

Tacrine is a potent (AChE IC_{50} = 190-230 nM, BuChE IC_{50}= 40-45 nM) selective dual-ChEI and was the first agent approved by the Food and Drug Administration (FDA) to treat AD, as Cognex (Pfizer and Warner-Lambert, New York, NY).[57] Tacrine's planar orientation allows it to bind closer to Trp86 in the active site of AChE preventing the stabilisation and hydrolysis of ACh. Currently, tacrine is no longer used to treat AD as it is associated with hepatotoxicity; however it remains as a reference compound and scaffold to develop potent ChEIs. Several research groups have synthesized novel tacrine derivatives and hybrids with potent ChEI (Fig. 8).[58-60]

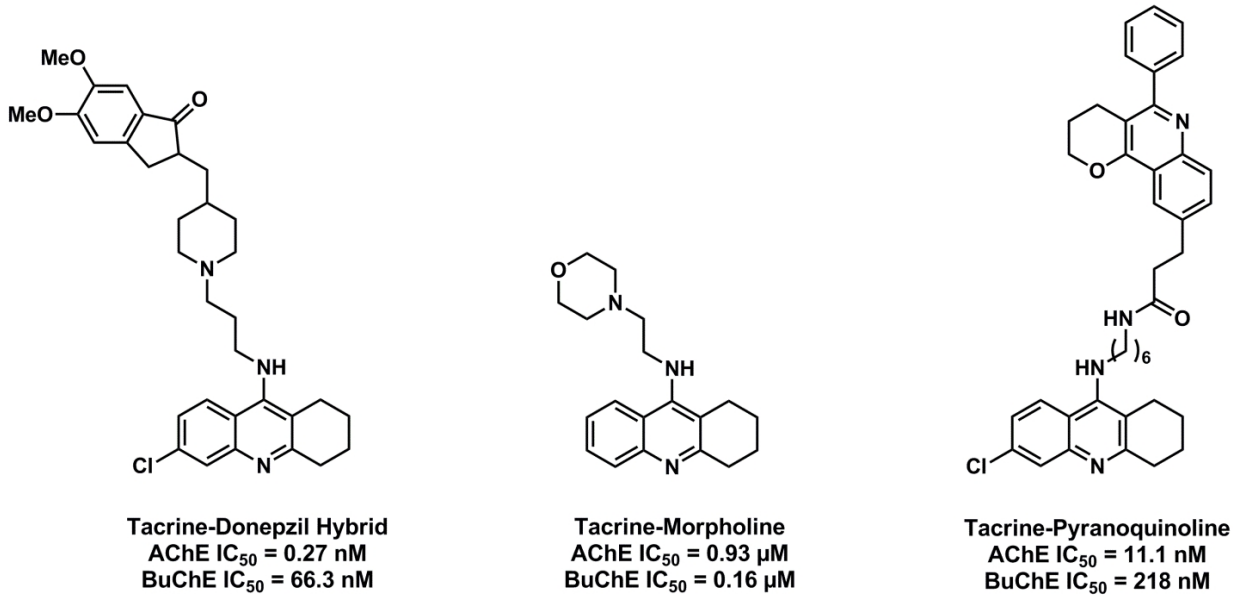

Figure 8: Chemical structure and ChE IC_{50} values of various tacrine derivatives

1.6 Chapter I Conclusion

In this chapter we examined the significant socioeconomic impact that Alzheimer's disease inflicts on national healthcare systems, on patients, and patient caregivers. With billions of dollars being spent in North America, there is a mandate for a better understanding of the disease and how to control it. Several hypotheses have arisen since the discovery of AD to better understand its pathophysiology including: i) the cholinergic hypothesis, ii) abnormalities in metal concentrations in the CNS, and iii) the oxidative stress pathway as shown in Figure 9 (Fig. 9). The first of these hypotheses, the cholinergic hypothesis, describes the significance of decreased ACh levels in the CNS leading to the hallmark symptoms of AD, including cognitive impairment and memory loss. The decrease of ACh levels is also made worse by the activity of ChE enzymes that further deplete ACh via hydrolysis. Next was the deregulation of metal ion concentrations in the brain whereby increased levels of iron, copper, and zinc ions contribute to the increased expression of Aβ peptides and interaction with senile plaques to generate ROS. Finally, these ROS promote oxidative stress where neuronal cell membranes and structures are damaged or destroyed promoting further AD progression. A major class of drug therapies known as cholinesterase inhibitors have been developed in order to treat AD with tacrine being the first FDA-approved ChEI and has become a major scaffold for developing novel drug therapies to treat AD.

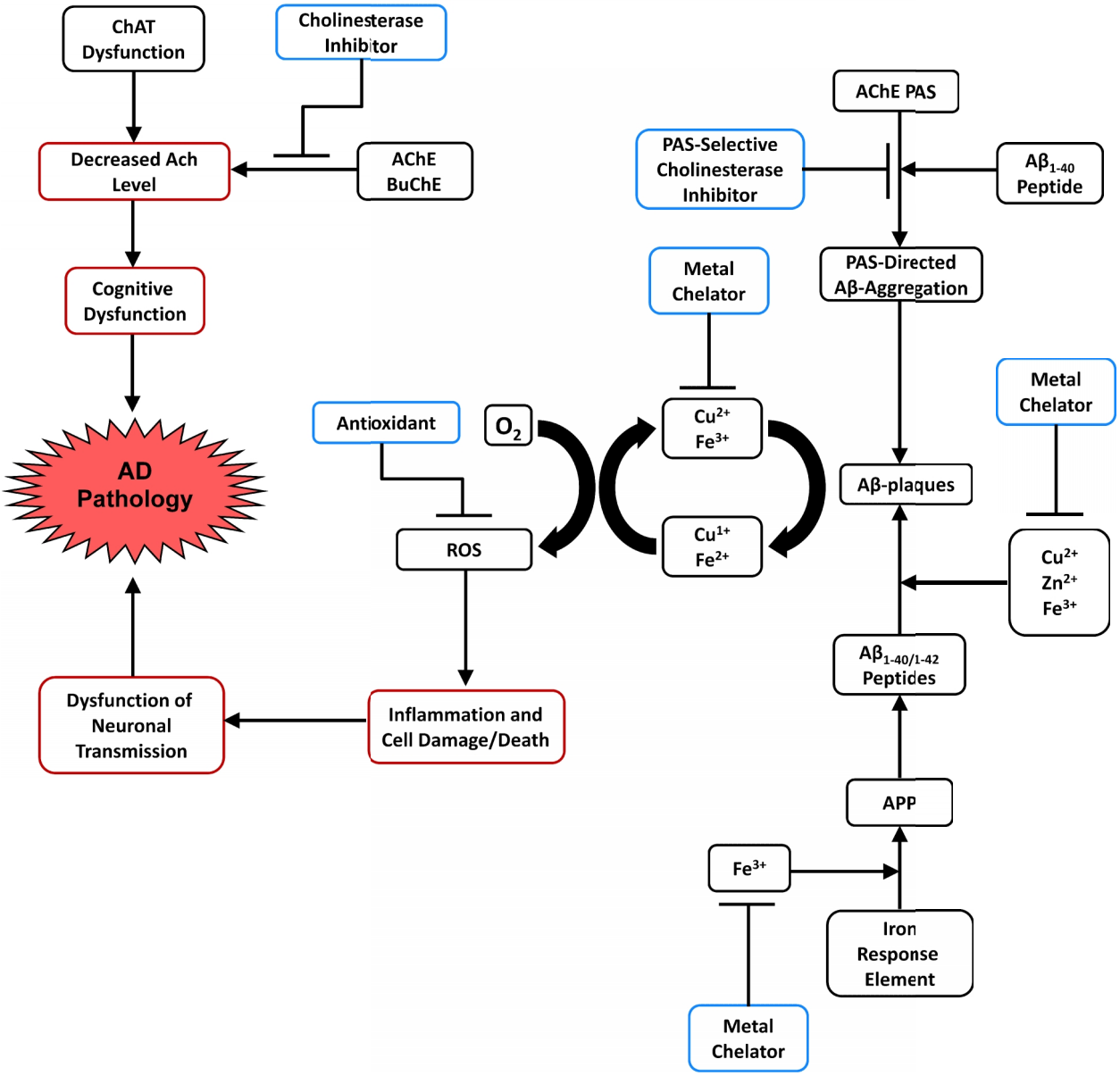

Figure 9: Outline of Alzheimer's disease pathology, major hallmarks and symptoms (red), and treatments (blue)

CHAPTER II

Hypothesis and Design Rationale

2.1 Template Design

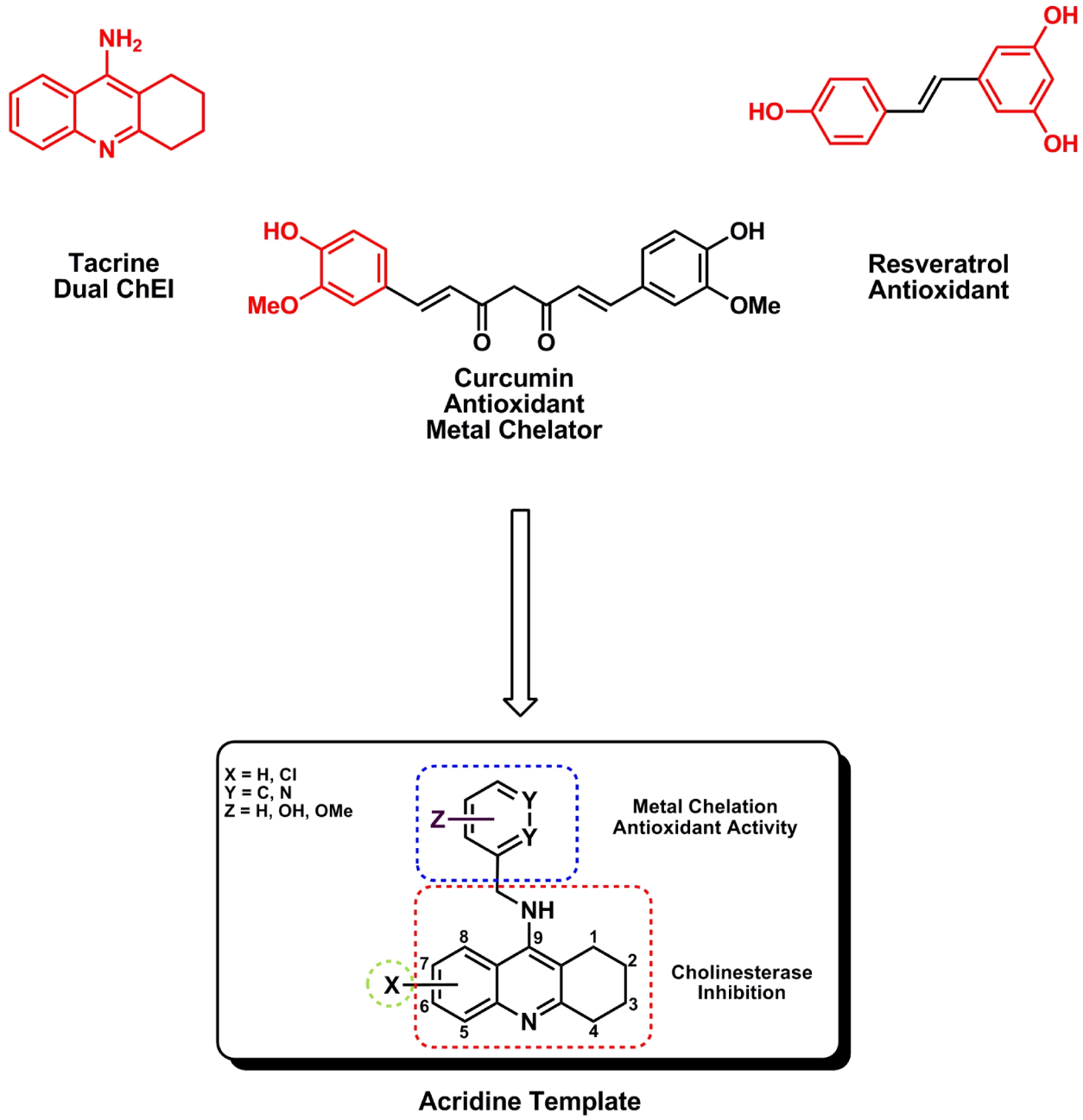

Figure 10: THA template design as dual-ChEI with antioxidant and chelating properties

The goal of this project was to develop a library of tricyclic derivatives based on a 1,2,3,4-tetrahydroacridine (THA) ring scaffold as dual-ChEI. Furthermore, substituents at C-9 position were varied to incorporate antioxidant and metal-chelating pharmacophores to target the oxidative stress pathway in AD (Fig. 10)

2.2 Target Derivatives

The fundamental goal of the project was to generate a library of THA derivatives and vary their electronic and steric parameters at C-6, C-7, and C-9 positions in order to evaluate their ability to: i) inhibit AChE and BuChE enzymes, and ii) exhibit antioxidant and metal chelating properties. The general synthetic route to obtain the library of target compounds is shown in Figure 11.

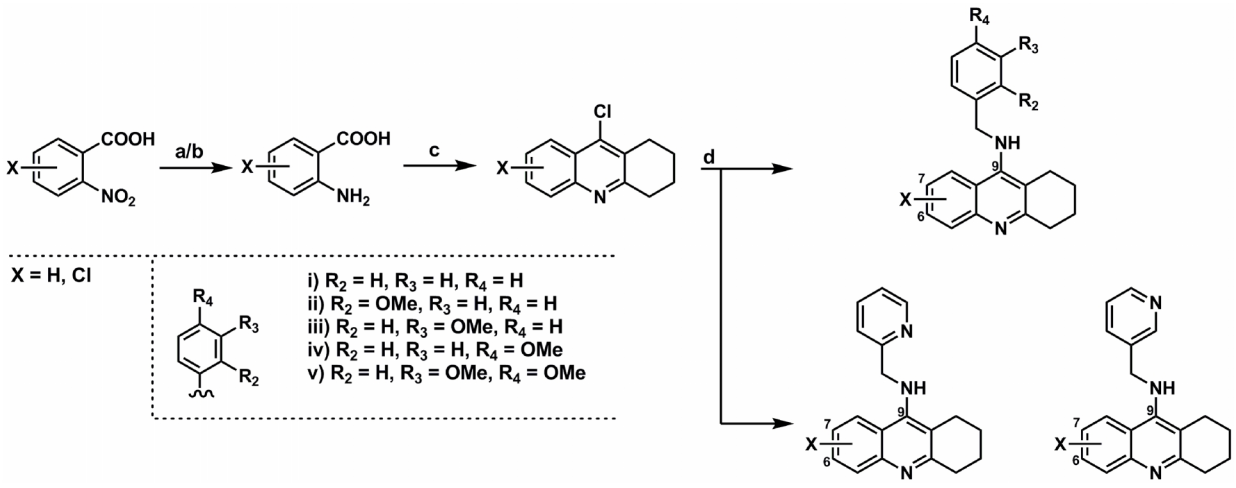

Figure 11: General overview of synthetic routes and functional groups of target compounds

CHAPTER III

Chemistry and Biological Evaluation

3.1 Computational Chemistry

Initially, the binding interaction of the THA derivative tacrine was investigated using the molecular modeling software Discovery Studio from Accelrys Inc. The known crystallographic coordinates of tacrine bound to both AChE and BuChE were studied to determine key polar and nonpolar interactions. Furthermore, THA derivatives containing various substituents and pharmacophores at C-6, C-7 and C-9 were assembled using the *build fragment* protocol in Discovery Studio. Energy minimized structures were docked in the active sites of both AChE and BuChE enzymes and their interaction energies were analyzed and ranked using a scoring function (Libdock Score) present in the docking module *LibDock*. Furthermore, critical parameters such as hydrogen bonding interactions, van der Waals interaction and electrostatic interactions were thoroughly investigated and compared with tacrine. Substituents were optimized further based on initial SAR screen for ChE inhibition to obtain better ChE inhibition.

3.2 Synthetic Chemistry

Synthetic schemes were optimized involving three to four steps to obtain target molecules. Post-synthesis purification was done by traditional work-ups and flash chromatography.

The THA derivatives with various C-6, C-7 and C-9 substituents were synthesised as per Scheme 1. Initially, nitro-substituted benzoic acid (**1, 2,** or **3**) was reduced to an amine derivative (**4, 5,** or **6**) in the presence of tin (II) chloride ($SnCl_2$) or by palladium (Pd/C) and

hydrazine under reflux (*Reaction a* and *b*, Scheme 1 and 2, Fig. 11).[61-62] The intermediate (**7, 8,** or **9**) was synthesized by coupling (**4, 5,** or **6**) with cyclohexanone in presence of phosphorous oxychloride ($POCl_3$) under reflux (Reaction **c**, Scheme 1 - 3).[63] Consequently, a nucleophilic substitution reaction with various benzylamine and picolylamine derivatives provided C-9 substituted tacrine derivatives (Reaction **d**, Scheme **1**, **2** and **3**).[64]

3.2.1 Synthetic Scheme to Prepare THA Derivatives (10 – 13)

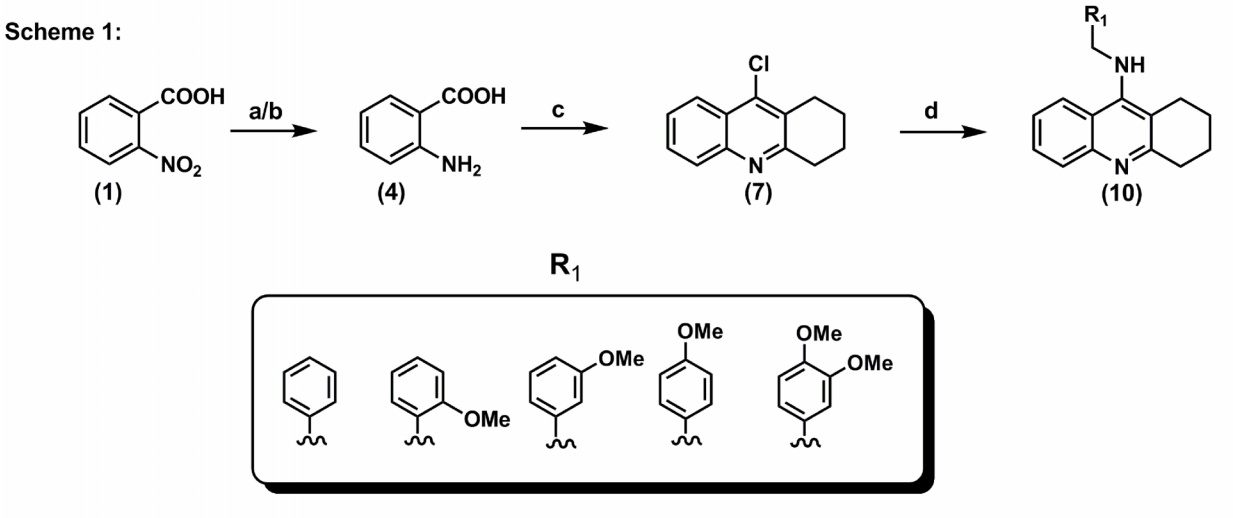

Reagents and Conditions. a: tin(II)chloride, EtOH, reflux at 75ºC 1h; **b**: Pd/C, hydrazine, EtOH, reflux at 80ºC 1.5 h; **c**: cyclohexanone, $POCl_3$, reflux at 120ºC 2.5 h; **d**: i) benzylamines, butanol, NaI, reflux 150ºC 4.5 h ii) benzylamines, phenol, NaI, reflux 180ºC 3 h

Scheme 2:

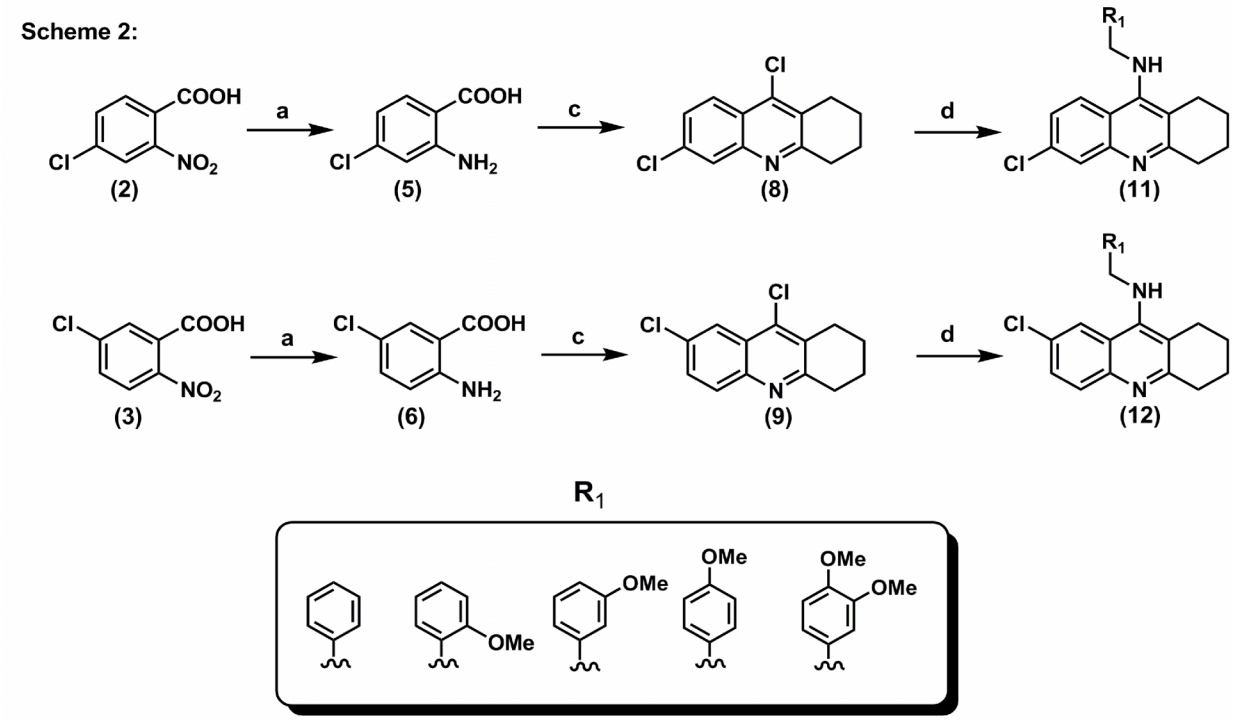

Reagents and Conditions. **a**: tin(II)chloride, EtOH, reflux at 75ºC 1h; **c**: cyclohexanone, $POCl_3$, reflux at 120ºC 2.5 h; **d**: i) benzylamines, butanol, NaI, reflux 150ºC 4.5 h ii) benzylamines, phenol, NaI, reflux 180ºC 3 h

Scheme 3:

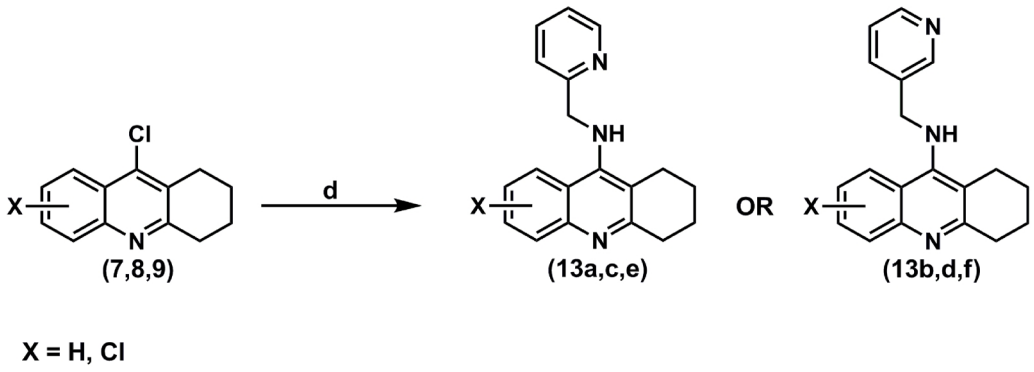

Reagents and Cinditions. d: picolylamines, butanol, NaI, reflux 150ºC 4.5 h

3.2.1. Intermediate Product Synthesis – Reaction a

The intermediate compounds 2-aminobenzoic acid and its chloro derivatives (**1**, **2**, **3**) were prepared via reduction of the C-2 nitro group into a primary amine (Fig. 12)

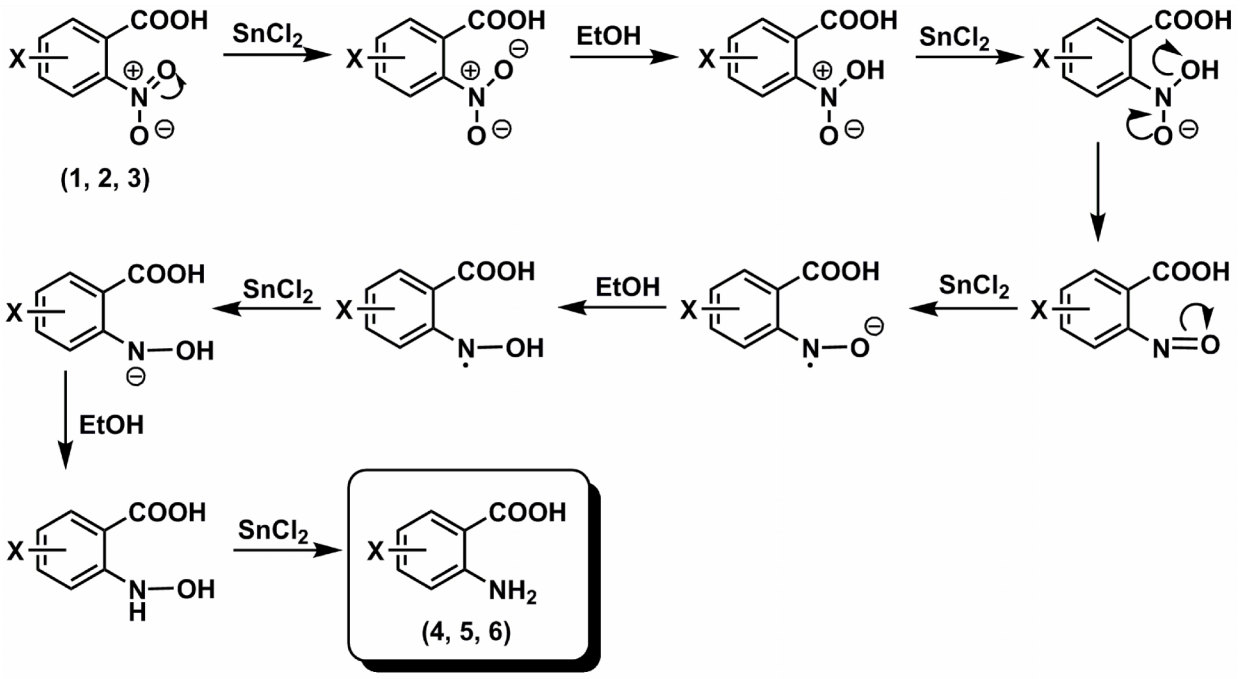

Figure 12: Reaction mechanism showing reduction of 2-nitrobenzoic acid into 2-aminobenzoic acid in presence of tin(II)chloride

The chloro- and non-chloro-nitrobenzoic acid starting material (**1**, **2**, or **3**, Scheme 1 and 2) was reduced in the presence of tin(II)chloride to convert the nitro group into an amine. Although *Reaction b* produces superior yield of the unchlorinated aminobenzoic acid intermediate, the use of a Pd/C-hydrazine reaction results in the displacement of the chlorine group from chloro-nitrobenzoic acid.

The chloro and nonchloro 2-nitrobenzoic acid starting materials (**1**, **2**, **3**, Fig. 12) were reacted in the presence of tin(II)chloride, which would dissociate to give low valent tin species

that would go on to reduce the nitro group (NO_2), to amine (NH_2) in presence of ethanol as a solvent thus producing chloro and non-chloro-aminobenzoic acid products (**4**, **5**, or **6**)

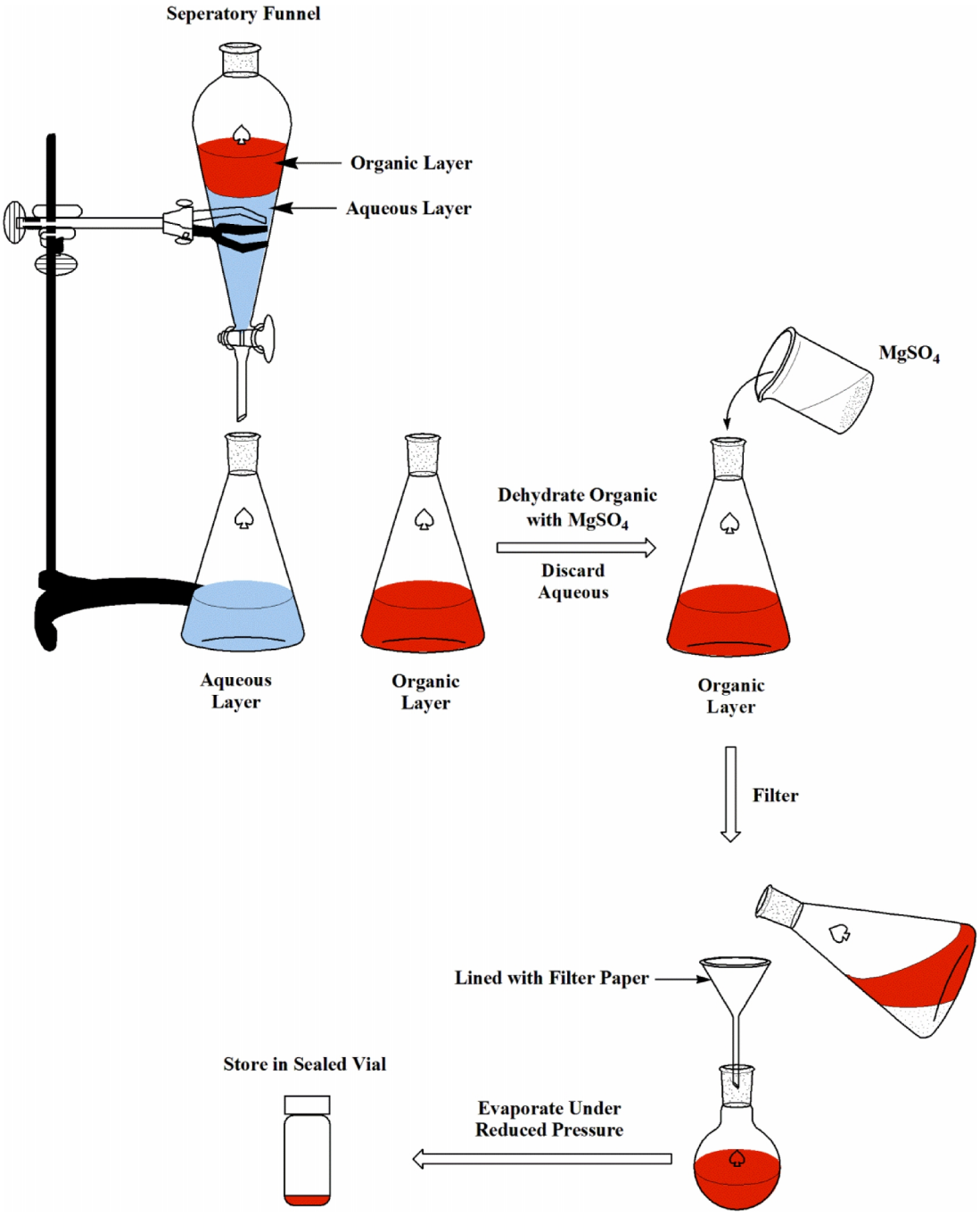

Figure 13: Overview of a brine-wash reaction workup

3.2.1.2 Intermediate Product Synthesis– Reaction b

The intermediate compound 2-aminobenzoic acid (**4**) was generated via reduction of the nitro group located at C-2 into a primary amine (Fig. 14)

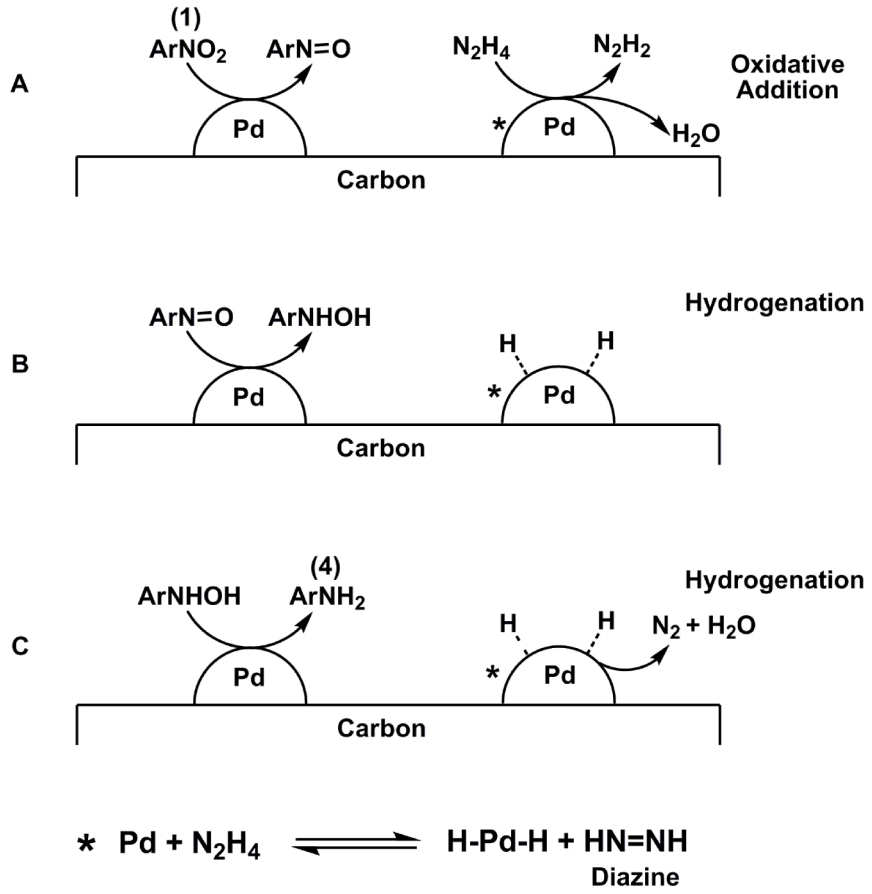

Figure 14: Reaction mechanism showing reduction of 2-nitrobenzoic acid into 2-aminobenzoic acid in presence of Pd/C and hydrazine

The 2-nitrobenzoic acid starting material (**1**, Fig. 14) was reduced in the presence of a carbon-activated palladium catalyst and hydrazine hydrate to convert the nitro group into a primary amine thus affording the 2-aminobenzoic acid product (**4**, Fig. 14) The carbon-activated palladium catalyzes the generation of hydride ions followed by a series of proton transfer reactions, which go on to reduce the nitro group into an amine, which also generates water and nitrogen gas side products.

Reaction b (Fig. 14) was run in ethanol (EtOH) and refluxed for a period of 1.5 hours with constant stirring under inert environment conditions (argon atmosphere) (Fig. 15). The completed reaction mixture was filtered via cotton plug to remove Pd/C (Fig. 16) and the EtOH solvent was evaporated under reduced pressure. Product yields ranged from 60 - 80%.

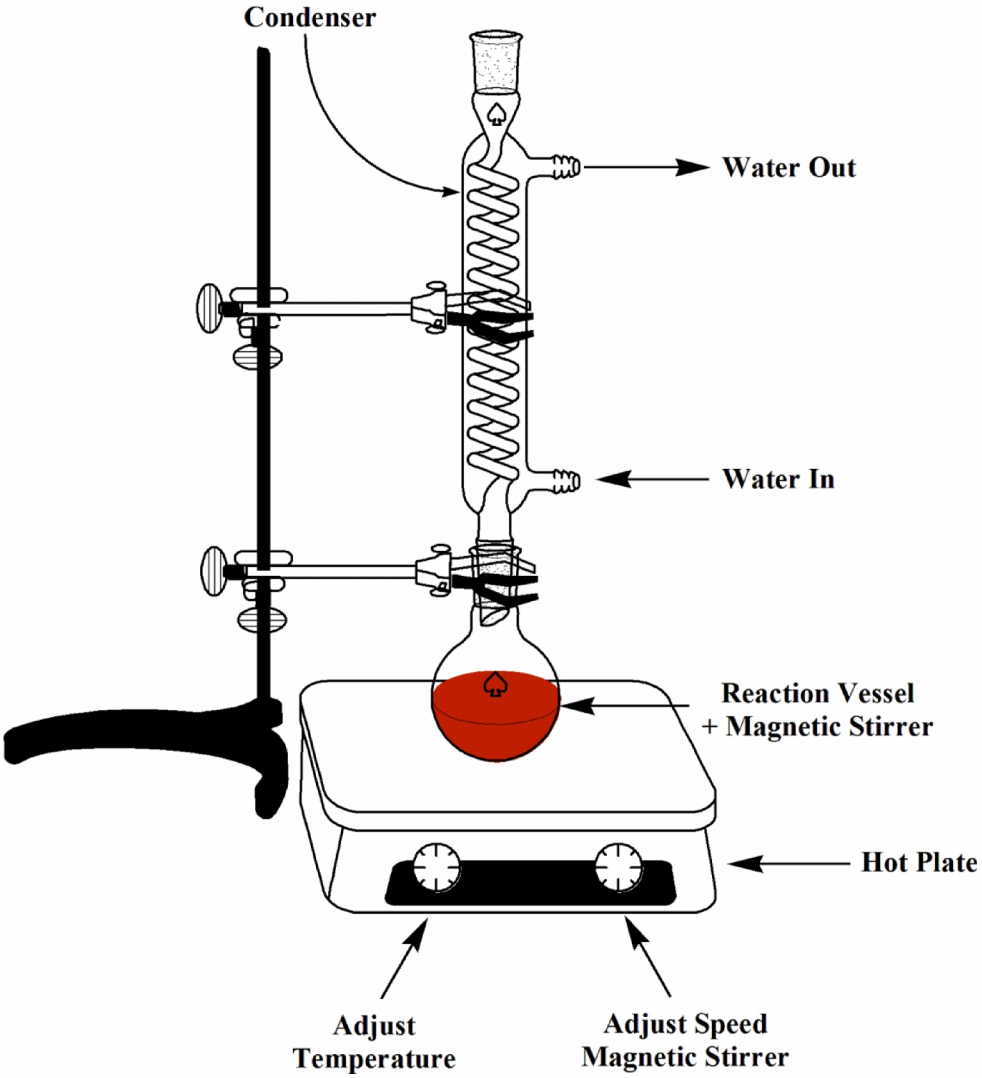

Figure 15: General setup for a refluxed reaction. Reaction vessel is heated via hot plate and evaporating solvent is condensed back into the reaction vessel via glass condenser cooled with running water

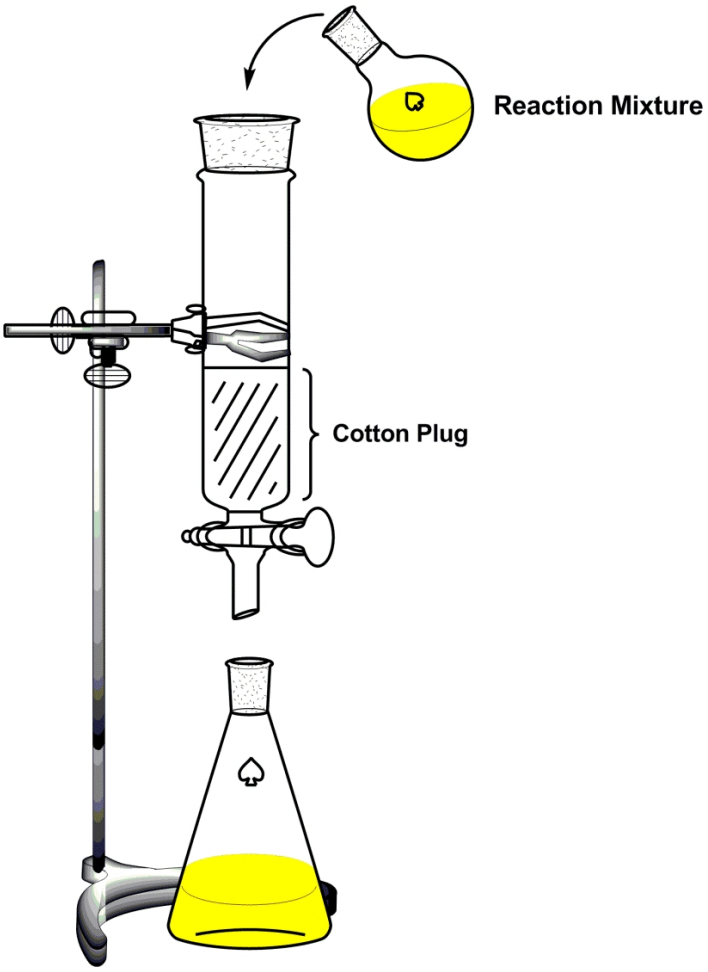

Figure 16: Overview of cotton plug filtration

3.2.1.3 Intermediate Product Synthesis – Reaction c

Intermediate compounds 9-chloro-1,2,3,4-tetrahydroacridine (9Cl-THA) and its C-6 and C-7 chloro-derivatives (**7**, **8**, **9**) were synthesized via multistep reaction mechanism where nucleophilic substitution, and elimination reactions occur (Fig. 17).

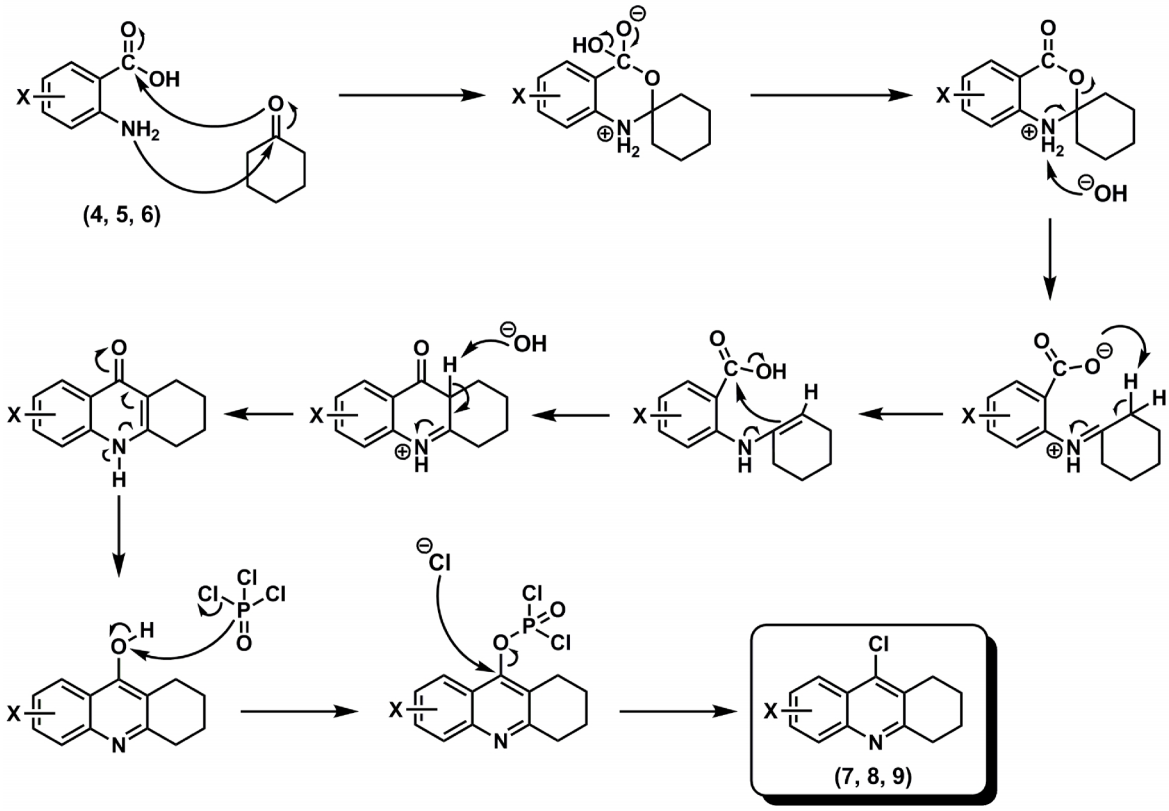

Figure 17: Reaction mechanism outlining the generation of 9-chloro-1,2,3,4-tetrahydroacridine derivatives in the presence of $POCl_3$

The mechanism of *Reaction c* begins by the nucleophilic attack of the carbonyl carbon of cyclohexanone by the primary amine of 2-aminobenzoic acid (**4**, **5**, or **6**, Fig. 17). The carbonyl oxygen of cyclohexanone also acts as a nucleophile attacking the carboxylate thus creating a 6-membered ring and eventually the desired tricyclic molecule. The reaction occurs in the presence of $POCl_3$ which generates chlorine to displace oxygen in order to afford the final 9-chloro-1,2,3,4-tetrahydroacridine product and its C-6 and C-7 chloro derivatives (**7**, **8**, or **9**, Fig. 17)

Reaction c was carried out in the presence of cyclohexanone and $POCl_3$ and kept under reflux for 2.5 hours (Fig. 15). The reaction mixture was poured on ice after cooling and mixed with excess ice water. Any formed precipitate was filtered off and the aqueous fraction was neutralized with sodium bicarbonate where further precipitate formed. The precipitate was again

filtered, combined, and dissolved in dichloromethane (DCM). The DCM fraction was washed with brine, then dried with magnesium sulphate ($MgSO_4$) and evaporated under reduced pressure (Fig. 13). The product was run through flash chromatography for further purification using DCM (Fig. 18). Product yields ranged from 50 – 80 %.

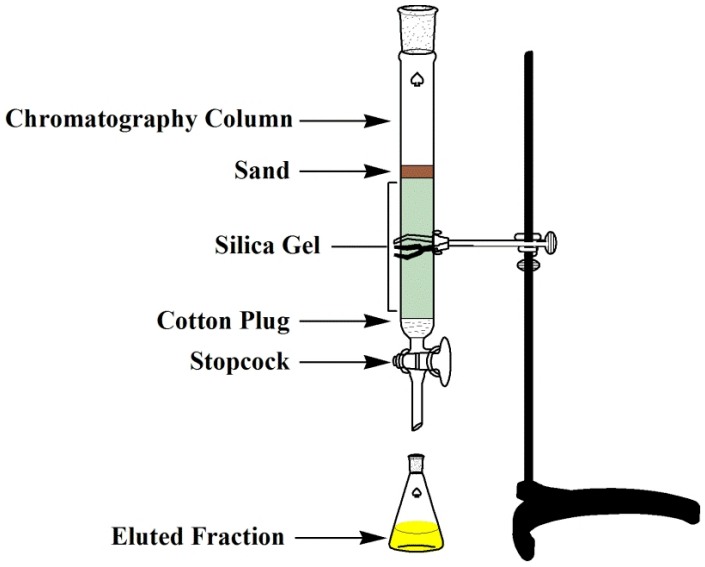

Figure 18: Overview of flash chromatography set up

3.2.1.4 Final Product Synthesis – Reaction d

Final test compounds were synthesized via a nucleophilic aromatic substitution at the C-9 position using an amine nucleophile as shown in Figure 19.

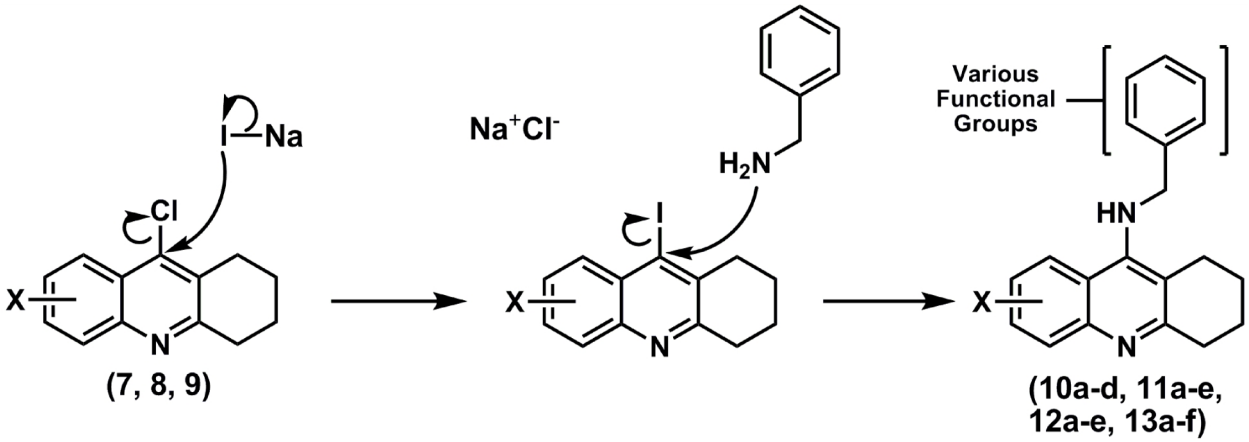

Figure 19: Reaction mechanism of amine coupling to THA catalyzed by NaI

The 9Cl-THA derivatives (**7**, **8**, or **9**, Fig. 19) were converted into the 6 or 7-chloro and unchlorinated benzylamine, substituted benzylamine, and picolylamine-substituted compounds (**10a-d, 11a-e, 12a-e**, **13a-f**, Fig. 19). The starting material (**7**, **8**, or **9**) was dissolved in a solvent which allows NaI to dissociate. The iodine ion displaces the chlorine located at C-9, thus creating a better leaving group for further nucleophilic attack (Fig. 19). The amine nucleophiles (substituted/unsubstituted benzylamine, or picolylamine) displace iodine at C-9 to afford the final test compound.

Reaction d (Fig. 19) was carried out in the presence of either phenol or butanol with NaI as a catalyst and run under reflux for 3 – 4.5 hours (Fig. 15). The resulting solution was dried under reduced pressure and re-dissolved in DCM then washed 3 times with concentrated brine solution (Fig. 13). The organic fraction was dried with $MgSO_4$ and evaporated under reduced pressure. The resulting product was purified via flash chromatography (solvent: DCM) with multiple rounds if necessary (Fig. 18). Product yields ranged from 12 – 47%.

3.3 Biological Evaluation

The biological profiles of synthesized compounds were evaluated, focusing on initial evaluation of i) ChE inhibition, followed by ii) antioxidant capacity, iii) chelation capacity, and finally evaluation of iv) cell viability in order to demonstrate the full SAR of top derivatives (Fig. 20).

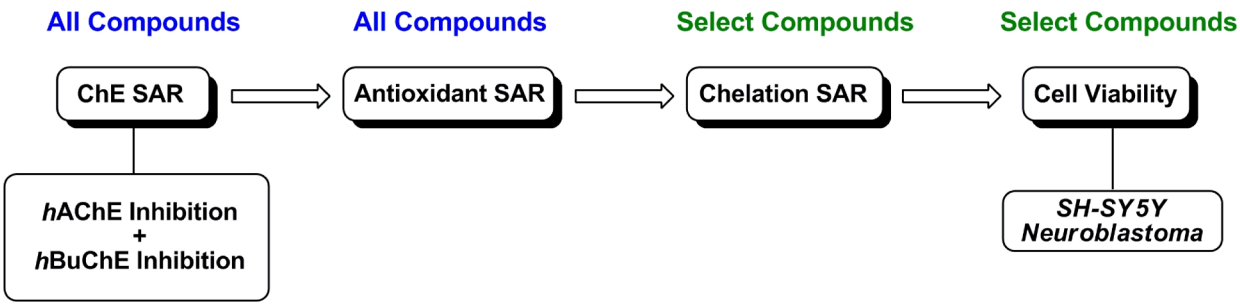

Figure 20: General outline of biological evaluation

3.3.1 Cholinesterase inhibition Assay

Inhibitory concentration (IC_{50}) values toward *h*AChE and *h*BuChE were determined for each test compound following the Ellman's method.[65] This colorimetric assay works by incubating test compounds with a solution containing either *h*AChE or *h*BuChE in the presence of a thiocholine analogue (acetylthiocholine or butyrylthiocholine). The ChEs hydrolyze their respective substrates to generate thiocholine, which will go on to react with 5,5'-dithiobis-(2-nitrobenzoic acid) (DTNB). This generates a yellow chromophore that is detected via UV-spectroscopy at 405-412 nm. Potent test compounds prevent ChE from hydrolyzing their respective substrates, thus preventing the generation of yellow chromophore. The general assay mechanism is illustrated in Figure 21.

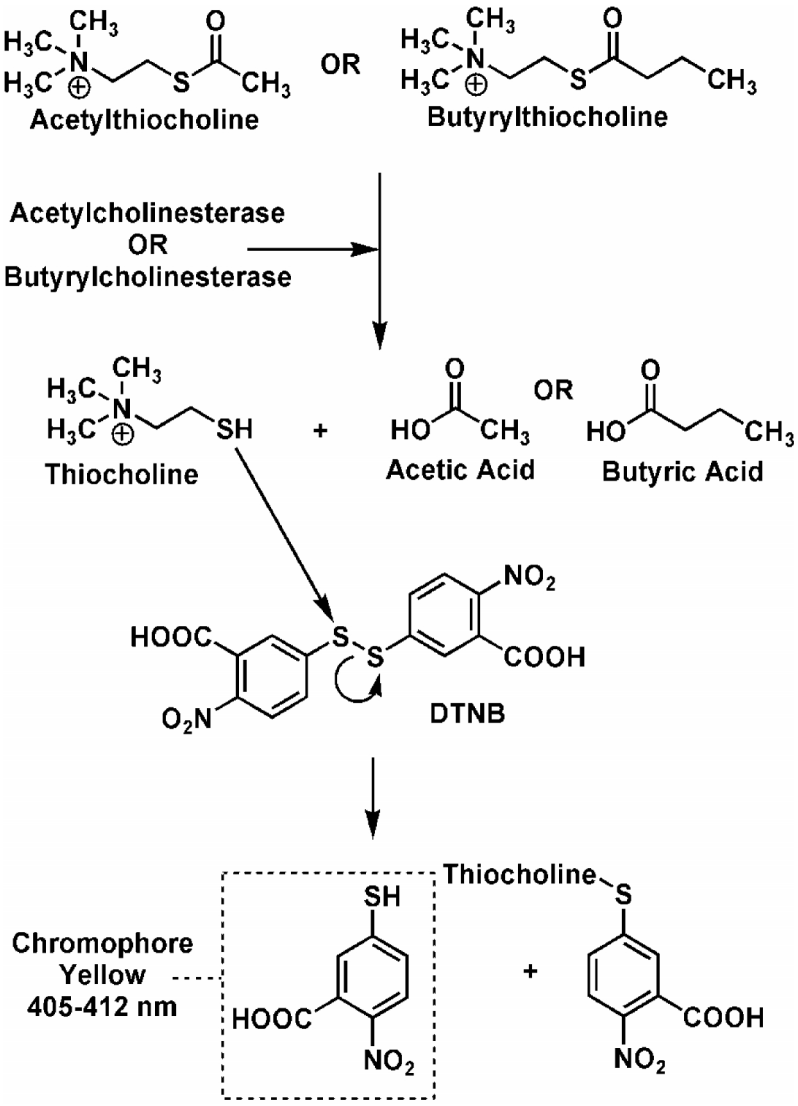

Figure 21: Mechanism of *h*AChE/*h*BuChE hydrolysis of acetylthiocholine/butyrylthiocholine and thiocholine interaction with DTNB to generate a yellow chromophore

3.4 Antioxidant Assay

The assessment of test compound capacity to scavenge ROS was accomplished via the 2,2-diphenyl-1-picrylhydrazyl (DPPH) assay protocol.[66] DPPH exists as a stable free radical in crystalline form where it takes on a purple colour (Fig. 22). It has an absorbance peak at a wavelength of 517 nm, which decreases when the free radical is quenched by an antioxidant. The colour change is directly proportional to the ability of molecules to act as potential antioxidants. The results were compared with reference agents curcumin and trolox.

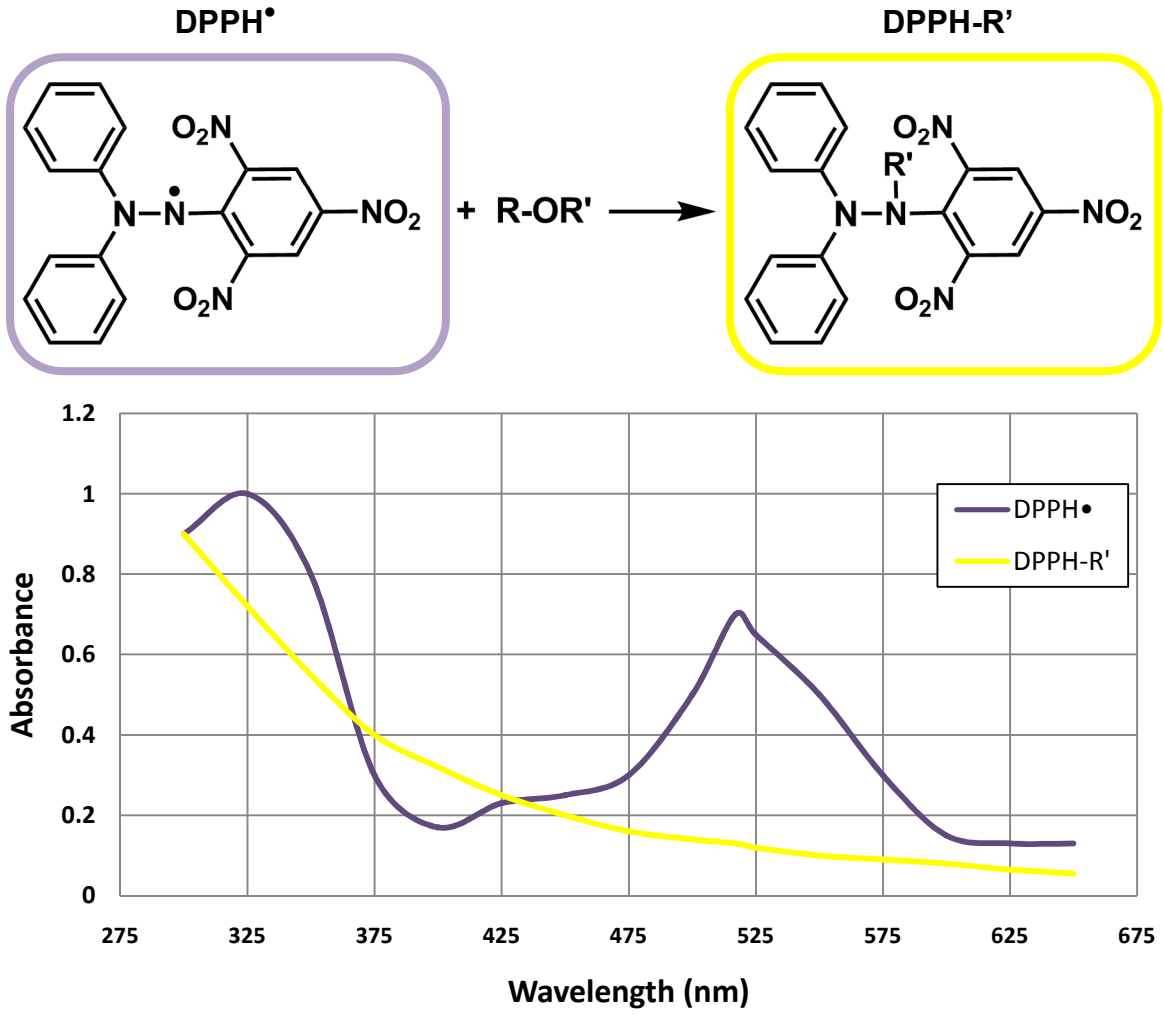

Figure 22: Absorbance shift of DPPH upon quenching of free radical

3.5 Chelation Assay

The metal-chelation assay protocol outlined by Karamac and coworkers, is a UV-vis spectroscopy-based experiment, which quantifies the chelation ability percentage of a given test compound.[67] It is a competitive assay where test compounds compete with ferrozine, a known chelator. The ability of test compounds to chelate iron can be monitored by a decrease in absorbance at 562 nm.

As a competitor chelator is introduced, it will begin to chelate the Fe^{2+} or Fe^{3+} ions resulting in a decrease in the absorbance at 562 nm (Fig. 22).

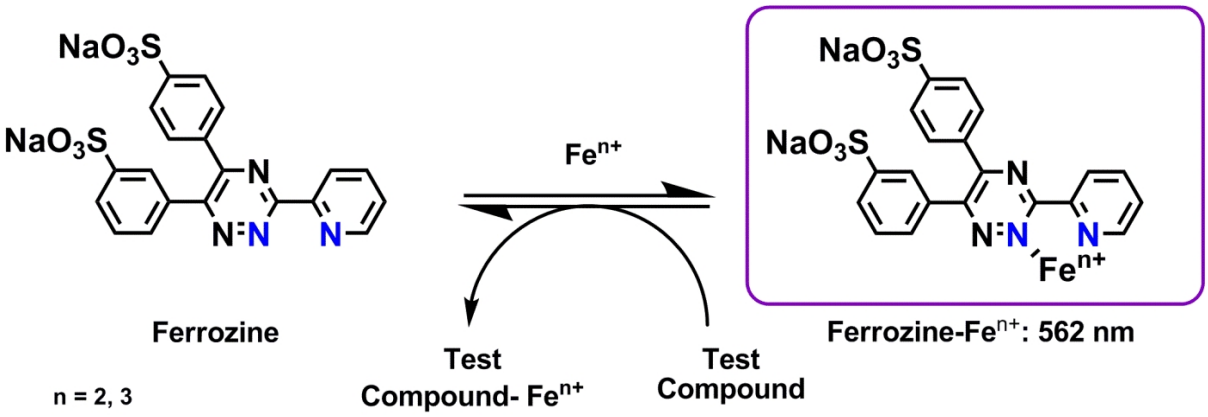

Figure 23: Shift in ferrozine absorbance upon iron chelation. Inhibition of ferrozine chelation and absorbance shift due to test compound chelation of iron

3.6 Evaluation of Cell Viability

The screening of cell viability follows a previously outlined methodology by Mosman, known as the MTT assay protocol.[68] SH-SY5Y neuroblastoma cells, like other living cells, reduce the reagent 3-(4,5-dimethylthiazol-2-yl)-2,5-diphenyltetrazolium bromide (MTT reagent) from a yellow chromophore into a purple formazan (absorption at 570 nm) via activity of the mitochondrial dehydrogenase (MDH) (Fig. 24). As cells die, MDH activity of the enzyme is reduced and the reduction of MTT reagent does not occur and is directly correlated to the percent

of living cells in a culture. This can be correlated to the toxicity profile of a test compound by observing the relationship between test compound and its capacity to maintain cell viability.

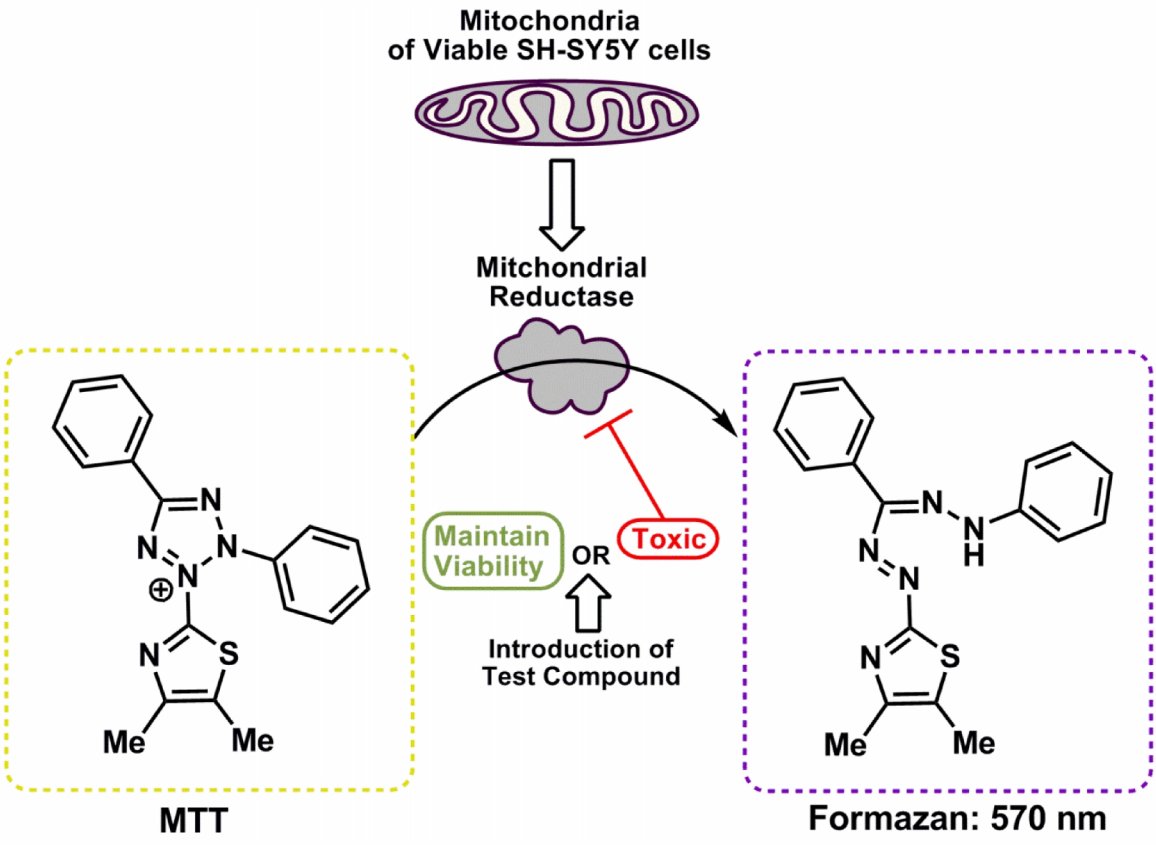

Figure 24: Mechanism of MTT assay with viable cell reduction of MTT to formazan

CHAPTER IV

Results and Discussion

4.1 Structure-Activity Relationship (SAR) Studies

Obtaining the relationship between different compound structures and their biological effects is an integral part of medicinal chemistry research. Structural modifications were utilized to assess the impact on the overall biological profile of target derivatives. This was ultimately done to answer the question of whether a series of THA derivatives could potentially target the cholinergic and oxidative stress pathways of AD.

4.2 Anti-cholinesterase Evaluation

The biological anti-ChE profiles of each compound were assessed. Two major classes of compounds make up the entirety of the chemical library developed based on C-9 groups: i) benzylamine and substituted benzylamine series; ii) picolylamine series.

4.2.1 Benzylamine and Substituted Benzylamine Series

The anti-ChE activity of test compounds carrying benzylamine and substituted benzylamine, are expressed as IC_{50} values; the concentration of test compound required to inhibit 50% of ChE enzyme activity. Selectivity indices (SI) indicate the selectivity of test compounds toward ChE enzymes with higher numbers indicating AChE selectivity. Other molecular parameters such as partition coefficient (ClogP), and molecular volume (MV – $Å^3$) are also given in Table 1.

Table 1: ChE IC_{50} values, SI, ClogP, and MV for benzylamine and substituted benzylamine compounds (**10a-d, 11a-e,** and **12a-e**)

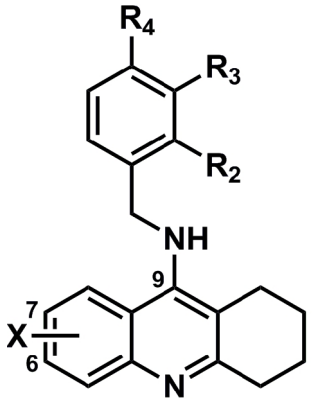

10a-d, 11a-e, 12a-e

Cpd	C-6	C-7	R_2	R_3	R_4	ChE IC_{50} (µM)[a]		SI[b]	ClogP[c]	MV[d] ($Å^3$)
						AChE	BuChE			
10a	H	H	H	H	H	6.96	0.41	0.059	5.52	203.39
10b	H	H	OMe	H	H	5.81	0.089	0.015	5.44	223.98
10c	H	H	H	OMe	H	3.34	0.079	0.024	5.44	223.98
10d	H	H	H	OMe	OMe	2.23	0.024	0.011	5.18	249.36
11a	Cl	H	H	H	H	1.67	3.99	2.4	6.33	219.05
11b	Cl	H	OMe	H	H	2.98	2.38	0.8	6.25	237.76
11c	Cl	H	H	OMe	H	0.61	5.22	8.6	6.25	237.76
11d	Cl	H	H	H	OMe	0.72	9.10	12.6	6.25	237.76
11e	Cl	H	H	OMe	OMe	0.85	1.40	1.6	5.99	260.33
12a	H	Cl	H	H	H	2.59	12.11	4.7	6.33	219.05
12b	H	Cl	OMe	H	H	5.1	4.25	0.83	6.25	237.76
12c	H	Cl	H	OMe	H	1.89	8.25	4.4	6.25	237.76
12d	H	Cl	H	H	OMe	3.37	11.65	3.5	6.25	237.76
12e	H	Cl	H	OMe	OMe	1.26	9.27	7.4	5.99	260.33
Tacrine – Cognex®						0.215	0.050	0.41	3.27	139.90
Donepezil – Aricept®						0.03	3.60	0.009	4.60	271.00
Galantamine – Reminyl®						3.20	12.60	0.3	1.00	179.20

[a]IC_{50} values are the average of two to three separate experiments (duplicates/n = 2) with mean deviation of < 10% of average. [b]SI = *h*BuChE IC_{50}/*h*AChE IC_{50}. [c]ClogP was determined using ChemDraw UIltra v11.0 Cambridge Software Company. [d]MV was calculated using the Discovery Studio from Accelrys Inc.

The SAR data for this class of compounds indicates that they exhibit cholinesterase inhibition from nM to μM range (*h*AChE IC_{50} 61 nM - 6.96 μM; *h*BuChE IC_{50} 0.61; 24 nM - 11.65 μM). In the substituted 1,2,3,4-tetrahydroacridin-9-amine series of compounds **10a-d**, the presence of a benzyl substituent at C-9 position in **10a** provided dual inhibition of both AChE and BuChE. This compound was a selective BuChE inhibitor (BuChE IC_{50} = 0.41 μM). The addition of an OMe substituent *ortho* (R_2 = OMe, R_3 = R_4 = H) to C-9 benzyl group in **10b** led to a 4.6-fold increase in its potency toward BuChE (IC_{50} = 89 nM) and a moderate gain in AChE inhibition (IC_{50} = 5.81 μM) relative to **10a**. Furthermore, regioisomeric replacement of *ortho*-OMe substituent with a *meta*-OMe (R_2 = H, R_3 = OMe, R_4 = H) as in **10c** provided further enhancement in BuChE inhibitory potency (IC_{50} BuChE = 79 nM) and further gain in AChE inhibitory potency (IC_{50} = 3.34 μM). Interestingly, the presence of a 3,4-diOMe substituent as in compound **10d** (R_2 = H, R_3 = R_4 = OMe), provided the best combination of dual cholinesterase inhibition among this series. Compound **10d** was the most potent BuChE inhibitor in this series (IC_{50} = 24 nM) and was much more potent relative to reference agents tacrine, donepezil and galantamine (Table 1). Furthermore, this compound was the most potent AChE inhibitor in this series (AChE IC_{50} = 2.23 μM). The AChE inhibitory potency order was 3,4-*di*OMe (**10d**) > 3-OMe (**10c**) > 2-OMe (**10b**) > H (**10a**). It is interesting to note that all compounds in this series exhibited selective inhibition of BuChE enzyme.

In the 6-chloro-substituted-1,2,3,4-tetrahydroacridin-9-amine series of compounds **11a-e**, the presence of a C-6 chlorine atom had a dramatic effect on BuChE inhibition and resulted in weaker inhibition relative to substituted 1,2,3,4-tetrahydroacridin-9-amine series of compounds **10a-d**. In contrast, the presence of the C-6 chlorine led to superior AChE inhibition (AChE IC_{50} = 0.61-2.98 μM). Compounds **11c-d** (AChE IC_{50} = 0.61 - 0.85 μM range) exhibited better AChE

inhibitory potency relative to galantamine although they were not as potent as tacrine (Table 1). It appears that for this class of compounds, the BuChE inhibition was sensitive to both the presence of C-6 chlorine and the position of OMe substituents. For example the presence a *para*-OMe substituent (R_2 = H, R_3 = H, R_4 = OMe) as in compound **11d**, led to weak inhibition of BuChE (IC_{50} = 9.1 μM). The compound with a good combination of dual AChE and BuChE inhibition in this series was **11e** with a 3,4-diOMe-substituent (AChE IC_{50} = 0.85 μM; BuChE IC_{50} = 1.4 μM) whereas compound **11c** was the most potent AChE inhibitor (IC_{50} = 0.61 μM). It is interesting to note that all the compounds in this series except compound **11b**, exhibited selective inhibition of AChE.

In the 7-chloro-substituted-1,2,3,4-tetrahydroacridin-9-amine series of compounds **12a-e**, the presence of a C-7 chlorine decreased both AChE and BuChE inhibition and potency relative to C-6 series (AChE IC_{50} = 1.26 - 5.10 μM range and BuChE IC_{50} = 4.25 - 11.65 μM range, Table 1). Compound **12e** (3,4-diOMe, R_2 = H, R_3 = R_4 = OMe) was the most potent AChE inhibitor in this series (AChE IC_{50} = 1.26 μM) whereas compound **12b** with an *ortho*-OMe (R_2 = OMe, R_3 = R_4 = H) substituent was the most potent BuChE inhibitor (BuChE IC_{50} = 4.25 μM). Similar to the 6,9-chloro-substituted-1,2,3,4-tetrahydroacridin-9-amine series of compounds, they all exhibited better AChE selectivity except for compound **12b**.

The ClogP values, a measure of partition coefficient, for this series of compounds calculated computationally were in the range of 5.18 to 6.33 (donepezil ClogP = 4.60) which indicates their ability to cross the blood brain barrier. However, it should be noted that ClogP values for the 6 and 7-chloro-substituted-1,2,3,4-tetrahydroacridin-9-amine series of compounds **11a-e** and **12a-e** are relatively high which suggests potential toxicity concerns. In contrast, the lack of chlorine in the substituted-1,2,3,4-tetrahydroacridin-9-amine series of compounds **10a-d**

provided acceptable ClogP values (ClogP = 5.18-5.52, Table 1). Furthermore, the molecular volume of these compounds was in a range of 203.39 to 260.33 $Å^3$ which indicates their ability to bind to both AChE and BuChE enzymes and exhibit dual inhibition.

In summary, these studies indicate that the presence of chlorine at either C-6 or C-7 position of the tetrahydroacridine ring had a significant impact on AChE inhibition and potency. Figures 25 and 26 compare the relative potencies of these compounds toward AChE and BuChE. The presence of a C-6 chlorine provided superior AChE inhibition (**11a-e**) whereas regioisomeric placement of chlorine at C-7 led to a decrease in AChE and BuChE inhibitory potency (**12a-e**). In contrast, non-chlorinated 1,2,3,4-tetrahydroacridin-9-amine derivatives (**10a-d**) exhibited selective and nM potency toward BuChE inhibition.

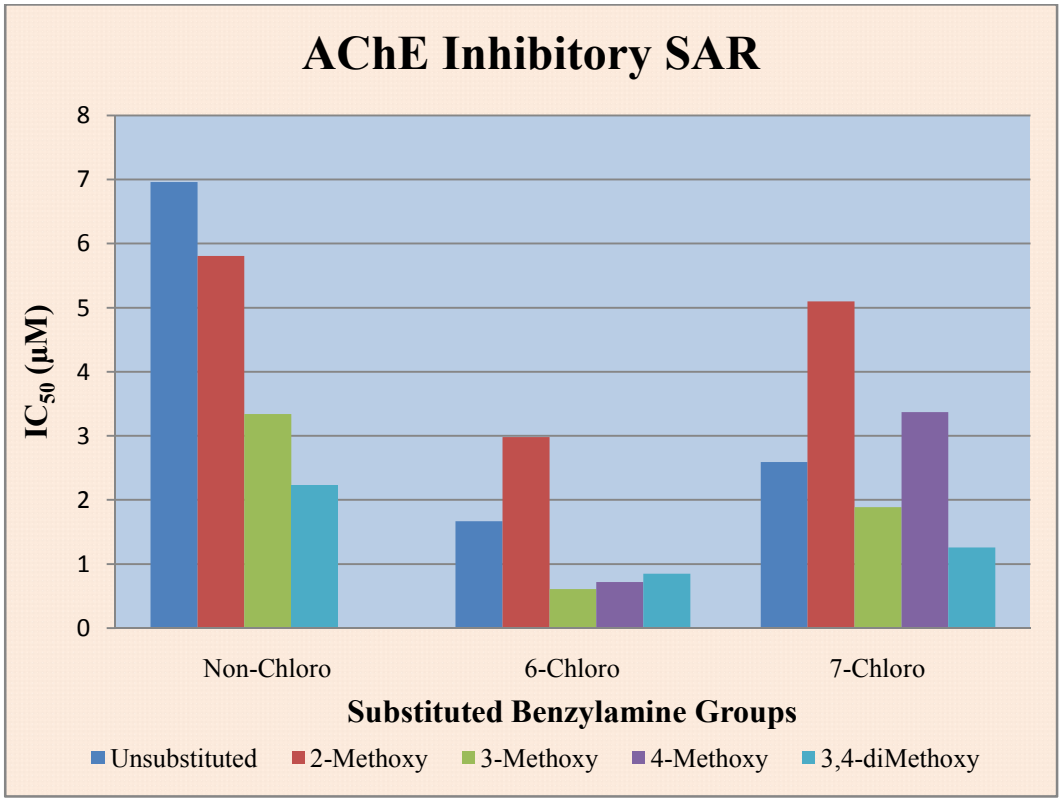

Figure 25: Summary of AChE IC_{50} values of benzylamine and substituted benzylamine series of compounds

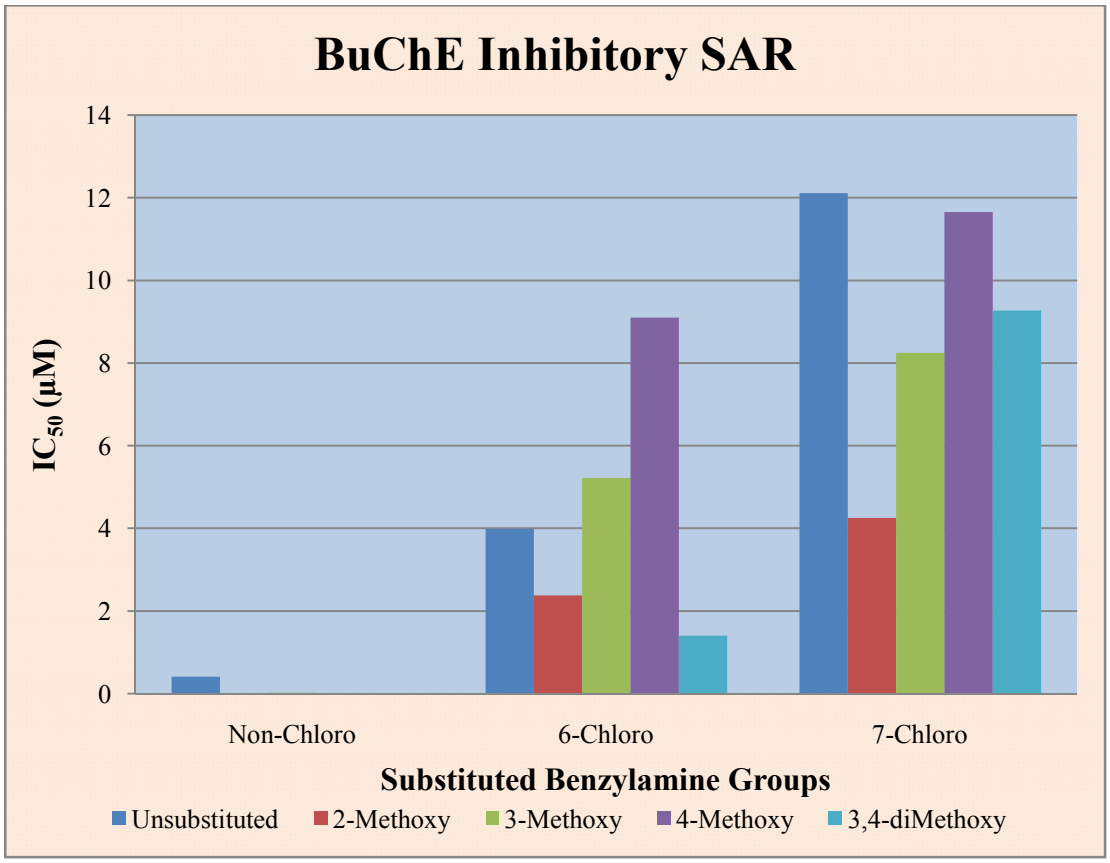

Figure 26: Summary of BuChE IC_{50} values of benzylamine and substituted benzylamine series compounds

AChE IC_{50} = 2.23 µM
BuChE IC_{50} = 0.024 µM

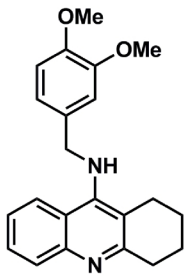

10d

***N*-(3,4-dimethoxybenzyl)-1,2,3,4-tetrahydroacridin-9-amine**

AChE IC_{50} = 0.61 µM
BuChE IC_{50} = 5.22 µM

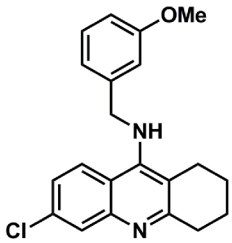

11c

6-chloro-*N*-(3-methoxybenzyl)-1,2,3,4-tetrahydroacridin-9-amine

AChE IC_{50} = 0.85 µM
BuChE IC_{50} = 1.40 µM

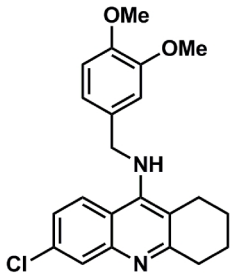

11e

6-chloro-*N*-(3,4-dimethoxybenzyl)-1,2,3,4-tetrahydroacridin-9-amine

Figure 27: Top ChEI from the benzylamine and substituted benzylamine series

4.2.2 Picolylamine Series

The anti-ChE activity of test compounds carrying picolylamine groups are expressed as IC_{50} values. Selectivity indices (SI) indicate the selectivity of test compounds toward ChE enzymes with higher numbers indicating AChE selectivity. Other molecular parameters such as partition coefficient (ClogP), and molecular volume (MV – $Å^3$) are also given in Table 2.

Table 2: ChE IC_{50} values, SI, ClogP, and MV for picolylamine derivatives; compounds (**13a-f**)

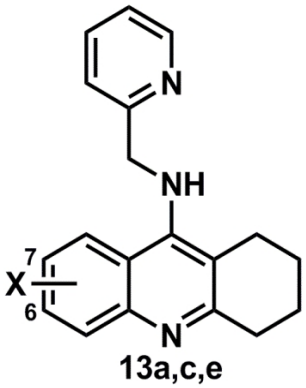

13a,c,e

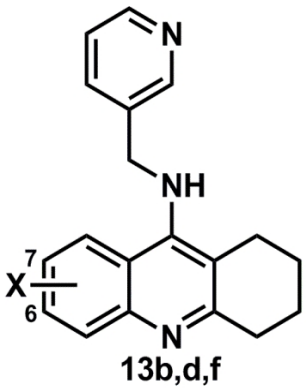

13b,d,f

Cpd	C-6	C-7	ChE IC_{50} (µM)[a]		SI[b]	ClogP[c]	MV ($Å^3$)[d]
			AChE	BuChE			
13a	H	H	6.65	0.073	0.011	4.02	201.00
13b	H	H	3.99	0.223	0.056	4.02	201.00
13c	Cl	H	0.095	1.61	16.9	4.83	215.74
13d	Cl	H	0.19	12.73	67.0	4.83	215.74
13e	H	Cl	7.06	6.78	0.96	4.83	215.74
13f	H	Cl	7.69	>25	-	4.83	215.74
Tacrine – Cognex®			0.215	0.050	0.41	3.27	139.90
Donepezil – Aricept®			0.03	3.60	0.009	4.60	271.00
Galantamine – Reminyl®			3.20	12.60	0.3	1.00	179.20

[a]IC_{50} values are the average of two to three separate experiments (duplicates/n = 2) with mean deviation of < 10% of average value. [b]SI = *h*BuChE IC_{50}/*h*AChE IC_{50}. [c]ClogP was determined using ChemDraw UIltra v11.0 Cambridge Software Company. [d]MV was calculated using the Discovery Studio from Accelrys Inc.

In order to explore the effect of aromatic heterocycles at the C-9 position of the THA template, derivatives (**13a-f**, Table 2) that contain either a 2- or 3-pyridyl ring were evaluated for their ability to inhibit ChE enzymes. Interestingly, compound **13a** which is the 2-pyridyl isomer of compound **10a**, was about 5.6-fold more potent toward BuChE enzyme (BuChE IC_{50} = 73 nM) compared to compound **10a**. However, this modification did not affect its AChE inhibition (AChE IC_{50} = 6.96 μM). The presence of a 3-pyridyl substituent in **13b**, provided superior BuChE inhibition (IC_{50} BuChE = 0.223 μM) relative to **10a**, although it was not as potent as **13a**. In contrast, **13b** exhibited superior AChE inhibition (AChE IC_{50} = 3.99 μM) compared to both **10a** and **13a** (Table 1 and 2). Both **13a** and **13b** exhibited selective BuChE inhibition which was similar to the trend seen with compounds **10a-d** (Table 1). Interestingly, the combination of a C-6 chlorine and a 2-pyridyl substituent in **13c** provided the most potent AChE inhibitor in the entire compound library with nanomolar inhibition (AChE IC_{50} = 95 nM, Table 2). **13c** is more than twice as potent in AChE inhibition (AChE IC_{50} = 95 nM) relative to reference agent tacrine (AChE IC_{50} = 215 nM, Table 2). However, the addition of C-6 chlorine in compound **13c** was detrimental to BuChE inhibition (BuChE IC_{50} = 1.61 μM) compared to **13a**. Similarly, compound **13d** with a 3-pyridyl substituent was the second most potent AChE inhibitor (AChE IC_{50} = 0.19 μM) identified in our compound library after **13c**. However, **13d** exhibited weak BuChE inhibition (BuChE IC_{50} = 12.73 μM). In contrast, the C-7-chlorinated pyridyl isomers, **13e** and **13f**, turned out to be poor ChE inhibitors (AChE IC_{50} range: 7.06 - 7.69 μM; BuChE IC_{50} range: 6.78 μM to no inhibition at 25 μM test concentration). It should be noted that the C-9 pyridyl series of compounds were less lipophilic relative to compounds **10a-d**, **11a-e** and **12a-e** series of compounds and exhibited ClogP values in the range of 4.02-4.83 which was comparable to the marketed anti-AD agent donepezil (ClogP = 4.60, Table 1).

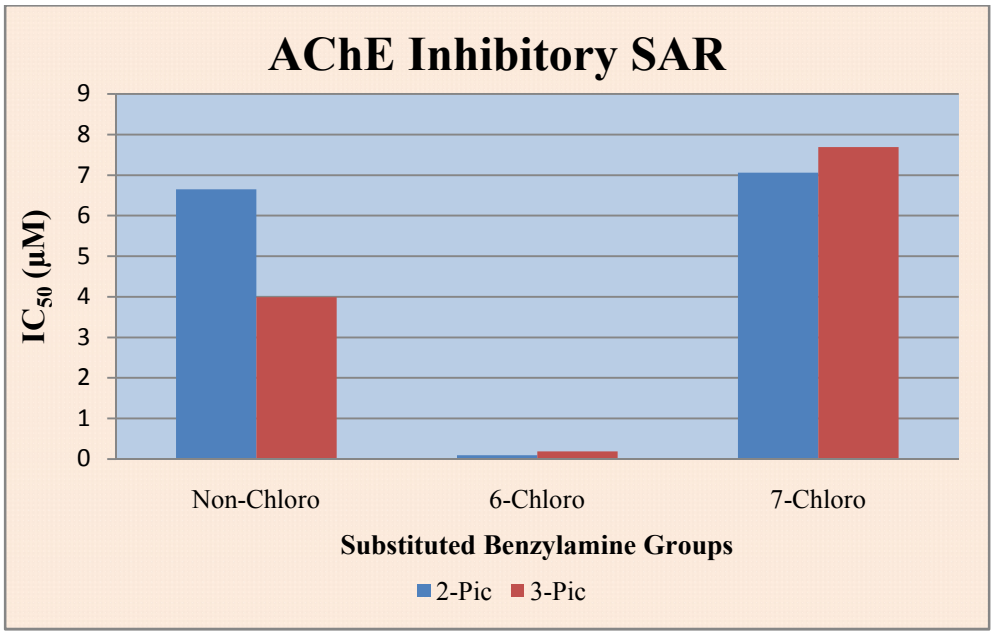

Figure 28: Summary of AChE IC_{50} values of picolylamine series of compounds

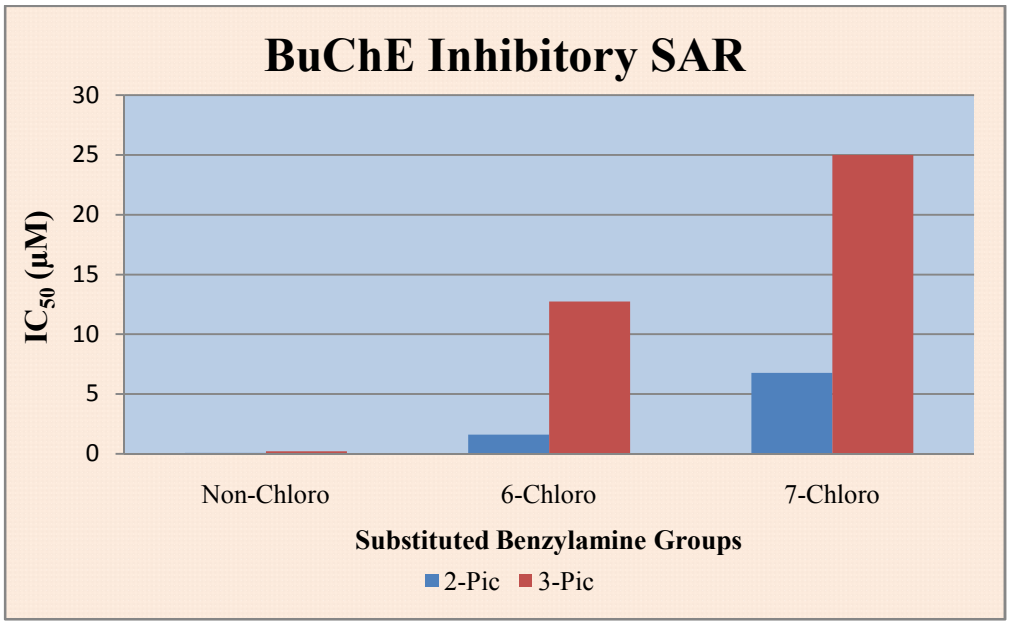

Figure 29: Summary of BuChE IC_{50} values of picolylamine series of compounds

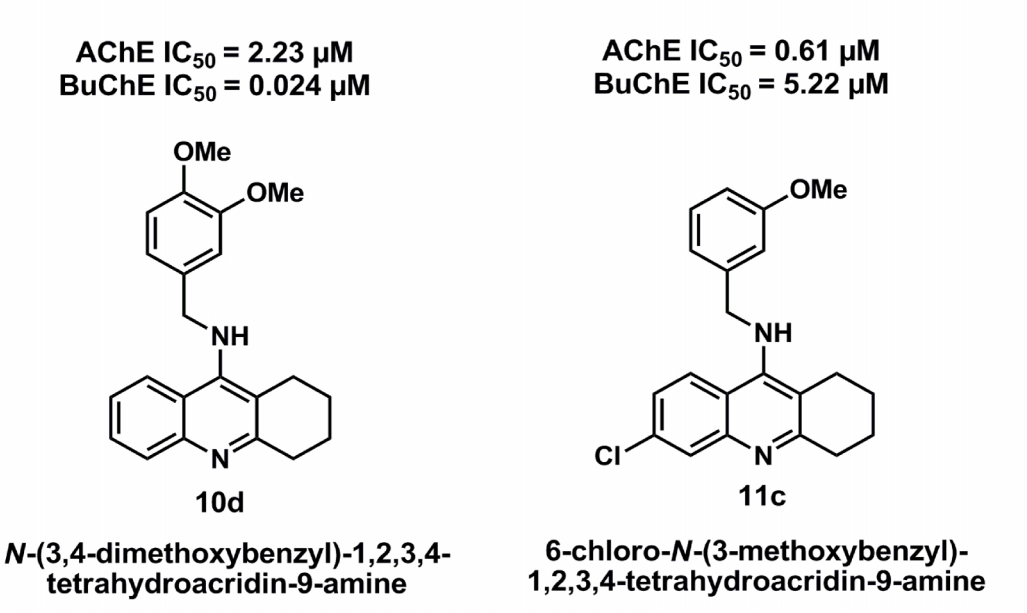

Figure 30: Top ChEI from the picolyl series of derivatives

Our SAR studies suggest that in general, BuChE inhibition was sensitive to electronic and steric parameters at C-9 position of the tetrahydroacridine ring whereas a chlorine substituent at either the C-6 or C-7 position modulated AChE inhibition.

4.3 Antioxidant Capacity Evaluation

The biological antioxidant profiles of test compounds were assessed. Two major classes of compounds make up the entirety of the chemical library developed: i) benzylamine and substituted benzylamine; ii) picolylamine series.

4.3.1 Benzylamine and Substituted Benzylamine Series

The antioxidant activity of test compounds carrying benzylamine, and substituted benzylamine are expressed as a percent inhibition at 100 µM which gives the ability of test compounds to scavenge DPPH free radical.

Table 3: DPPH percent inhibition (%) values for benzylamine and substituted benzylamine; compounds (**10a-d, 11a-e, 12a-e)**

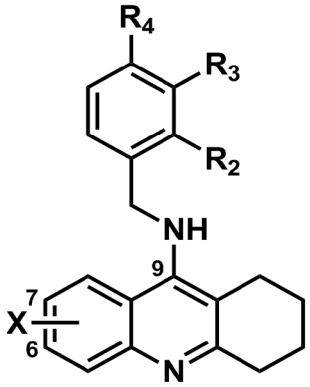

10a-d, 11a-e, 12a-e

Cpd	C-6	C-7	R_2	R_3	R_4	Percent Inhibition (%) at 100 μM[a]
10a	H	H	H	H	H	12.3
10b	H	H	OMe	H	H	10.4
10c	H	H	H	OMe	H	8.5
10d	H	H	H	OMe	OMe	9.3
11a	Cl	H	H	H	H	10.8
11b	Cl	H	OMe	H	H	10.8
11c	Cl	H	H	OMe	H	7.9
11d	Cl	H	H	H	OMe	9.5
11e	Cl	H	H	OMe	OMe	7.2
12a	H	Cl	H	H	H	9.0
12b	H	Cl	OMe	H	H	6.3
12c	H	Cl	H	OMe	H	10.4
12d	H	Cl	H	H	OMe	8.1
12e	H	Cl	H	OMe	OMe	10.9
Trolox						91.5
Curcumin						68.8

[a]Percent inhibition values are the average of two separate experiments (duplicate/n = 2) with mean deviation < 10% of average value.

The benzyl and substituted benzylamine series of compounds demonstrated percent inhibitions of the DPPH radical between 6 - 11 %.

Comparing the compounds in Table 3 to the chemical structures of curcumin (Fig. 5) it can be seen that the presence of a phenolic group is responsible for their antioxidant properties (curcumin: 68.8 % inhibition, trolox: 91.5% inhibition). The test compounds do not possess phenolic groups. Although they have methoxy groups, they are not considered as effective antioxidants as was seen with their weak DPPH scavenging (% inhibition: 6.3 – 12.3%).

4.3.2 Picolylamine Series

The antioxidant activity of test compounds carrying picolylamine groups are expressed as percent inhibition at 100 μM.

Table 4: DPPH percent inhibition (%) values for picolylamine derivatives **13a-f**

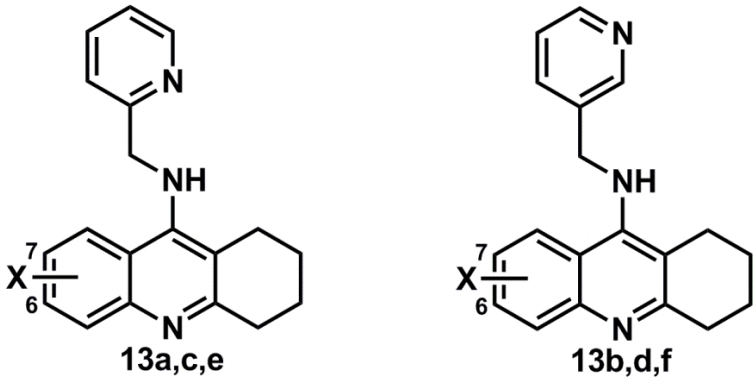

Cpd	C-6	C-7	Percent Inhibition (%) at 100 μM[a]
13a	H	H	11.0
13b	H	H	7.8
13c	Cl	H	7.2
13d	Cl	H	5.9
13e	H	Cl	11.5
13f	H	Cl	7.9
Trolox			91.5
Curcumin			68.8

[a]Percent inhibition values are the average of two separate experiments (duplicate/n = 2) with mean deviation < 10% of average value.

Like the substituted benzylamine series, the picolyl series of THA derivatives exhibit percent inhibitions between 5.9 – 11.5% (Table 4) and thus demonstrate negligible antioxidant effects.

When comparing the picolyl series for their antioxidant capacities to that of the reference compounds (curcumin: 68.8% inhibition, trolox: 91.5% inhibition), it can be seen that the phenolic group is a driving force in antioxidant capacity. Therefore, the picolyl series of compounds are not effective antioxidants due to their by their weak DPPH scavenging capacity (% inhibition: 5.9 – 11.5%), suggesting 2- or 3- pyridyl groups do not possess antioxidant properties.

4.4 Metal Chelation

The iron chelation capacity of picolyl-type derivatives was determined via UV analysis in the Fe(II)-ferrozine competition assay. The chelation capacity of test compounds is expressed as percent chelation.

Table 5: Percent iron chelation (%) values for picolylamine derivatives **13a-f**

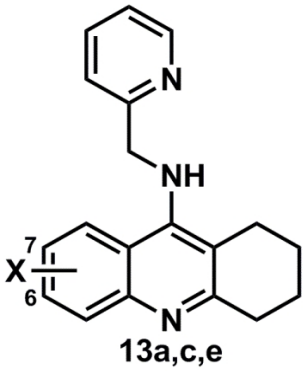

13a,c,e

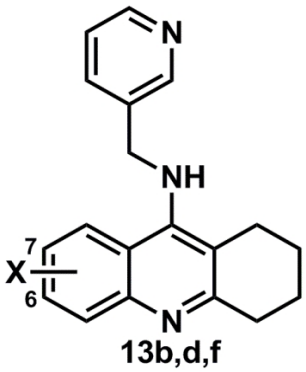

13b,d,f

Cpd	C-6	C-7	Percent Chelation (%) at 50 μM[a]
13a	H	H	9.4
13b	H	H	11.0
13c	Cl	H	14.5
13d	Cl	H	10.2
13e	H	Cl	20.2
13f	H	Cl	10.4
Clioquinol			63.5
Desferoxamine			67.1

[a]Percent chelation values are the average of two separate experiments (duplicate/n = 2) with mean deviation < 10% of average value.

From Table 5, the relative percent chelation of test compounds range from 9.4 -20.2% while references clioquinol and desferoxamine have percent chelation of 63 and 67%, respectively. The C-9, 2-pyridyl series of compounds, **13a**, **13c**, and **13e**, can form a chelating center. Despite this, these compounds exhibited weak to moderate iron chelation. The maximum chelation was seen for compound **13e** (20.2%, Table 5). This can be explained by the presence of an sp^3 hybridized methylene ($-CH_2$) group at C-9 that leads to bond rotation and hinders the formation of a rigid chelation center. The weak iron chelation capacity exhibited by the 3-pyridyl series of compounds **13b**, **13d**, and **13f**, is not surprising since they do not form a chelation center as the pyridyl nitrogen is at a greater distance from the C-9 secondary amine, relative to the 2-pyridyl series of compounds.

4.5 Evaluation of Cell Viability

The toxicity profiles of test compounds **10b-d**, **11c,e**, and **13a-d** were evaluated using the MTT assay protocol in order to assess their potential toxicity. Compounds were tested at 25 μM, 50 μM concentrations along with reference compound tacrine.

Table 6: Percent viability of SH-SY5Y neuroblastoma cell line after treatment with test compounds

Cpd	Percent Viability at 25 μM (%)[a,b]	Percent Viability at 50 μM (%)[a,b]	ClogP[c]
10b	54.1	20.3	5.44
10c	95.5	26.8	5.44
10d	93.8	84.2	5.18
11c	2.8	1.7	6.25
11e	81.8	40.5	5.99
13a	58.9	47.2	4.02
13b	100.0	82.1	4.02
13c	75.4	18.1	4.83
13d	80.6	96.6	4.83
Tacrine	89.6	81.1	3.27

[a]Data is expressed as mean ± SD, (n = 3) ANOVA analysis with Dunnett's post-test. [b]Derivative's cell viability data obtained from the collaboration with Dr. Beazely's group. [c]ClogP was determined using ChemDraw Ulltra v11.0 Cambridge Software Company

From Table 6, the range of cell viability for selected test compounds ranged from as low as 1.7% to as high as 100% viability. Compounds chosen from Table 1 and Table 2 were those that demonstrated potent ChEI activity.

It was observed that for compounds **10b**, **10c**, and **10d**, the presence of a dimethoxy-substituted benzyl group (**10d**) significantly improved the cell viability at a concentration as high as 50 μM (84.2%) compared to mono-OMe compounds, **10b** and **10c** (cell viability = 20.3 – 26.8%, respectively). This can be attributed to the difference in ClogP values between the mono versus diOMe compounds. The increased ClogP of **10b** and **10c** led to increased cell toxicity as

compared to the diOMe compound, **10d** (cell viability = 93.8 and 84.2% at 25 µM and 50 µM, respectively). However, it may not be the ClogP values alone which dictate cell viability. We also see that the mono-OMe derivative **11c** with one of the highest ClogP values in the chemical library (6.25) promotes significant cell death in the neuroblastoma cell line at both 25 µM and 50 µM. Finally, the picolylamine series of compounds (Table 2) had lower ClogP values (Table 6) as compared to the substituted benzylamine series. Compounds **13b** and **13d** exhibited good cell viability at both 25 µM and 50 µM concentrations (100%, 82.1%, and 80.6%, 96.6%, respectively). However, compounds **13a** and **13c** were toxic to cells at 50 µM (Table 6). These studies indicate that the cell viability was sensitive to both the ClogP values as well as the nature of substituents at C-6, C-7, and C-9 positions.

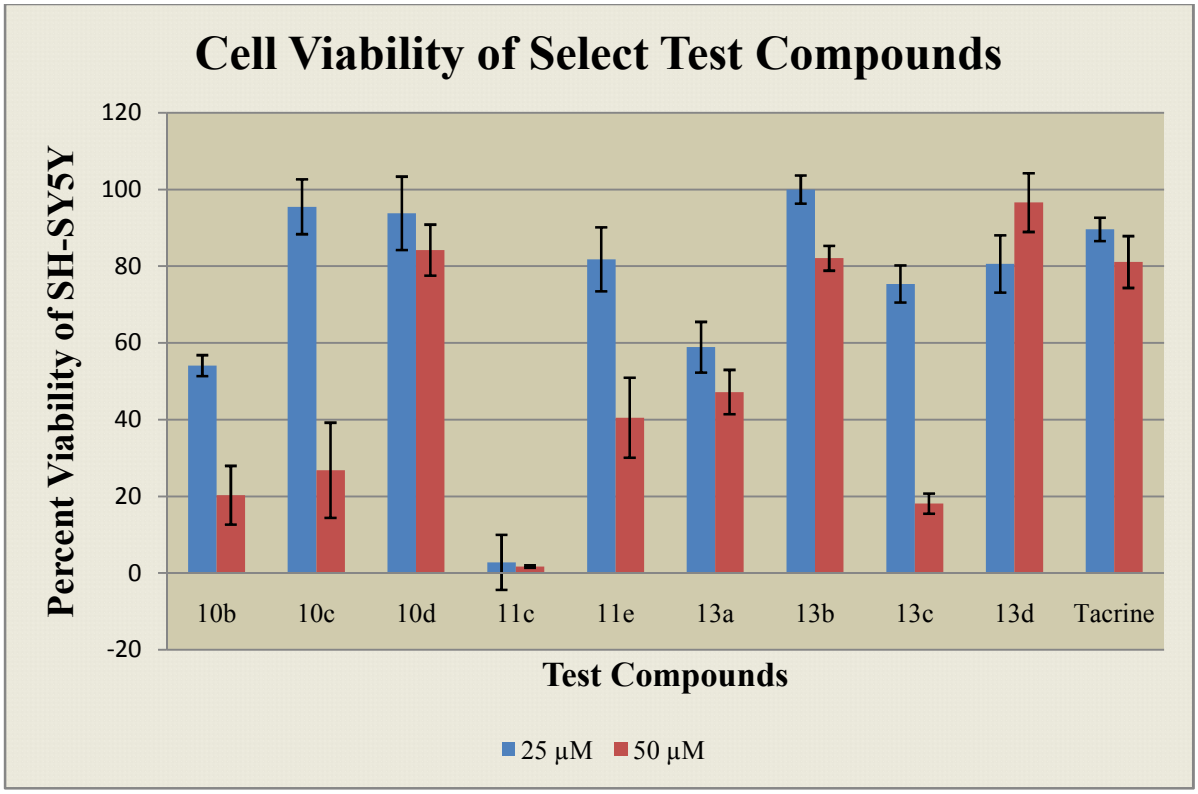

Figure 31: Summary of cell viability percentages of THA test compounds after 24 h incubation with SH-SY5Y neuroblastoma cells. Control (not shown) represents 100% viability. Error bars represent average of standard error.

4.6 Molecular Modeling

Computational modeling studies were utilized to help corroborate and better understand the findings determined in the biological ChE evaluation of test compounds. This section aims to describe the binding modes of a few potent ChEI and their comparisons within *h*AChE and *h*BuChE active sites. Only key residues are highlighted with hydrogen atoms removed for clarity.

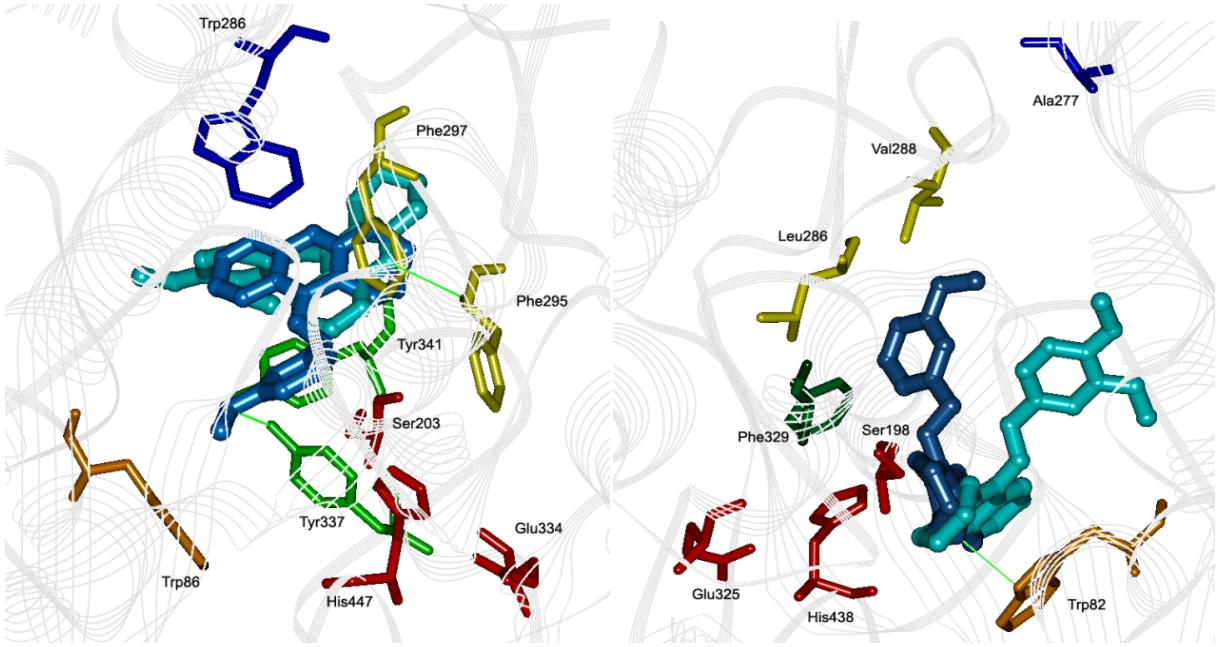

Figure 32: Docking of *N*-(3-methoxybenzyl)-1,2,3,4-tetrahydroacridin-9-amine (**10c**, light blue ball and stick) and *N*-(3,4-dimethoxybenzyl)-1,2,3,4-tetrahydroacridin-9-amine (**10d**, dark blue, ball and stick) in the active site of *h*AChE (left) and *h*BuChE (right). Green lines represent hydrogen bonding (distance < 3.5 Å). Hydrogen atoms are not shown for clarity. *Red*: Catalytic triad; *Orange*: Cationic site; *Yellow*: Acyl pocket; *Green*: Stabilizing residues; *Blue*: PAS (AChE) and PAS analogue (BuChE)

The binding mode of **10c** in *h*AChE (PDB: 1B41) (Fig. 32) demonstrates an almost planar orientation whereby the THA moiety of the compound is located in the PAS with its nitrogen group forming strong hydrophobic interactions with Trp286 (distance ≈ 3.4 Å). The aliphatic ring of THA also spans into the acyl pocket where it interacts with Phe295 (distance ≈ 3.2 Å), and interacts with Tyr341 (distance ≈ 4.9 Å). Moving further toward the active site, the

C-9 amine forms strong van der Waals interactions with residues Tyr341 and Tyr337 (distance ≈ 4.3 Å and 4.0 Å, respectively). Finally, the C-9 group extends into the active site where it interacts with the catalytic Ser203 and His447 (distance ≈ 4.7 Å and 5.1 Å, respectively). The methoxy group also anchors the molecule within the active site by forming hydrogen bonds with Tyr337 (distance ≈ 3.5Å), and leans against Trp86 (distance ≈ 3.8 Å). Overall this compound spans the length of the PAS and acyl pocket, even interacting with catalytic and cationic site residues, which explains its AChE inhibition (IC_{50} = 3.34 μM; **10c** MV = 223.98 $Å^3$).

The addition of a diOMe-benzyl substituent to the C-9 group in **10d** proved to have a significant effect in the compound binding mode within the AChE active site. **10d** is oriented such that its THA moiety leans entirely against the acyl pocket where the THA nitrogen forms direct hydrogen bonding interactions with Phe295 (distance ≈ 3.3 Å). The C-9 amine forms van der Waals contacts with Trp286 and Tyr341 (distance ≈ 4.5 Å and ~ 4.3 Å, respectively). The C-9 group is rotated about its axis such that it is perpendicular to the THA base. The molecule is mostly PAS localized with the C-9 group protruding out of the enzyme. Overall the compound creates a stable plug through hydrophobic and hydrogen bonding interactions in the acyl pocket and PAS thus preventing substrates from entering AChE. These observations indicate its superior AChE inhibition (IC_{50} = 2.23 μM) relative to **10c**.

When comparing **10c** and **10d** we find that although their spatial orientation in the enzyme differs, they are both mostly PAS localized and are stabilized by several polar and non-polar interactions with residues in this region, thus they act to block entry of substrates into the enzyme active site.

The binding mode of **10c** differs significantly when observed in *h*BuChE (PDB: 1PO1). The molecule sits between the cationic and catalytic site with the THA nitrogen forming a direct

hydrogen bond with Trp82 (distance ≈ 3.4 Å). The fused benzyl ring of THA also forms hydrophobic interactions with His438 (distance ≈ 3.6 Å). The molecule sits at an angle to Trp82 with the C-9 group of the molecule directed into the acyl pocket. The C-9 amine also interacts with aromatic residue Phe329 (distance ≈ 3.4 Å). The C-9 group is oriented perpendicularly to the THA base with the 3-methoxy group directed away from the catalytic site. The C-9 benzene ring interacts with both catalytic Ser198 and His438 (distance ≈ 4.4 Å) with the 3-methoxy group sitting between acyl pocket residues Leu286 (distance ≈ 3.8 Å from the backbone) and Val288 (distance ≈ 3.7 Å). Its superior and selective inhibition for BuChE (IC_{50} = 0.079 μM) can be attributed to the observations above that it forms strong hydrophobic and hydrogen bonding interactions with key residues in the active site. By blocking Trp82, as well as the catalytic and acyl pocket residues, it effectively prevents ACh hydrolysis.

The binding mode of **10d** in *h*BuChE differs by the slight angle in which it sits in the active site (Fig. 32). Unlike **10c**, **10d** lays parallel with Trp82 with the C-9 group pointing away from the catalytic triad. The THA nitrogen and carbons form hydrophobic interactions with Trp82 ranging from 3.9 – 4.3 Å away, thus completely covering the residue. The THA base also forms hydrophobic interactions between the fused benzene ring of Ser198 (distance ≈ 4.9 Å) and the aliphatic ring of His438 (distance ≈ 4.5 Å). The C-9 group is rotated such that its benzene ring is perpendicular to THA with the 3-OMe substituent interacting with the backbone of Trp82 (distance ≈ 3.6 Å). This explains the potent BuChE inhibition seen with **10d** (IC_{50} = 0.024 μM).

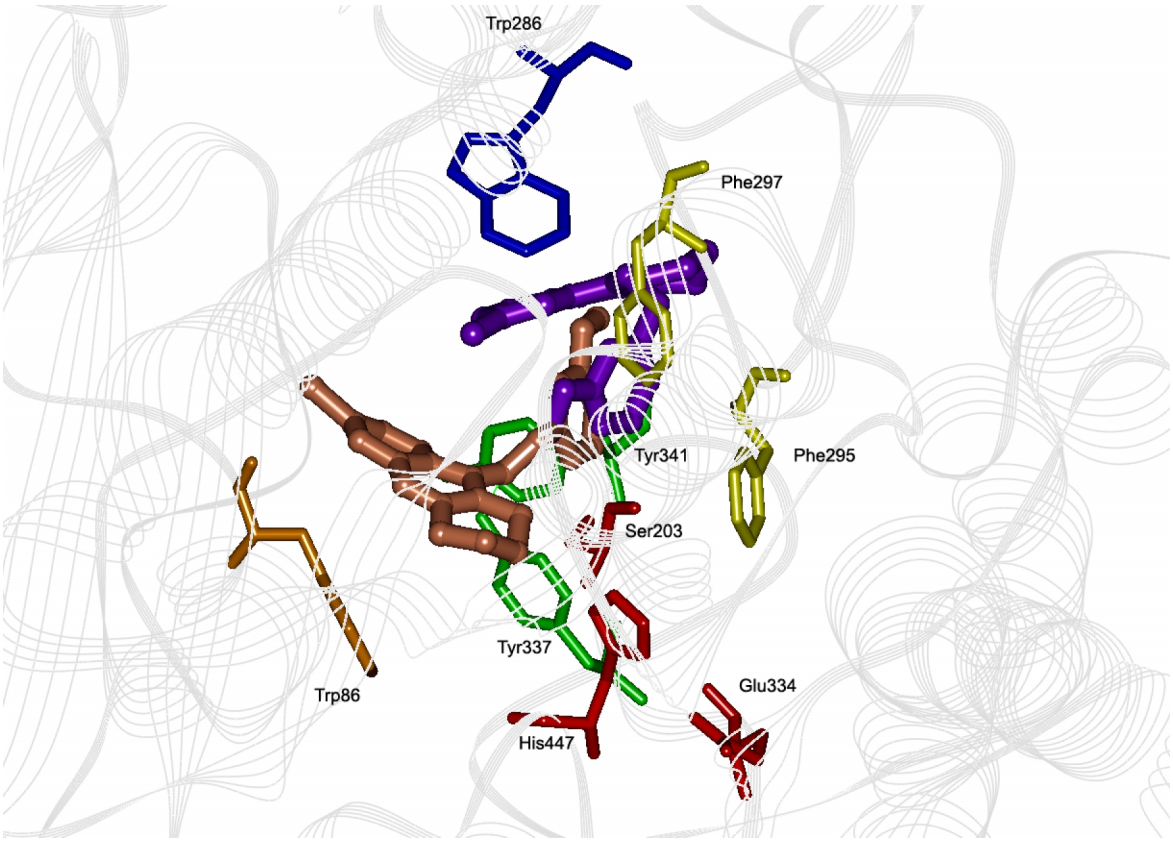

Figure 33: Docking of 6-chloro-*N*-(3-methoxybenzyl)-1,2,3,4-tetrahydroacridin-9-amine (**11c**, salmon, ball and stick) and 7-chloro-*N*-(3-methoxybenzyl)-1,2,3,4-tetrahydroacridin-9-amine (**12c**, purple, ball and stick) in the active site of *h*AChE. Green lines represent hydrogen bonding (distance < 3.5 Å). Hydrogen atoms are not shown for clarity. *Red*: Catalytic triad; *Orange*: Cationic site; *Yellow*: Acyl pocket; *Green*: Stabilizing residues; *Blue*: PAS (AChE)

The binding mode of **11c** in *h*AChE (PDB: 1B41) (Fig. **33**) indicated that the molecule was able to span all the way from the active site gorge to the PAS. It can also be seen that the THA template is situated in the active site while the C-9 methoxy-benzylamine group is directed toward the PAS. The THA template is situated atop Trp86; however it did not lay parallel to the residue, instead taking on an approximate 50º angle. Additionally, the THA template and C-6 chloro substituent form strong van der Waals contact with the Trp86 backbone (distance ≈ 3.8 Å). This C-6 chloro group is pointed opposite to the catalytic triad residues with the aliphatic ring of the THA base forming strong hydrophobic interactions with the catalytic Ser203, (distance ≈ 3.6 Å), and His447 (distance ≈ 3.4 Å). Moving toward the C -9 secondary amine, we

see the amine forming hydrogen bonds with the aromatic residue, Tyr337 (distance ≈ 2.7 Å). The C-9 group is oriented such that the benzyl ring is rotated perpendicularly to that of the THA base. This benzyl ring forms hydrophobic interactions with Phe297, a key residue in the acyl pocket (distance ≈ 3.7 Å). In addition, the 3-OMe substituent forms hydrophobic interactions with a key residue of the PAS, Trp286 (distance ≈ 3.2 Å). Overall, the molecule is in a non-planar conformation, and is situated such that its THA base is located above Trp86 and spans the length of the active site to the PAS. These observations account for its potent AChE inhibition (IC_{50} = 0.61 μM)

Alternatively the spatial orientation of the 7-chloro isomer, **12c**, significantly differs from **11c**. The THA base of **12c** points toward the entrance of AChE with the C-9 group pointing toward the active site. The molecule is also non-planar with the C-9 group slightly bent laterally toward the C-7 chloro-substituted aromatic ring of THA. The molecule is almost entirely PAS localized forming strong hydrophobic interactions between the C-9 amine and Tyr341 (distance ≈ 3.6 Å). The C-9 3-methoxy-benzyl group forms strong hydrophobic interactions with the acyl pocket being ~ 3.3 Å away from Phe297. The C-9 group points toward the active site; however, it is ~10 Å away from the catalytic triad.

The observation that **12c** is able to block the entrance into AChE, while forming hydrophobic interactions with several key residues demonstrates why it has a low μM IC_{50} toward AChE (1.89 μM) (Fig. 33). However, it is apparent that the hydrogen bonding, hydrophobic interactions, and blocking of key residues in the active and catalytic site make **11c** a more potent AChE inhibitor (IC_{50} = 0.61 μM), and thus a simple isomeric change from C-6 to C-7 chlorination can have a significant impact in receptor-ligand binding interactions, which affects AChE inhibition.

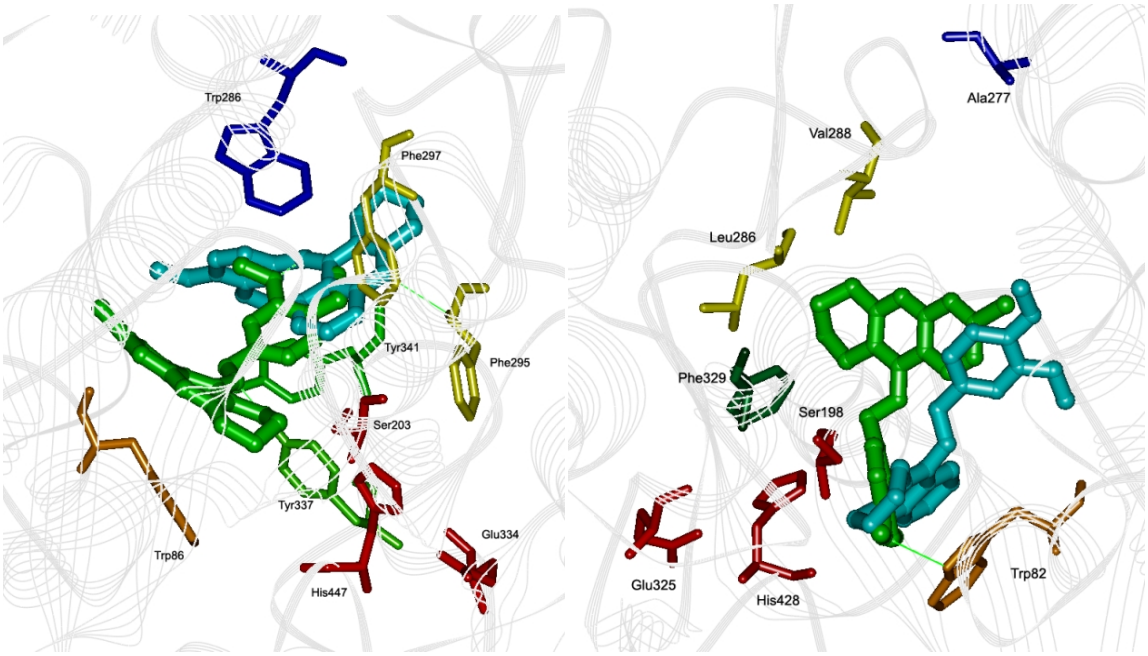

Figure 34: Docking of *N*-(3,4-dimethoxybenzyl)-1,2,3,4-tetrahydroacridin-9-amine (**10d**, light blue, ball and stick) and 6-chloro-*N*-(3,4-dimethoxybenzyl)-1,2,3,4-tetrahydroacridin-9-amine (**11e**, green, ball and stick) in the active site of *h*AChE (left) and *h*BuChE (right). Green lines represent hydrogen bonding (distance < 3.5 Å). Hydrogen atoms are not shown for clarity. *Red*: Catalytic triad; *Orange*: Cationic site; *Yellow*: Acyl pocket; *Green*: Stabilizing residues; *Blue*: PAS (AChE) and PAS analogue (BuChE)

The binding mode of **10d** and **11e** in *h*AChE (PDB: 1B41) (Fig. 34) was investigated to determine the differences in the receptor-ligand interactions which illustrate **11e**'s superior potency (IC_{50} = 0.85 μM) over **10d** (IC_{50} = 2.23 μM) toward AChE. From Figure 34, it can be seen that **10d** is entirely PAS localized with the THA base pointing toward the acyl pocket ~ 3.4 Å away from Phe295, forming hydrogen bonds with the backbone of Phe295 and THA nitrogen. The C-9 group is rotated such that it is perpendicular to the THA base and it protrudes from the enzyme. The C-9 amine also forms van der Waals contact with the Trp286 in the PAS (distance ≈ 4.5 Å), and the stabilizing region with Tyr341 (distance ≈ 4.3 Å) as it is situated between these two residues. The C-9 group's 3-methoxy substituent is also directed toward stabilizing residue Tyr341 (distance ≈ 5.2 Å).

Alternatively, the receptor-ligand interactions between AChE and **11e** show that the compound is situated primarily in the active site gorge. The THA base sits deep into the gorge as

it forms hydrogen bonds between its nitrogen and the backbone of the cationic site residue, Trp86 (distance ≈ 3.5 Å). The molecule is not planar and takes on a "C"-shape. The C-6 chloro group is pointed away from the catalytic site with the aliphatic ring of THA pointed directly toward the catalytic triad. This ring forms polar interactions with Ser203 and His447, (distance ≈ 4.5 Å and 4.0 Å, respectively). The C-9 amine is anchored into the active site by forming hydrogen bonds with Tyr337 (distance ≈ 1.9 Å). Moving toward the C-9 group, we see that it folds slightly inward and lays against Tyr341 ~3.7 Å away. The OMe substituents are directed opposite to the acyl pocket and are located between Tyr341 and Trp286. Strong hydrophobic interactions are formed between the OMe and Trp286 (distance ≈ 4.2 Å).

Furthermore, **11e** spans the length of the active site all the way to the PAS, unlike **10d**. It is anchored by hydrogen bonds and hydrophobic interactions with residues in the cationic site and catalytic triad, thus affording superior AChE inhibition.

As discussed previously in relation to Figure 34, **10d** acts to inhibit *h*BuChE (IC_{50} = 0.024 μM) by completely blocking off Trp82 in the active site from stabilizing incoming substrates through hydrophobic interactions. Its tricyclic THA rings, the largest portion of the molecule, sits deep in the active site. Alternatively, **11e** (BuChE IC_{50} = 1.4 μM) has a significantly different binding mode where its C-9 group is directed into the active site and its THA base directed toward the enzyme entrance. The aliphatic ring is directed into the acyl pocket ~3.4 Å from Leu286 and ~4.8 Å from Val288. The C-9 group extends toward the catalytic site where van der Waals occur between His438 and the 3-OMe substituent interacting with the backbone of His438 (distance ≈ 3.6 Å). Finally the 4-OMe substituent forms a hydrogen bond with Trp82 (distance ≈ 2.8 Å).

Our studies indicate the need for the THA moiety to be within the active site in order to afford superior BuChE inhibition. The presence of a chlorine group at the C-6 position forces the molecule to flip along its horizontal axis with the C-9 group binding within the active site. Although the hydrogen bonding and hydrophobic interactions corroborates **11e**'s μM IC_{50} for BuChE, the lack of a chlorine in **10d** allows the molecule to sit deeper into the active site and afford nM IC_{50} values.

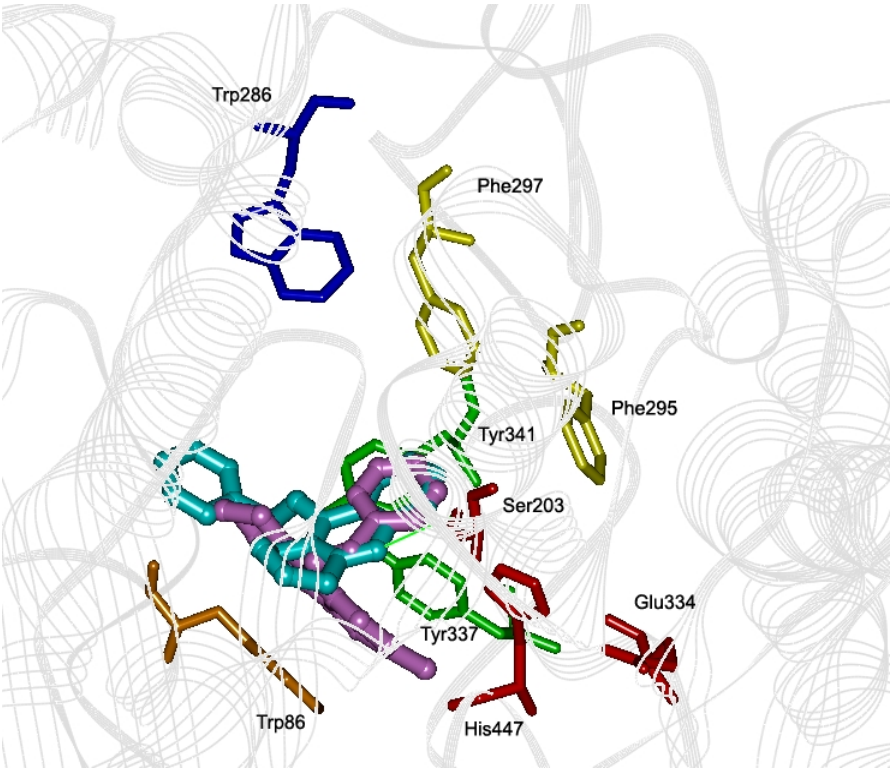

Figure 35: Docking of *N*-(pyridin-2-ylmethyl)-1,2,3,4-tetrahydroacridin-9-amine (**13a**, light blue, ball and stick) and 6-chloro-*N*-(pyridin-2-ylmethyl)-1,2,3,4-tetrahydroacridin-9-amine (**13c**, purple, ball and stick) in the active site of *h*AChE (left) and *h*BuChE (right). Green lines represent hydrogen bonding (distance < 3.5 Å). Hydrogen atoms are not shown for clarity. *Red*: Catalytic triad; *Orange*: Cationic site; *Yellow*: Acyl pocket; *Green*: Stabilizing residues; *Blue*: PAS (AChE) and PAS analogue (BuChE)

The binding mode of **13a** (IC_{50} = 6.65 μM) and **13c** (IC_{50} = 0.095 μM) in *h*AChE (PDB: 1B41) (Fig. **35**) illustrates the differences that occur when a chlorine group is added to a non-chloro picolylamine series derivative. **13a** is in an almost planar conformation with its THA

group pointed toward the catalytic triad; specifically perpendicular to a virtual bridge between His447 and Ser203. The THA base forms hydrogen bonds with the catalytic Ser203 (distance ≈ 3.5 Å), and strong van der Waals interactions with the imidazole nitrogen of His447 (distance ≈ 4.4 Å). The fused benzene ring of the THA base is pointing toward the acyl pocket (distance ≈ 5.8 Å) thus forming van der Waals interactions, whereas the cyclohexyl ring is leaning against Trp86 ~4.6 Å away. The C-9 group is parallel to the cationic pocket ~5 Å away from Trp86 with the picolyl nitrogen forming strong van der Waals interactions with the backbone of Trp86 (distance ≈ 4 Å). Overall the compound is situated in the active site maintaining a planar conformation where it is able to block key residues in the acyl pocket and cationic site.

The presence of a chlorine group at the C-6 position in **13c** does not conform to a planar structure with its THA base in the active site situated atop of Trp86 (distance ≈ 3.5 Å). The THA nitrogen forms strong van der Waals interactions with the Trp86 indole nitrogen (distance ≈ 3.8 Å), with the chlorine group of the THA base pointing toward the catalytic triad ~4.0 Å away from the backbone of His447. The same THA nitrogen also forms hydrogen bonds with key stabilizing residue Trp337 ~2.8 Å away. Moving away from the THA base, the C-9 amine also undergoes strong hydrophobic interactions with Trp86 (distance ≈ 4.0 Å). The C-9 picolyl group is rotated such that the compound is in a "C"-shape conformation with the picolyl group pointing toward the acyl pocket and its nitrogen pointing toward the PAS.

Ultimately, the hydrogen bonding and hydrophobic interactions of **13a** attributes to its weak μM IC_{50} (6.65 μM). However, **13c**'s "C"-shape conformation and localization in the active site allows it to maintain strong hydrogen bonding and hydrophobic interactions in the active site, unlike **13a**, attributing to its far superior binding to AChE (IC_{50} = 0.095 μM).

CHAPTER V

Conclusion and Future Studies

5.1 Conclusion

Over the course of this research project, a compound library of 20 THA-based derivatives were designed, synthesized via 3-4 step reactions, and biologically tested against AChE, BuChE, ROS, and metal chelation.

Compound design was established through review of past literature discussing the most optimal functional groups to create a multi-target compound followed by computational modelling studies to further assess compound potential. Chemical library development utilized a wide range of chemical syntheses with yields ranging between 12 – 82%. Biological evaluations were accomplished with previously developed protocols optimized for the purpose of this project. Computational modelling was re-examined after biological profiles were established on SAR data to substantiate generated results with their enzyme binding patterns. A summary of drug properties are outlined below:

Molecular Weights (MW): 288.38 - 382.88 Da

Molecular Volume (MV): 201.00 **-** 260.33 $Å^3$

Partition Coefficient (ClogP): 4.02 – 6.33

AChE Inhibition (IC_{50}): 0.095– 7.69 μM

BuChE Inhibition (IC_{50}): 0.024 – >25 μM

Antioxidant Capacity (% Inhibition): 5.9 – 12.3%

Chelation Capacity (% chelation): 9.4 – 20.2%

Neuroblastoma Cell Viability (at 25 μM and 50 μM): 1.7 – 100%

When examining the ChE activity profiles of the 20 C-9 substituted THA derivatives, all derivatives but one (19 total) demonstrated dual-ChE inhibition (Table 1 and 2). Many compounds showed significant AChE inhibition with values as low as 0.095 – 0.85 μM (**11c – e, 13c – d**), which are more potent than the marketed agent galantamine (AChE IC_{50}: 3.20 μM) and comparable to tacrine (AChE IC_{50}: 0.215 μM). These compounds fell into the group of C-6 chlorinated derivatives. The most potent compound being **13c** (6-chloro-*N*-(pyridin-2-ylmethyl)-1,2,3,4-tetrahydroacridin-9-amine**;** AChE IC_{50}: 0.095 μM) with AChE inhibition greater than that of tacrine and galantamine, but not as potent as donepezil (AChE IC_{50}: 0.032 μM). The non-chlorinated series proved to show exceptional BuChE inhibition (**10b – d, 13a**; BuChE IC_{50}: 0.024 – 0.089 μM), with **10d** (*N*-(3,4-dimethoxybenzyl)-1,2,3,4-tetrahydroacridin-9-amine**;** BuChE IC_{50}: 0.024 μM) being the most potent. It demonstrates superior BuChE inhibition compared to that of donepezil (BuChE IC_{50}: 3.2 μM), galantamine (BuChE IC_{50}: 13.2 μM), and tacrine (BuChE IC_{50}: 0.06 μM).

In order to establish a multi-target candidate, all compounds were screened for their antioxidant properties. With antioxidant capacity ranging between 5.9 – 12.3% DPPH scavenging, as compared to curcumin (68.8%) and trolox (91.5%), the antioxidant profiles of test compounds appear weak to negligible. Ultimately, it was concluded that lack of a hydroxy (OH) group attached to the C-9 functionality is the primary reason for the weak antioxidant findings. Introduction of a phenolic side chain would potentially afford significantly increased antioxidant capacity.

Finally, select compounds (**13a – f**) were assessed for proof-of-concept to chelate metal ions, specifically iron. The picolylamine-substitute series of compounds showed chelation capacities ranging between 9.4 – 20.2%, with **13e** (7-chloro-*N*-(pyridin-2-ylmethyl)-1,2,3,4-

tetrahydroacridin-9-amine) being the most potent of the series (20.2%), showcasing a third of the chelation capacity of reference compounds clioquinol (63.5%) and desferoxamine (67.1%). Although it was able to chelate, it was relatively weak potentially due to a non-rigid chelating center and varying bond angles between the picolylamine nitrogen and the C-9 amine.

SH-SY5Y neuroblastoma cell viability was assessed in the presence of test compounds and had significant ranges between 1.7 – 100% viability. Differences in cell viability were the result of varying combinations between lipophilicity, bioisosterism, and isomerism.

The acquired SAR for the tacrine based derivates strongly supports their use as ChEI for both AChE and BuChE.

5.2 Future Studies

With our current SAR and biological profiles, future studies pertaining to this research include further development of THA-based derivatives with C-9 catechol- and guaiacol substituted benzylamines to improve the antioxidant profile and metal chelation properties. As previously discussed, the possible loss of a chelation center accounts for the weak chelating ability of the 2-picolyl class of compounds would lead us to explore pyrimidine groups. Additionally a viable option in order to improve chelation capacity is to remove the methylene (-CH_2) at C-9 to prevent bond rotation. Another alternative is to convert the fused cyclohexyl ring of THA into a piperazine (2 nitrogens on a non-aromatic ring) which would also create a chelation center with favourable bond angles.

Finally, replacing the C-9 2-pyridinyl ring with a thiophene or furan ring will allow us to explore metal chelation and antioxidant capacity with sulphur and oxygen as opposed to the picolyl nitrogen and 5-membered versus 6-membered rings (Fig. 36).

Expanding the SAR of lead compounds would include exploring other pathological parameters of AD such as Aβ aggregation inhibition, inflammation, as well as neurofibrillary tangle inhibition. The developed test compounds demonstrate *in silico* that they may be of benefit in the inhibition of AChE-promoted Aβ aggregation whereby test compounds that contain a 3,4-dimethoxybenzyl pharmacophore may be PAS localized (Fig. 32 and 33). As mentioned, the PAS is a key region where Aβ peptides can anchor and form senile plaques promoting AD pathology. It is of therapeutic benefit to explore PAS-blockers to inhibit the generation of PAS-directed Aβ aggregation.

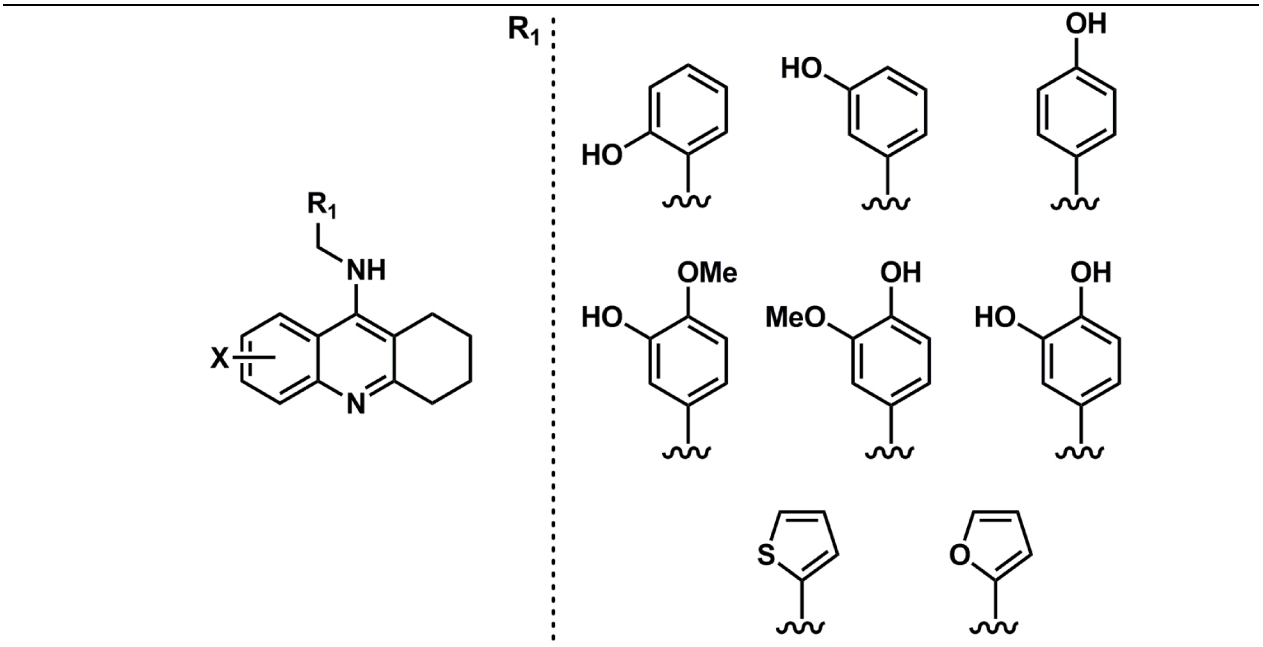

Figure 36: Potential drug candidates with antioxidant and metal chelating capacity

CHAPTER VI

Experimental

6.1 Computational Chemistry

This project utilized the advanced structure-based drug design software, Discovery Studio Client, Accelrys Inc. to investigate compound-enzyme interaction using X-ray crystal structures for both ChEs obtained from the RCSB Protein Data Bank (PDB: 1B41 (*h*AChE), 1POI (*h*BuChE). The *Build Fragment* tool was utilized to construct ligand molecules and energy minimized for 1000 iterations reaching a convergence of 0.01 kcal/mol Å. *Libdock* command was used for docking experiments in the receptor-ligand interactions protocol of Discovery Studio and the energy-minimized ligands after defining a 12-15 Å sphere radius within the enzyme. Docking experiments utilized the Chemistry at HARvard Macromolecular Mechanics (CHARMM) force field. Ligand-enzyme assembly was then subjected to a molecular dynamics (MD) simulation using *Simulation* protocol at a constant temperature of 300 K with a 100 step equilibration for over 1000 iterations and a time step of 1 fs using a distance dependent dielectric constant 4*r*. The optimal binding orientation of the ligand-enzyme assembly obtained after docking was further minimized for 1000 iterations using the conjugate gradient method until a convergence of 0.001 kcal/mol Å was reached after which *E*intermolecular (kcal/mol) of the ligand−enzyme assembly was evaluated and the distances measured.

6.2 Chemistry

All solvents and chemical reagents were obtained from various sources (Acros Organics®, Sigma Aldrich®, Alfa Aesar®, UW Chemstores) with minimum purities of 95% used as is. The Heidolph Laborta 4000 rotary evaporator was used to evaporate solvent from

synthesized compounds. Melting points were obtained using the Fisher-Johns apparatus. ^{1}H-NMR spectra were obtained and analyzed using the Bruker® Avance 300 MHz series spectrometer with $CDCl_3$ as the solvent. Coupling constants (*J* values) were recorded with the values in hertz (Hz). Abbreviations to dictate multiplicity of NMR chemical shifts include: s – singlet, d – doublet, t – triplet, m – multiplet, br – broad. Mass spectra was obtained from the JEOL HX110 double focusing mass spectrometer. Purification was accomplished using Merck 230-400 mesh silica gel 60. Compound purity was assessed via thin layer chromatography (TLC) on Merck 60F254 selica gel plates using different solvent combinations (EtOAc, DCM, 3:1 EtOAc: MeOH). Spots on TLCs are visualized via UV 254 nm. Purity is confirmed with high pressure liquid chromatography (HPLC) analysis using 0.1 % TFA in water/acetonitrile gradient by UV detectiion at 254 nm using the Zobrax Eclipse XDB-C8 column 4.6 x 150 mm testing 5 μM of compound showing more than 95% purity. If necessary, further purification is accomplished via flash chromatography using the same solvent system (Fig. 18).

6.2.1. General Method to Prepare Aminobenzoic Acid Derivatives (4, 5, and 6)

The benzoic acid derivatives were prepared by two different routes: *Reaction A* and *Reaction b*. *Reaction a* was optimized where tin(II)chloride was used as the reducing agent. However, *Reaction a* provided lower yields of desired aminobenzoic acid derivatives. In this regard, *Reaction b*, which used Pd/C in presence of hydrazine hydrate provided superior yields of up to 80%.

Reaction a: 0.01 mol of (**1**), (**2**), or (**3**) is dissolved in excess ethanol (25 mL) at 0°C under argon conditions (Fig. 12). The reaction mixture was reacted with tin-(II)-chloride dihydrate (0.025 mol) for 60 minutes at room temperature. Ethanol was evaporated under

reduced pressure and the dried product is re-dissolved in as little EtOAc as possible. The EtOAc solution was washed 6X with brine solution (Fig. 13). The EtOAc fraction was then dried with $MgSO_4$ and filtered off. EtOAc is evaporated under reduced pressure to afford the light-yellow solid product (**4, 5,** or **6**) (23 - 27% yield).

Reaction b: 0.01 mol of (**1**) is dissolved in ethanol (25 mL) under argon at 0°C. Pd/C (0.001 mol) was added to the reaction mixture followed by the drop-wise addition of hydrazine hydrate (0.04 mol) (Fig. 14). The reaction mixture was refluxed for 1.5 hours at 80°C, cooled and palladium was filtered off via cotton plug and EtOH was evaporated under reduced pressure. Upon drying, the product, (**4**), was obtained as a slightly yellow/brown solid (80% yield). The analytical data for (**4**), (**5**), and (**6**) are given below.

2-Amino-benzoic acid (4): The product is obtained by reducing (**1**) with hydrazine hydrate and Pd/C (1.3 g, 80%). mp: 144 -146°C. ^{1}H-NMR (300 MHz, $CDCl_3$): δ 7.90 (d, J = 8.0 Hz, 1H), δ 7.31 - 7.26 (m, 1H), δ 6.67 - 6.63 (m, 2H)

2-Amino-4-chlorobenzoic acid (5): The product is obtained by reducing (**2**) with tin-(II)-chloride (0.39 g, 23%). mp: 205 - 207°C. ^{1}H-NMR (300 MHz, $CDCl_3$): δ 7.80 (d, J = 8.5 Hz, 1H), δ 6.66 (d, J = 2.0 Hz, 1H), δ 6.63 - 6.59 (dd, J = 8.5 Hz, 2.0 Hz, 1H)

2-Amino-5-chlorobenzoic acid (6): The product is obtained by reducing (**3**) with tin-(II)-chloride (0.46 g, 27%). mp: 196 - 198°C. ^{1}H-NMR (300 MHz, $CDCl_3$): δ 7.86 (d, J = 2.5 Hz, 1H), δ 7.25 - 7.22 (m, 1H), δ 6.62 (d, J = 9.0 Hz, 1H)

6.2.2. General method to prepare 6- or 7-substituted-9-chloro-1,2,3,4-tetrahydroacridine derivatives (7, 8, and 9)

Compound (**7, 8,** or **9**) was synthesized by adding (**4, 5,** or **6**) (0.01 mol) and cyclohexanone (0.01 mol) in a completely dry reaction vessel at 0°C (Fig. 17). This was followed by the drop-wise addition of phosphorous oxychloride ($POCl_3$) (0.10 mol) and the solution was allowed to mix for 5 minutes followed by the addition of 3Å molecular sieves. The reaction mixture is refluxed for 2.5 hours at 120°C and then cooled for 20 minutes. The solution is poured onto ice and 80 mL of 0°C water is added. A precipitate was formed and filtered off. The filtrate is then neutralized with sodium carbonate to precipitate out any remaining product. The precipitate was collected and dissolved in dichloromethane (DCM) (100 mL). The solution is then washed five times with equal volume of concentrated sodium bicarbonate solution. The organic layer is collected and dried with $MgSO_4$ and the solvent is evaporated under reduced pressure. The crude product was purified by flash chromatography (solvent: DCM) and the collected fractions were dried under reduced pressure to afford a yellowish solid which was stored at 4ºC (51 - 82% yield). The analytical data for compounds (**7**), (**8**), and (**9**) are given below.

9-Chloro-1,2,3,4-tetrahydroacridine (7): The product was obtained by coupling (**4**) with cyclohexanone in the presence of $POCl_3$ (4.0 g, 51%) mp: 67 - 69°C ^{1}H-NMR (300 MHz, $CDCl_3$): δ 8.15 (d, J = 8.0 Hz 1H), δ 7.96 (d, J = 8.5 Hz, 1H), δ 7.66 (t, J = 7.0 Hz, 1H), δ 7.61 (t, J = 7.0 Hz, 1H), δ 3.22 - 3.11 (m, 2H), δ 3.05 - 2.99 (m, 2H)

6,9-Dichloro-1,2,3,4-tetrahydroacridine (8): The product was obtained by coupling (**5**) with cyclohexanone in the presence of $POCl_3$ (6.0 g, 82%). mp: 83 - 85°C. ^{1}H-NMR (300 MHz,

$CDCl_3$): δ 8.94 (s, 1H), δ 7.99 (s, 1H), δ 7.47 (dd, J = 9 Hz, 2 Hz, 1H), δ 3.11 - 3.09 (m. 2H), δ 3.01 - 2.99 (m, 2H), δ 1.97-1.88 (m, 4H)

7,9-Dichloro-1,2,3,4-tetrahydroacridine (9): The product was obtained by coupling (**6**) with cyclohexanone in the presence of $POCl_3$ (5.5 g, 75%). mp: 79 - 81°C ^{1}H-NMR (300 MHz, $CDCl_3$): δ 8.11 (d, J = 2.0 Hz, 1H), δ 7.88 (d, J = 9.0 Hz, 1H), δ 7.56 (dd, J = 9.0 Hz, 2.0 Hz, 1H), δ 3.08-3.06 (m, 2H), δ 3.00 - 2.87 (m, 2H), δ 1.96 - 1.88 (m, 4H)

6.2.3. General method to prepare 6- or 7-substituted-*N*-benzyl-1,2,3,4-tetrahydroacridine-9-amine derivatives (10a-d, 11a-e, 12a-e, 13a-f)

Coupling the various benzylamine groups to (**7, 8,** or **9**) was done in two ways. i) Firstly, sodium iodide (0.0006 mol) was added to (**7, 8,** or **9**) (0.002 mol), and dissolved as much as possible in excess butanol (5 mL) (Fig. 19). Benzylamine (0.005 mol) was added and the reaction mixture was refluxed at 150ºC for 4.5 hours, cooled, and then immediately dried under reduced pressure. It was re-dissolved in excess DCM and washed three times with concentrated brine solution. The organic layer was dried with $MgSO_4$ and the solvent was evaporated under reduced pressure. The remaining product was purified via flash chromatography (solvent: EtOAc). Some compounds were purified by repetitive flash chromatography (2-3 repeats).

ii) Sodium iodide (0.6 mmol) was added to (**7**), (**8**), or (**9**) (0.002 mol), followed by the addition of benzylamines (0.005 mol) (Fig. 19). Phenol (0.01 mol) was added and the reaction mixture was refluxed at 180ºC for 3 hours. The reaction mixture was allowed to cool to room temperature, dissolved in excess DCM, then washed three times with concentrated brine solution. The organic layer was collected and dried with $MgSO_4$ and the solvent was evaporated under reduced pressure. The remaining product was purified via flash chromatography (solvent:

EtOAc). Some compounds were purified by repetitive flash chromatography (2-3 repeats). The analytical data for compounds **10a-d, 11a-e, 12a-e, 13a-f** are shown below.

6.2.3.1 Analytical Data for Benzylamine and Substituted-Benzylamine Series

***N*-1,2,3,4-tetrahydroacridin-9-amine (10a):** The product was obtained by coupling (**7**) with benzylamine (0.45 g, 45%). mp:111-113 ºC. ^{1}H-NMR (300 MHz, $CDCl_3$): δ 7.90 (t, *J* = 8.0 Hz, 2H), δ 7.49 (t, *J* = 8.0 Hz, 1H), δ 7.35 – 7.25 (m, 6H), δ 4.56 (d, *J* = 6.0 Hz, 2H), δ 4.17 (br s, 1H), δ 3.02 (t, *J* = 6.0 Hz, 2H), δ 2.57 (t, *J* = 6.0 Hz, 2H), δ 1.86 – 1.78 (m, 4H). ESI-MS: 289 $[M+H]^+$

***N*-(2-methoxybenzyl)-1,2,3,4-tetrahydroacridin-9-amine (10b):** The product was obtained by coupling (**7**) with 2-methoxybenzylamine (0.45 g, 40%). mp: semisolid. ^{1}H-NMR (300 MHz, $CDCl_3$): δ 8.47 (d, *J* = 8.5 Hz, 1H), δ (d, *J* = 8.5 Hz, 1H), δ 7.52 (t, *J* = 8.0 Hz, 1H), δ 7.33 - 7.22 (m, 3H), δ 6.89 – 6.78 (m, 2H), δ 6.11 (br s, 1H), δ 4.88 (s, 2H), δ 3.76 (s, 3H), δ 3.18 – 3.08 (m, 2H), δ 2.61 – 2.56 (m, 2H), 1.87 – 1.76 (m, 4H). ESI-MS: 319 $[M+H]^+$

***N*-(3-methoxybenzyl)-1,2,3,4-tetrahydroacridin-9-amine (10c):** The product was obtained by coupling (**7**) with 3-methoxybenzylamine (0.35 g, 32%). mp: semisolid. ^{1}H-NMR (300 MHz, $CDCl_3$): δ 7.90 (t, *J* = 8.0 Hz, 2H), δ 7.52 (t, *J* = 8.0 Hz, 1H), δ 7.35-7.23 (m, 2H), δ 6.92-6.81 (m, 3H), δ 4.56 (d, *J* = 6.0 Hz, 2H), δ 4.21-4.17 (m, 1H), δ 3.75 (s, 3H), δ 3.04 (t, *J* = 6.0 Hz, 2H), δ 2.16 (t, *J* = 6.0 Hz, 2H), δ 1.92-1.81 (m, 4H). ESI-MS: 319 $[M+H]^+$

***N*-(3,4-dimethoxybenzyl)-1,2,3,4-tetrahydroacridin-9-amine (10d):** The product was obtained by coupling (**7**) with 3,4-dimethoxybenzylamine (0.40 g, 41%). mp: semisolid. ^{1}H-NMR (300 MHz, $CDCl_3$): δ 7.94 (d, *J* = 8.5 Hz, 1H), δ 7.90 (d, *J* = 8.5 Hz, 1H), δ 7.52 (t, *J* = 8.0 Hz, 1H), δ 7.30 (t, *J* = 7.5 Hz, 1H), δ 6.81 (q, *J* = 8.0 Hz, 2H), δ 6.76 (s, 1H), δ 4.55 – 4.52 (m, 2H), δ 4.13 (br s, 1H), δ 3.86 (s, 3H), δ 3.78 (s, 3H), δ 3.02 (t, *J* = 6.0 Hz, 2H), δ 2.60 (t, *J* = 5.0 Hz, 2H), δ 1.86 – 1.80 (m, 4H). ESI-MS: 349 $[M+H]^+$

***N*-Benzyl-6-Chloro-1,2,3,4-tetrahydroacridin-9-amine (11a):** The product was obtained by coupling (**8**) with benzylamine (0.40 g, 41%). mp: semisolid. ^{1}H-NMR (300 MHz, $CDCl_3$): δ 8.01 - 7.94 (m, 1H), δ 7.89 (d, *J* = 9.0 Hz, 1H), δ 7.38 – 7.29 (m, 6H), δ 4.63 (s, 2H), δ 4.27 (br s, 1H), δ 3.09 – 3.00 (m, 2H), 2.60 – 2.54 (m, 2H), 1.91 – 1.79 (m, 4H). ESI-MS: 323 $[M+H]^+$

6-Chloro-*N*-(2-methoxybenzyl)-1,2,3,4-tetrahydroacridin-9-amine (11b): The product was obtained by coupling (**8**) with 2-methoxybenzylamine (0.25 g, 25%). mp: semisolid. ^{1}H-NMR (300 MHz, $CDCl_3$): δ 7.91 (d, *J* = 8.0 Hz, 2H), δ 7.27 (s, 1H), δ 7.15 (d, *J* = 7.0 Hz, 1H), δ 6.87 (d, *J* = 7.0 Hz, 2H), δ 5.27 (s, 1H), δ 4.56 (s, 2H), δ 3.80 (s, 3H), δ 3.02 – 3.00 (m, 2H), δ 2.58 – 2.59 (m, 2H), δ 1.85 – 1.82 (m, 4H). ESI-MS: 353 $[M+H]^+$

6-Chloro-*N*-(3-methoxybenzyl)-1,2,3,4-tetrahydroacridin-9-amine (11c): The product was obtained by coupling (**8**) with 3-methoxybenzylamine (0.15 g, 15%). mp: semisolid. ^{1}H-NMR (300 MHz, $CDCl_3$): δ 7.92 (s, 1H), δ 7.87 (d, *J* = 9.0 Hz, 1H), δ 7.30 – 7.26 (m, 2H), δ 6.90 – 6.84 (m, 3H), δ 4.57 (s, 2H), δ 4.19 (br s, 1H), δ 4.19 (br s, 1H), δ 3.77 (s, 3H), δ 3.01 (t, *J* = 6.0 Hz, 2H), δ 2.57 (t, *J* = 6.0 Hz, 2H), δ 1.87 – 1.85 (m, 4H). ESI-MS: 353 $[M+H]^+$

6-Chloro-*N*-(4-methoxybenzyl)-1,2,3,4-tetrahydroacridin-9-amine (11d): The product was obtained by coupling (**8**) with 4-methoxybenzylamine (0.14 g, 14%). mp: semisolid. ^{1}H-NMR (300 MHz, $CDCl_3$): δ 7.95 – 7.89 (m, 2H), δ 7.27 – 7.19 (m, 3H), δ 6.85 (d, *J* = 5 Hz, 2H), δ 4.59 - 4.51 (m, 1H), δ 4.29 (br s, 1H), δ 3.80 (s, 3H), δ 3.10 – 2.99 (m, 2H), δ 2.58 – 2.54 (m 2H), 1.89 – 1.83 (m, 4H). ESI-MS: 353 $[M+H]^+$

6-Chloro-*N*-(3,4-dimethoxybenzyl)-1,2,3,4-tetrahydroacridin-9-amine (11e): The product was obtained by coupling (**8**) with 3,4-dimethoxybenzylamine (0.40 g, 35%) . mp: 131-133 ºC. ^{1}H-NMR (300 MHz, $CDCl_3$): δ 7.90 – 7.87 (m, 2H), δ 7.27 – 7.24 (m, 1H), δ 6.87 – 6.81 (m, 2H), δ 6.75 (s, 1H), δ 4.53 (s, 2H), δ 4.13 (br s, 1H), δ 3.87 (s, 3H), δ 3.79 (s, 3H), δ 3.00 (t, *J* = 6.0 Hz, 2H), δ 2.55 (t, *J* = 5.0 Hz, 2H), δ 1.87 – 1.75 (m, 4H). ESI-MS: 383 $[M+H]^+$

***N*-Benzyl-7-Chloro-1,2,3,4-tetrahydroacridin-9-amine (12a):** The product was obtained by coupling (**9**) with benzylamine (0.35 g, 36%). mp: semisolid. ^{1}H-NMR (300 MHz, $CDCl_3$): δ 8.54 (d, *J* = 9.0 Hz, 1H), δ 8.17 (s, 1H), δ 7.59 (dd, *J* = 9.0 Hz, 2 Hz, 1H), δ 7.44-7.25 (m, 5H), δ 5.91(br s, 1H), δ 5.06 (s, 2H), δ 3.29 (t, *J* = 6.0 Hz, 2H), δ 2.59 (t, *J* = 6 Hz, 2H), δ 1.90-1.87 (m, 4H). ESI-MS: 323 $[M+H]^+$

7-Chloro-*N*-(2-methoxybenzyl)-1,2,3,4-tetrahydroacridin-9-amine (12b): The product was obtained by coupling (**9**) with 2-methoxybenzylamine (0.12 g, 12%). mp: semisolid. ^{1}H-NMR (300 MHz, $CDCl_3$): δ 8.00 (d, *J* = 2.0 Hz, 1H), δ 7.79 (d, *J* = 6.0 Hz, 1H), δ 7.42 (dd, *J* = 9.0 Hz, 2.0 Hz, 1H), δ 7.20 (t, *J* = 7.0 Hz, 1H), δ 7.10 (d, *J* = 5.0 Hz, 1H), δ 6.81 (t, *J* = 5.0 Hz, 2H), δ

4.46 (s, 2H), δ 4.38 (br s, 1H), δ 3.81 (s, 3H), δ 2.97 (t, *J* = 6.0 Hz, 3H), δ 2.58 (t, *J* = 6.0 Hz, 2H), δ 1.85-1.78 (m, 4H). ESI-MS: 353 $[M+H]^+$

7-Chloro-*N*-(3-methoxybenzyl)-1,2,3,4-tetrahydroacridin-9-amine (12c): The product was obtained by coupling (**9**) with 3-methoxybenzylamine (0.17 g, 17%). mp: semisolid. ^{1}H-NMR (300 MHz, $CDCl_3$): δ 7.94 - 7.93 (m, 1H), δ 7.81 (d, *J* = 9.0 Hz, 1H), δ 7.43 (dd, *J* = 9.0 Hz, 2.0 Hz, 1H), δ 7.27-7.22 (m, 1H), δ 6.88-6.81 (m, 3H), 4.51 (d, *J* = 6.0 Hz, 2H), δ 4.11 (br s, 1H), δ 3,74 (s, 3H), δ 2.99 (t, *J* = 6.0 Hz, 2H), δ 2.55 (t, *J* = 6.0 Hz, 2H), δ 1.84-1.81 (m, 4H). ESI-MS: 353 $[M+H]^+$

7-Chloro-*N*-(4-methoxybenzyl)-1,2,3,4-tetrahydroacridin-9-amine (12d): The product was obtained by coupling (**9**) with 4-methoxybenzylamine (0.20 g, 20%). mp: semisolid. ^{1}H-NMR (300 MHz, $CDCl_3$): δ 7.96 (s, 1H), δ 7.83 (d, *J* = 9.0 Hz, 1H), δ 7.50-7.46 (m, 1H), δ 7.19 (d, *J* = 8.0 Hz, 2H), δ 6.86 (d, *J* = 8.0 Hz, 2H), δ 4.51 (s, 2H), δ 4.03 (br s, 1H), δ 3.80 (s, 3H), δ 3.00 (t, *J* = 6.0 Hz, 2H), δ 2.54 (t, *J* = 6.0 Hz, 2H), 1.85-1.82 (m, 4H). ESI-MS: 353 $[M+H]^+$

7-Chloro-*N*-(3,4-dimethoxybenzyl)-1,2,3,4-tetrahydroacridin-9-amine (12e): The product was obtained by coupling (**9**) with 3,4-dimethoxybenzylamine (0.23 g, 20%). mp: 113-115 ºC. ^{1}H-NMR (300 MHz, $CDCl_3$): δ 7.96 (d, *J* = 2.0 Hz, 1H), δ 7.82 (d, *J* = 9.0 Hz, 1H), δ 7.46 (dd, *J* = 9.0 Hz, 2 Hz, 1H), δ 6.81 - 6.87 (m, 2H), δ 6.75 (s, 1H), δ 4.50 (d, *J* = 3.5 Hz, 2H), δ 4.09 (br s, 1H), δ 3.87 (s, 3H), δ 3.80 (s, 3H), δ 2.99 (t, *J* = 6.0 Hz, 2H), δ 2.56 (t, *J* = 6.0 Hz, 2H), δ 1.87-1.83 (m, 4H). ESI-MS: 383 $[M+H]^+$

6.2.3.2 Analytical Data for *N*-(pyridinylmethyl)-1,2,3,4-tetrahydroacridin-9-amine Derivatives

***N*-(pyridin-2-ylmethyl)-1,2,3,4-tetrahydroacridin-9-amine (13a):** The product was obtained by coupling (**7**) with 2-picolylamine (0.35 g, 35%). mp: 103-105 ºC ^{1}H-NMR (300 MHz, $CDCl_3$): δ 8.64 (d, *J* = 4.5 Hz, 1H), δ 8.09 (d, *J* = 8.0 Hz, 1H), δ 7.89 (d, *J* = 8.0 Hz, 1H), δ 7.60 (td, *J* = 8.0 Hz, 2.0 Hz, 1H), δ 7.51 (td, *J* = 8.0 Hz, 1.0 Hz, 1H), δ 7.33 (t, *J* = 7.5 Hz, 1H), δ 7.17 – 7.21 (m, 2H), 5.86 (br s, 1H), δ 4.76 (d, *J* = 5.0 Hz, 2H), δ 3.00 – 3.10 (m, 2H), δ 2.90 – 2.80 (m, 2H), δ 1.92 – 1.87 (m, 4H). ESI-MS: 290 $[M+H]^+$

***N*-(pyridin-3-ylmethyl)-1,2,3,4-tetrahydroacridin-9-amine (13b):** The product was obtained by coupling (**7**) with 3-picolylamine (0.40 g, 40%). mp: semisolid. ^{1}H-NMR (300 MHz, $CDCl_3$): δ 8.60 (d, *J* = 2.0 Hz, 1H), δ 8.53 (dd, *J* = 5.0 Hz, 1.5 Hz, 1H), δ 7.89 (dd, *J* = 8.0 Hz, 6.0 Hz, 2H), δ 7.62 – 7.53 (m, 2H), δ 7.32 (t, *J* = 7.0 Hz, 1H), δ 7.27 – 7.23 (m, 1H), δ 4.57 (d, *J* = 7.0 Hz, 2H), δ 4.07 – 4.11 (m, 1H), δ 3.03 (t, *J* = 6.0 Hz, 2H), δ 2.61 (t, *J* = 6.0 Hz, 2H), δ 1.89 – 1.83 (m, 4H). ESI-MS: 290 $[M+H]^+$

6-Chloro-*N*-(pyridin-2-ylmethyl)-1,2,3,4-tetrahydroacridin-9-amine (13c): The product was obtained by coupling (**8**) with 2-picolylamine (0.35 g, 36%). mp: 117 – 119 ºC. ^{1}H-NMR (300 MHz, $CDCl_3$): δ 8.65 (d, *J* = 5.0 Hz, 1H), δ 8.08 (d, *J* = 6.0 Hz, 1H), δ 7.99 (s, 1H), δ 7.66 (t, *J* = 3.0 Hz, 1H), δ 7.29 (dd, *J* = 9.0 Hz, 2.0 Hz, 1H), δ 7.28-7.23 (m, 2H), δ 6.43 (br s, 1H), δ 4.86 (d, *J* = 5.0 Hz, 2H), δ 3.08-3.05 (m, 2H), δ 2.82 - 2.79 (m, 2H), δ 1.92-1.90 (m, 4H). ESI-MS: 324 $[M+H]^+$

6-Chloro-*N*-(pyridin-3-ylmethyl)-1,2,3,4-tetrahydroacridin-9-amine (13d): The product was obtained by coupling (**8**) with 3-picolylamine (0.25 g, 26%). mp: 87 – 89 ºC ^{1}H-NMR (300

MHz, $CDCl_3$): δ 8.59 (d, *J* = 2.0 Hz, 1H), δ 8.55 (dd, *J* = 5.0 Hz, 1 Hz, 1H), δ 7.93 (d, *J* = 2.0 Hz, 1H), δ 7.84 (d, *J* = 9.0 Hz, 1H), δ 7.58 (d, *J* = 8.0 Hz, 1H), δ 7.26 (dd, *J* = 9.0 Hz, 2 Hz, 2H), δ 4.60 (d, *J* = 6.5 Hz, 2H), δ 4.25 (br s, 1H), δ 3.01 (t, *J* = 6.0 Hz, 2H), δ 2.57 (t, *J* = 6.0 Hz, 2H), δ 1.91 – 1.89 (m, 4H). ESI-MS: 324 $[M+H]^+$

7-Chloro-*N*-(pyridin-2-ylmethyl)-1,2,3,4-tetrahydroacridin-9-amine (13e): The product was obtained by coupling (**9**) with 2-picolylamine (0.45 g, 47%). mp: semisolid. ^{1}H-NMR (300 MHz, $CDCl_3$): δ 8.66 – 8.63 (m, 1H), δ 8.10 (d, *J* = 2 Hz, 1H), δ 7.83 (d, *J* = 7.5 Hz, 1H), δ 7.68 – 7.62 (m, 1H), δ 7.46 (dd, *J* = 9.0 Hz, 2 Hz, 1H), δ 7.24 - 7.19 (m, 2H), δ 6.05 (br s, 1H), δ 4.79 – 4.73 (m, 2H), δ 3.10 – 2.99 (m, 2H), δ 2.85 – 2.75 (m, 2H), δ 1.93 – 1.81 (m, 4H). ESI-MS: 324 $[M+H]^+$

7-Chloro-*N*-(pyridin-3-ylmethyl)-1,2,3,4-tetrahydroacridin-9-amine (13f): The product was obtained by coupling (**9**) with 3-picolylamine (0.26 g, 27%). mp: 126 – 128 ºC ^{1}H-NMR (300 MHz, $CDCl_3$): δ 8.59 (d, *J* = 2.0 Hz, 1 H), δ 8.55 (dd, *J* = 5.0 Hz, 1.5 Hz, 1H), δ 7.90 – 7.93 (m, 2 H), δ 7.59 (d, *J* = 8.0 Hz, 1H), δ 7.48 (dd, *J* = 9.0 Hz, 2.0 Hz, 1H), δ 7.25 (dd, *J* = 8.0 Hz, 5.0 Hz, 2H), δ 4.60 (d, *J* = 6.5 Hz, 2H), δ 4.24 (br s, 1H), δ 3.03 (t, *J* = 6.0 Hz, 2H), δ 2.57 (t, *J* = 6.0 Hz, 2H), δ 1.87 – 1.84 (m, 4H). ESI-MS: 324 $[M+H]^+$

6.3 Biological Evaluation

6.3.1 Cholinesterase Inhibition Evaluation

Test compounds were evaluated for their ability to inhibit *h*AChE and *h*BuChE using a 96-well plate (Fig. 37). Reference compounds tacrine, galantamine, and donepezil were used for comparison. Test compound solutions were solubilized in minimum amount of DMSO (1% v/v) and a wide range of concentrations were used (0.025 – 25 μM) to determine the IC_{50} values.

Each well, with the exception of blanks, and controls, contained 160 μL of DTNB, 50 μL *h*AChE or *h*BuChE solution, and 10 μL of test compound. Blank wells contained 160 μl DTNB, 50 μL buffer A, and 10 μL DMSO. 100% ChE activity (100% activity) contained 160 μl DTNB, 50 μL *h*AChE/*h*BuChE, 8 μl buffer A, and 2 μL DMSO. Aluminum foil was used to cover the 96-well plate from light exposure due to DTNB light-sensitivity. A 5 minute incubation period at room temperature was followed, and 30 μL of substrate (acetylthiocholine iodide 15 mM or butyrylthiocholine iodide 15 mM) (final volume 250 μL) was then added. The absorbance values were taken every minute for 5 minutes at 410 nm. The average absorbance value from all 6 readings (t = 0, 1, 2, 3, 4, 5 min) were subtracted from average absorbance values from the 100% activity controls, then divided by the average absorbance of 100% activity control. The percent inhibition was obtained as per the equation below. The IC_{50} values for each compound were calculated by plotting their percent inhibition values against their respective concentrations on a logarithmic scale. A line of best fit was determined and the IC_{50} is calculated from the equation.

Percent inhibition =

(100%-activity absorbance – test compound absorbance)/(100%-activity absorbance) x 100

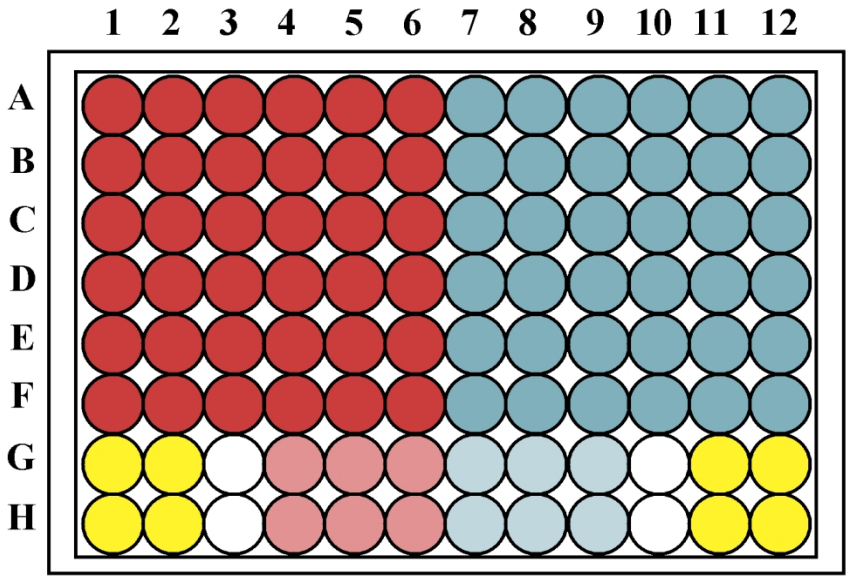

Figure 37: General set-up of 96-well plate. *Red*: test compounds with *h*AChE; *Pink*: 100% *h*AChE activity; *Dark Blue*: test compounds with *h*BuChE; *Light Blue*: 100% *h*BuChE activity; *Yellow*: blanks without ChE or test compound; *White*: empty wells

6.3.1.1 Solutions and Substrates

Buffer A was prepared by dissolving 3.029 g of Trizma base (Sigma), 2.922 g of NaCl and 2.033 g of $MgCl_2 \bullet 6H_2O$ in 450 mL of UPW. 1M HCl was added to the solution until pH 8.0, and finally the solution was filled up to 500 mL with ultra pure water (UPW).

Buffer B was prepared by dissolving 3.029 g of Trizma base (Sigma) in UPW followed by 0.50 g of BSA and 20 mL of UPW. Finally, 0.086 mL of 1M HCl was added with the final solution pH at 8.0. Then the volume was made up to 50 mL with UPW.

Acetylcholinesterase solution (0.22 units/mL) was prepared by dissolving the supplied amount of *h*AChE (425.95 units/mg) in 9.4 mL of buffer B. 0.5 mL of the aforementioned solution was added to an additional 0.5 mL of buffer B; 0.011 mL of this solution was added to 5.31 mL of buffer B yielding a final concentration of 0.22 units/mL.

Butyrylcholinesterase solution (0.12 units/mL) was prepared by dissolving the supplied amount of *h*BuChE (221 units/mg) in 9.0 mL of buffer B. 0.5 mL of the aforementioned solution was added to an additional 0.5 mL of buffer B; 0.010 mL of this solution was added to 9.198 mL of buffer B yielding a final concentration of 0.12 units/mL.

6.3.2 Antioxidant Capacity Evaluation

In a 96-well plate, 50 µL of test compound was first added followed by 200 µL of DPPH ($\mathbf{A_{Test}}$; final volume 250 µL). Blank controls are comprised of 50 µL test compound solution and 200 µL MeOH ($\mathbf{A_{Test\ Blank}}$; final volume 250 µL) and carried out in duplicate for each test compound concentration. DPPH control wells include 50 µL MeOH and 200 µL DPPH solution ($\mathbf{A_{DPPH}}$; final volume 250 µL). Negative controls contain 250 µL of MeOH, and empty well controls are left without any solutions (final volume 250 µL). Reference compound trolox or curcumin were included. The plate was incubated at room temperature while shaking for 30 minutes. Absorbance values were taken at time 0 and 30 minutes (517 nm). The percent inhibition was calculated as per the equation below:

$$\textbf{Percent inhibition} = [(A_{DPPH} - (A_{Test} - A_{Test\ Blank}))/A_{DPPH}] \times 100$$

6.3.2.1 Preparation of DPPH solution

DPPH solution was prepared by dissolving 5 µmol of DPPH in 40 mL of MeOH (125 µM). Dilute the solution to 62.5 µM with MeOH to finalize the DPPH solution used in test compound evaluation. The solution was stored to protect it from light exposure.

6.3.3 Chelation Capacity Evaluation

Iron chelation capacity: Stock solutions of test compounds were prepared in tris buffer (pH 7.4; 100 mM). Test compound solution (95 µL: final concentration 50 µM) was added to $FeSO_4 \cdot 7H_2O$ (10 µL: final concentration 40 µM) followed by ferrozine (95 µL: final concentration 100 µM) ($\mathbf{A_{Test}}$; final volume 200 µL). The absorbance value of the mixture was recorded at 562 nm after incubating at room temperature for 20 minutes. Test compound blanks were prepared with test compound solution (95 µL) added to $FeSO_4 \cdot 7H_2O$ (10 µL: final concentration 40 µM), and 95 µL UPW instead of ferrozine. Results were compared with reference agents clioquinol and desferoxamine. The percentage of iron bound was then determined. The percent of chelation were calculated following the equation:[69]

Chelating ability % = [1 – absorbance sample/absorbance control] x 100

6.3.3.1 Preparation of Reagent and Buffer solutions

Tris buffer was prepared by dissolving 3.0 g (0.025 mol) tris(hydroxymethyl)aminomethane) in 200 mL of UPW in a volumetric flask. The pH was adjusted to 7.4 through drop-wise addition of HCl solution (1M). The volume was made up to 250 mL

Ferrozine stock solution (10 mM) was prepared by weighing 4.92 mg of 3-(2-pyridyl)-5,6-diphenyl-1,2,4-triazine-*p*,*p'*-disulfonic acid monosodium salt hydrate (ferrozine) in 1 mL tris buffer solution. This solution was diluted to 210 µM using tris buffer.

Iron stock solution (10 mM) was prepared by dissolving 2.78 mg iron(II)sulphate heptahydrate in 1 mL MeOH. This solution was diluted to to 800 µM and used to evaluate chelation.

6.3.4 Evaluation of Cell Viability

Evaluation of cell viability was performed using the SH-SY5Y neuroblastoma cell line via examination of the reduction of 3(4,5 dimethylthiazol-2-yl)-2.5 diphenyltetrazolium bromide (MTT) into a purple formazan via mitochondrial reductase activity. Cells were plated at a density of 4×10^5 cells/mL in growth media consisting of 1:1 DMEM and Ham's F12 (Thermo, Fisher), supplemented with 2.5 mM glutamate and 10% fetal bovine serum at 37ºC in 5% CO_2. Cells were incubated after treated with test compounds, 50 µM and 25 µM, for 24 hours at 37ºC (n = 3). After incubation, each well was treated with MTT solution equal to 10% of the cell culture medium volume followed by an additional 3 hour incubation period at 37ºC in 5% CO_2. Upon incubation completion the generated formazan was solubilized with MTT reagent solution (10% Triton X-100 and 0.1 N HCl in anhydrous isopropanol) in equal volume to the culture medium for each well with readings done at 570 nm with subtraction of background absorbance values.

.

References

1. Goedert M.; Spillantini M.G. A Century of Alzheimer's Disease. *Science* **2006***, 314*, 777-781.
2. Alzheimer's Disease International World Alzheimer Report. London, United Kingdom: King's College; 2010.
3. Samuel W.; Terry R.D.; DeTeresa R.; Butters N.; Masliah E. Clinical correlates of cortical and nucleus basalis pathology in Alzheimer dementia. *Arch. Neurol*. **1994**, *51*, 772–778.
4. Tiraboschi P.; Hansen L.A.; Alford M.; Masliah E.; Thal L.J.; Corey-Bloom J. The decline in synapses and cholinergic activity is asynchronous in Alzheimer's disease. *Neurology*. **2000**, *55*, 1278–1283.
5. Bolea I.; Juárez-Jiménez J.; Delosrios C.; Chioua M.; Pouplana R.; Luque F.J.; Unzeta M.; Marco-Contelles J.; Samadi A. Synthesis, biological evaluation and molecular modeling of donepezil and *N*-[(5-(benzyloxy)-1-methyl-1H-indol-2-yl)methyl]-*N*-methylprop-2-yn-1-amine hybrids, as new multipotent cholinesterase/monoamine oxidase inhibitors for the treatment of Alzheimer's disease. *J. Med. Chem.* **2011**, *54*, 8251–8270
6. Alzheimer's Disease International, World Alzheimer Report 2011, "The benefits of early diagnosis and intervention," by Prof Martin Prince, Dr Renata Bryce and Dr Cleusa Ferri, Institute of Psychiatry, King's College London, Summary, p.4.
7. 2012 Alzheimer's Disease Facts and Figures. *Alzheimer's & Dementia*. **2012**, *8*, 42-43.
8. Talesa V.N. Acetylcholinesterase in Alzheimer's disease. *Mech. Ageing Dev*. **2001**, *122*, 1961–1969.

9. Terry Jr. A.V.; Buccafusco J.J. The cholinergic hypothesis of age and Alzheimer's disease-related cognitive deficits: recent challenges and their implications for novel drug development. *J. Pharmacol. Exper. Therap.* **2003**, *306*, 821-827.
10. Lane R.M.; Potkin S.G.; Enz A. Targeting acetylcholinesterase and butyrylcholinesterase in dementia. *Int. J. Neuropsychopharmacol*. **2006**, *9*, 101-124.
11. Darvesh S.; Lockridge O.; Darvesh K.V.; Martin E. Carbamates with differential mechanism of inhibition toward acetylcholinesterase and butyrylcholinesterase *J. Med. Chem.* **2008**, *51,* 4200–4212.
12. Kryger G.; Giles K.; Velan B.; Harel M.; Toker L.; Kronman C.; Ariel N.; Lazar A.; Shafferman A.; Barak D.; Silman I.; Sussman J.L. Structures of recombinant native and E202Q mutant human acetylcholinesterase complexed with the snake-venom toxin fasciculin-II. *Acta. Cryst*. **2000**, *56*, 1385-1394.
13. Barak D.; Ordentlich A.; Kaplan D.; Kronman C.; Velan B.; Shafferman A. Lessons from functional analysis of AChE covalent and noncovalent inhibitors for design of AD therapeutic agents. *Chem. Biol. Interact*. **2005**, *157-158*, 219-226.
14. Inestrosa N.C.; Dinamarca M.C.; Alvarez A. Amyloid-cholinesterase interactions – implications for Alzheimer's disease. *FEBS* **2008**, *275*, 625-632.
15. Inestrosa N.C.; Alvarez A.; Perez C.A.; Moreno, R. D.; Vincete, M.; Linker, C.; Casanueva, O.I.; Soto, C.; Garrido, J. Acetylcholinesterase accelerates assembly of amyloid-β-peptides into Alzheimer's fibrils: Possible role of the peripheral site of the enzyme. *Neuron* **1996**, *16*, 881-891.
16. Belluti F.; Rampa A.; Piazzi L.; Bisi A.; Gobbi S.; Bartolini M.; Andrisano V.; Cavalli A.; Recanatini M.; Valenti P. Cholinesterase inhibitors: Xanthostigmine derivatives

blocking the acetylcholinesterase-induced β-amyloid aggregation. *J. Med. Chem.* **2005**, *48*, 4444-4456.

17. Mohamed T.; Yeung J.C.K.; Rao P.P.N. Development of 2-substituted *N*-(naphthalene-1-ylmethyl)- and *N*-benzhydryl-pyrimidin-4-amines as dual cholinesterase and Aβ-aggregation inhibitors: Synthesis and biological evaluation. *Bioorg. Med. Chem. Lett.* **2011***, 21*, 5881-5887 .
18. Nicolet Y.; Lockbridge O.; Masson P.; Fontecilla-Camps J. C.; Nachon F. Crystal structure of human butyrylcholinesterase and of its complexes with substrate and products. *J. Biol. Chem*. **2003**, *278*, 41141- 41147.
19. Saxena A.; Redman A.M.G.; Jiang X.; Lockridge O.; Doctor B.P. Differences in active-site gorge dimensions of cholinesterases revealed by binding of inhibitors to human butyrylcholinesterase. *Chem. Biol. Interact.* **1999**, *119–120*, 61–69.
20. Bush A.I. The metallobiology of Alzheimer's disease. *Trends Neurosci*. **2003**, *26*, 207–214.
21. Smith D.G.; Cappai R.; Barnham K.J. The redox chemistry of the Alzheimer's disease amyloid ß peptide. *Biochim. Biophys. Acta.* **2007**, *8*, 1976-1990.
22. Curtain C.C.; Ali F.; Volitakis I.; Cherny R.A.; Norton R.S.; Beyreuther K.; Barrow C.J.; Masters C.L.; Bush A.I.; Barnham K.J. Alzheimer's disease amyloid-beta binds copper and zinc to generate an allosterically ordered membrane-penetrating structure containing superoxide dismutase-like subunits. *J. Biol. Chem*, **2001**, *276*, 20466-20473.
23. Ceballos-Picot I.; Merad-Boudia M.; Nicole A.; Thevenin M.; Hellier G.; Legrain S.; Berr C. Peripheral antioxidant enzyme activities and selenium in elderly subjects and in

dementia of Alzheimer's type--place of the extracellular glutathione peroxidase. *Free Radic. Biol. Med.* **1996**, *20*, 579-587.

24. Hensley K.; Hall N.; Subramaniam R.; Cole P.; Harris M.; Aksenov M.; Aksenova M.; Gabbita S.P.; Wu J.F.; Carney J.M.; Lovell M.; William R.; Markesbery D.; Butterfield A. Brain regional correspondence between Alzheimer's disease histopathology and biomarkers of protein oxidation. *J. Neurochem.* **1995**, *65*, 2146-2156.
25. Mecocci P.; MacGarvey U.; Beal M.F. Oxidative damage to mitochondrial DNA is increased in Alzheimer's disease. *Ann. Neurol.* **1994**, *36*, 747-751.
26. Smith M.A.; Harris P.L.; Sayre L.M.; Perry G. Iron accumulation in Alzheimer disease is a source of redox-generated free radicals. *Proc Natl Acad Sci*. **1997**, *94*, 9866–9868
27. Martins R.N.; Harper C.G.; Stokes G.B.; Masters C.L. . Increased cerebral glucose-6-phosphate dehydrogenase activity in Alzheimer's disease may reflect oxidative stress. *J. Neurochem.* **1986***, 46*, 1042–1045.
28. Atwood C.S.; Huang X.; Moir R.D.; Tanzi R.E.; Bush A.I. Role of free radicals and metal ions in the pathogenesis of Alzheimer's disease. *Met. Ions Biol. Syst*. **1999**, *36*, 309-364.
29. Lovell M.A.; Robertson J.D.; Teesdale W.J.; Campbell J.L.; Markesbery W.R. Copper, iron and zinc in Alzheimer's disease senile plaques. *J. Neurol. Sci*. **1998**, *158*, 47-52.
30. Connor J.R.; Tucker P.; Johnson M.; Snyder B. Ceruloplasmin levels in the human superior temporal gyrus in aging and Alzheimer's disease. *Neurosci. Lett.* **1993**, *159*, 88-90.

31. Connor J.R.; Snyder B.S.; Arosio P.; Loeffler D.A.; LeWitt P. A quantitative analysis of isoferritins in select regions of aged, parkinsonian, and Alzheimer's diseased brains. *J. Neurochem.* **1995**, *65*, 717-724.

32. Basun H.; Forssell L.G.; Wetterberg L.; Winblad B. Metals and trace elements in plasma and cerebrospinal fluid in normal aging and Alzheimer's disease. *J. Neural Transm. Park Dis. Dement. Sect*. **1991**, *3*, 231-258.

33. Loeffler D.A.; DeMaggio A.J.; Juneau P.L.; Brickman C.M.; Mashour G.A.; Finkelman *J*.H.; Pomara N.; LeWitt P.A. Ceruloplasmin is increased in cerebrospinal fluid in Alzheimer's disease but not Parkinson's disease. *Alzheimer Dis. Assoc. Disord.* **1994**, *8*, 190-197.

34. Robinson S.R.; Noone D.F.; Kril J.; Halliday G.M. Most amyloid plaques contain ferritin rich cells. *Alzheimer's Res.* **1996**, *1*, 191−196.

35. Bush A.I.; Pettingell W.H.; Paradis M.D.; Tanzi R.E. Modulation of Ab adhesiveness and secretase site cleavage by zinc. *J. Biol. Chem*. **1994**, *269*, 12152–12158.

36. Bush A.I.; Pettingell W.H.; Multhaup G.; Paradis M.D.; Vonsattel J.P.; Gusella J.F.; Beyreuther K.; Masters C.L.; Tanzi R.E. Rapid induction of Alzheimer Aβ formation by zinc. *Science* **1994**, *265*, 1464–1467.

37. Dai X.L.; Sun Y.X.; Jiang Z.F. Cu(II) potentiation of Alzheimer Abeta1-40 cytotoxicity and transition on its secondary structure. *Acta. Biochim. Biophys. Sin*. **2006**, *38*, 765-772.

38. Atwood C.S.; Moir R.D.; Huang X.; Scarpa R.C.; Bacarra N.M.; Romano D.M.; Hartshorn M.A.; Tanzi R.E.; Bush A.I. Dramatic aggregation of Alzheimer Aβ by Cu(II) is induced by conditions representing physiological acidosis. *J. Biol. Chem*. **1998**, *273*, 12817–12826.

39. Huang X.; Tyndall J.D.A.; Goldstein L.E.; Glabe C.; Cuajungco M.P.; Hanson G.R.; Scarpa R.C.; Bowden E.F.; Atwood C.S.; Stokes K.C.; Saunders A.J.; Masters C.L.; Hartshorn M.A.; Leopold M.; Lim J.; Fairlie D.P.; Multhaup D.; Moir R.D.; Tanzi R.E.; Bush A.I. Cu(II) potentiation of Alzheimer Aβ neurotoxicity correlation with cell-free hydrogen peroxide production and metal reduction. *J. Biol. Chem.* **1999***, 274,* 37111-37116.

40. Cherny R.A.; Atwood C.S.; Xilinas M.E.; Gray D.N.; Jones W.D.; McLean C.A.; Barnham K.J.; Volitakis I.; Fraser F.W.; Kim Y.; Huang X.; Goldstein L.E.; Moir R.D.; Lim J.T.; Beyreuther K.; Zheng H.; Tanzi R.E.; Masters C.L.; Bush A.I. Treatment with a copper-zinc chelator markedly and rapidly inhibits beta-amyloid accumulation in Alzheimer's disease transgenic mice. *Neuron* **2001**, *30*, 665-676.

41. Huang X.; Atwood C.S.; Hartshorn M.A.; Multhaup G.; Goldstein L.E.; Scarpa R.C.; Cuajungco M.P.; Gray D.N.; Lim *J.*; Moir R.D.; Tanzi R.E.; Bush A.I. The Aβ peptide of Alzheimer's disease directly produces hydrogen peroxide through metal ion reduction. *Biochemistry* **1999**, *38*, 7609–7616.

42. Tabner B.*J.*; Turnbull S.; El-Agnaf O.M.; Allsop D. Formation of hydrogen peroxide and hydroxyl radicals from Aβ and alpha synuclein as a possible mechanism of cell death in Alzheimer's disease and Parkinson's disease. *Free Radic. Biol. Med*. **2002**, *32*, 1076–1083.

43. Lewén A.; Matz P.; Chan P.H. Free radical pathways in CNS injury. *J. Neurotrauma*. **2000**, *17*, 871-890.

44. Andersen *J*.K. Oxidative stress in neurodegeneration: cause or consequence? *Nat. Rev. Neurosci.* **2004,** *5,* S18-S25.

45. Feng Y.; Wang X. Antioxidant therapies for Alzheimer's disease. *Ox. Med. Cell. Longev.* **2012**, 1-17.

46. Thomas T.; Thomas G.; McLendon C.; Sutton T.; Mullan M. Beta-amyloid-mediated vasoactivity and vascular endothelial damage. *Nature*. **1996**, *380*, 168-171.

47. Bruce A.J.; Malfroy B.; Baudry M. Beta-amyloid toxicity in organotypic hippocampal cultures: protection by EUK-8, a synthetic catalytic free radical scavenger. *Proc. Natl. Acad. Sci*. **1996**, *93,* 2312–2316.

48. Frautschy S.A.; Hu W.; Miller S.A.; Kim P.; Harris-White M.E.; Cole G.M. Phenolic anti-inflammatory antioxidant reversal of A_-induced cognitive deficits and neuropathology. *Neurobiol. Aging.* **2001***, 22,* 993–1005.

49. Galasko, D. R.; Peskind, E.; Clark, C. M.; Quinn, *J*. F.; Ringman, M. D.; Jicha, G. A.; Cotman, C.; Cottrell, B.; Montine, T. *J*.; Thomas, R. G.; Alsen, P. Antioxidants for Alzheimer disease: a randomized clinical trial with cerebrospinal fluid biomarker measures. *Arch. Neurol.* **2012,** *69,* 836-841.

50. Garcia-Alloza M.; Borrelli L.A.; Rozkalne A.; Hyman B.T.; Bacskai B.J. Curcumin labels amyloid pathology in vivo, disrupts existing plaques, and partially restores distorted neurites in an Alzheimer mouse model. *J. Neurochem.* **2007***, 102,* 1095–1104.

51. Yang F.; Lim G.P.; Begum A.N.; Ubeda O.J.; Simmons M.R.; Ambegaokar S.S.; Chen P.P.;Kayed R.; Glabe C.G.; Frautschy S.A.; Cole G.M. Curcumin inhibits formation of amyloid beta oligomers and fibrils, binds plaques, and reduces amyloid in vivo. *J. Biol. Chem.* **2005***, 280***,** 5892–5901.

52. Wenzel E.; Soldo T.; Erbersdobler H.; Somoza V. Bioactivity and metabolism of trans-resveratrol orally administered to Wistar rats. *Mol. Nutr. Food Res.* **2005**, *49*, 482–494.

53. Niles R.M.; Cook C.P.; Meadows G.G.; Fu Y.M.; McLaughlin J.L.; Rankin G.O. Resveratrol is rapidly metabolized in athymic (nu/nu) mice and does not inhibit human melanoma xenograft tumor growth. *J. Nutr.* **2006**, *136*, 2542–6.

54. Anand P.; Kunnumakkara A.B.; Newman R.A.; Aggarwal B.B. Bioavailability of curcumin: problems and promises. *Mol. Pharmaceut.* **2007***, 4*, 807–818.

55. Begum A.N.; Jones M.R.; Lim G.P.; Morihara T.; Kim P.; Heath D.D.; Rock C.L.; Pruitt M.A.; Yang F.; Hudspeth B.; Hu S.; Faull K.F.; Teter B.; Cole G.M.; Frautschy S.A. Curcumin structure-function, bioavailability, and efficacy in models of neuroinflammation and Alzheimer's disease. *J. Pharmacol. Exp. Ther.* **2008**, *326*, 196-208.

56. Kelloff G.J.; Crowell J.A.; Hawk E.T.; Steele V.E.; Lubet R.A.; Boone C.W.; Covey J.M.; Doody L.A.; Omenn G.S.; Greenwald P.; Hong W.K.; Parkinson D.R.; Bagheri D.; Baxter G.T.; Blunden M.; Doeltz M.K.; Eisenhauer K.M.; Johnson K.; Knapp G.G.; Longfellow D.G.; Malone W.F.; Nayfield S.G.; Seifried H.E.; Swall L.M.; Sigman C.C. Strategy and planning for chemopre-ventive drug development: clinical development plan: curcumin. *J. Cell Biochem. Suppl.* **1996**, *26*, 72-85.

57. Camps P.; Formosa X.; Galdeanoa C.; Gómeza T.; Torrero D.M.; Ramírez L.; Viayna E.; Gómez E.; Isambert N.; Lavilla R.; Badia A.; Clos M.V.; Bartolini M.; Mancini F.; Andrisano V.; Bidon-Chanal A.; Huertas O.; Dafni T.; Luque F.J. Tacrine-based dual binding site acetylcholinesterase inhibitors as potential disease-modifying anti-Alzheimer drug candidates. *Chem. Biol. Interact*. **2010**, *187*, 411–415.

58. Camps P.; Formosa X.; Galdeano C.; Muñoz-Torrero D.; Ramírez L.; Gómez E.; Isambert N.; Lavilla R.; Badia A.; Clos M.V.; Bartolini M.; Mancini F.; Andrisano V.;

Arce M.P.; Rodríguez-Franco M.I.; Huertas O.; Dafni T.; Luque F.J. Pyrano[3,2-c]quinoline-6-chlorotacrine hybrids as a novel family of acetylcholinesterase- and beta-amyloid-directed anti-Alzheimer compounds. *J. Med. Chem*. **2009**, *52*, 5365-5379.

59. Camps P.; Formosa X.; Galdeano C.; Gómez T.; Muñoz-Torrero D.; Scarpellini M.; Viayna E.; Badia A.; Clos M.V.; Camins A.; Pallàs M.; Bartolini M.; Mancini F.; Andrisano V.; Estelrich J.; Lizondo M.; Bidon-Chanal A.; Luque F.J. Novel donepezil-based inhibitors of acetyl- and butyrylcholinesterase and acetylcholinesterase-induced beta-amyloid aggregation. *J. Med. Chem*. **2008**, *51*, 3588-3598.
60. Hamulaková, S.; Kristian, P.; Jun, D.; Kuca, K.; Imrich, J.; Danihel, I.; Bohm, S.; Klika, K.D.Synthesis, structure, and cholinergic effect of novel neuroprotective compounds bearing the tacrine pharmacophore. *Heterocycles* **2008**, *76*, 1219-1235.
61. Bellamy F.D.; Ou K. Selective reduction of aromatic nitro compounds with stannous chloride in non acidic and non aqueous medium. *Tetrahedron Lett.* **1984**, *25*, 839–842.
62. Rao P.P.N.; Uddin M.J.; Knaus E.E. Design, synthesis, and structure-activity relationship studies of 3,4,6-triphenylpyran-2-ones as selective cyclooxygenase-2 inhibitors *J. Med. Chem.* **2004**, *47,* 3972-3990.
63. Hu M.K.; Wu L.J.; Hsiao G.; Yen M.H. Homodimeric tacrine congeners as acetylcholinesterase inhibitors. *J. Med. Chem.* **2002**, *45,* 2277-2282.
64. Bolognesi M.L.; Cavalli A.; Valgimigli L.; Bartolini M.; Rosini M.; Andrisano V.; Recanatini M.; Melchiorre C. Multi-target-directed drug design strategy: from a dual binding site acetylcholinesterase inhibitor to a trifunctional compound against Alzheimer's disease. *J. Med. Chem*. **2007**, *50*, 6446-6449.

65. Ellman G. L.; Courtney K. D.; Andres V. Jr.; Featherstone R. M. A new and rapid colorimetric determination of acetylcholinesterase activity. *Biochem. Pharmacol*. **1961**, *7*, 88-95.

66. Ebada S.S.; Edrada R.A.; Lin W.; Proksch P. Methods for isolation, purification and structural elucidation of bioactive secondary metabolites from marine invertebrates. *Nat. Protoc*. **2008**, *3*, 1820-1831.

67. Karamac M. Chelation of Cu(II), Zn(II), and Fe(II) by tannin constituents of selected edible nuts. *Int. J. Mol. Sci.* **2009**, *10*, 5485-5497.

68. Mosmann T. Rapid colorimetric assay for cellular growth and survival: application to proliferation and cytotoxicity assays. *J. Immunol. Methods*. **1983**, *65*, 55-63.

69. Lin H.Y.; Chou C.C. Antioxidative activities of water-soluble disaccharide chitosan derivatives. *Food Res. Int*. **2004**, *37*, 883–889.